Polynuclear 3*d*/4*f*-Metal Complexes as Molecular Magnetic Refrigerants and Single-Molecule Magnets

Paul Richardson, BSc.

Department of Chemistry

Submitted in partial fulfillment of the requirements for the degree of

Master of Science

Faculty of Mathematics and Science, Brock University

St. Catharines, Ontario

Abstract

The use of two different chelating/bridging ligands, naphthalene-2,3-diol (ndH_2) and acenaphthenequinone dioxime ($acndH_2$), in heterometallic 3*d*/4*f*-metal cluster chemistry has yielded two new families of polynuclear Cu^{II}/Ln^{III} clusters. These complexes were found to exhibit interesting magnetic properties, specifically single-molecule magnetism and the magnetocaloric effect.

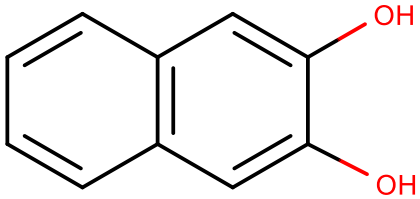

ndH_2

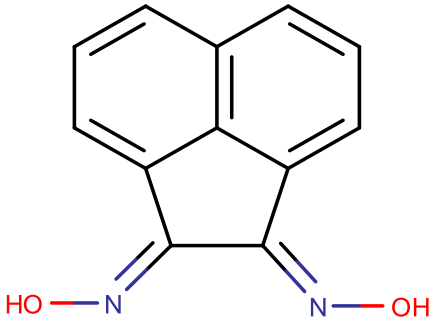

$acndH_2$

In this thesis, Chapter 1 lays the foundation for the research presented within. This section covers the fundamentals of polynuclear metal complexes, molecular magnetism, and the magnetocaloric effect, as well as the approaches used for the synthesis of new polynuclear metal complexes and the choice of ligands. Chapters 2 and 3 report the results of the current thesis. In Chapter 2, the synthesis and characterization of a family of $\{Cu_4Ln\}$ complexes (Ln^{III} = Gd^{III} (**1**), Tb^{III} (**2**), Dy^{III} (**3**)), employing the ligand ndH_2 is presented. The complexes join a handful of previously reported $\{Cu_4Ln\}$ clusters, however, the family reported in this thesis are the first 'propeller'-like clusters that exhibit single-molecule magnetism and magnetic refrigeration properties.

In Chapter 3, a family of $\{Cu_6Ln_2\}_n$ chains (Ln^{III} = Gd^{III} (**4**), Tb^{III} (**5**), Dy^{III} (**6**)) obtained through the employment of ligand acndH_2 is presented. This family of 1D-chains is a novel motif that has not been previously reported in the literature, with only a few discrete $\{Cu_6Ln_2\}$ 0D-clusters having been previously reported. The complexes were magnetically characterized, with **4** and **5** exhibiting ferromagnetic exchange interactions while **6** revealed a more complex magnetic behaviour with both ferromagnetic and antiferromagnetic interactions dominating at different temperature regimes. Furthermore, **5** was found to behave as a single-molecule magnet and **4** was shown to act as a molecular magnetic refrigerant.

Acknowledgements

There are many people that I wish to thank; that without their help, completing this task would have been nigh impossible. First and foremost, I want to thank my supervisor, Prof. Theocharis C. Stamatatos. Over the 3 years that I have spent with him, both in my undergraduate and my Master's thesis, I have come to look up to him not only as a scientist and an educator, but as a mentor in my scientific career. His depth of knowledge in the fields of inorganic chemistry and magnetism taught me a great deal, and was invaluable towards the completion of this thesis. Whether it be through meetings in his office or after hours over a beer, any interaction with him has been of great importance to me and my progress in academia. Thank you for pushing me to newer and greater heights!

Furthermore, I would like to thank the other professors who sat on my committee, both current and former: Prof. Georgii Nikonov, Prof. Feng Li, and Prof. Tomas Hudlicky. Their insights in how to improve the quality of my research and comments on where to improve have been, and will continue to be, of great use to me in the future.

As well, this thesis would not have been possible without a worldwide network of collaborators. Many thanks go out to Dr. Luís Cunha-Silva, Dr. Kevin J. Gagnon, and Dr. Simon J. Teat for the solving and refining of the crystal structures presented within this thesis. I would also like to thank Dr. Jinkui Tang for providing the magnetism data of all of the complexes presented herein. Finally, I would like to thank Dr. Giulia Lorusso and Dr. Marco Evangelisti for giving me the opportunity to probe the magnetocaloric properties of my complexes through specific heat studies of my complexes.

My gratitude also extends to the other members of the research group, both past and present: Dimos, Eleni, Penny, Alysha, Angeliki, and Marco! Whether it be through talks after meetings or grabbing a coffee together, you will not know how important these interactions were towards keeping me on the right path. Particular thanks goes to Dr. Dimitrios Alexandropoulos, whose guidance when I first entered the lab helped me start this research off on the right foot.

Finally, I would like to thank my friends and family. Justin Harney, thanks for allowing me the opportunity to get away to Hamilton now and then and recuperate my mind. Scott Teibert, Scott Rempel, and Zach O'Doherty, thank you for the late night talks and games, which helped me stay balanced. To my parents, Al and Debbie, and to my brother, Sean, your love and support helped push me forwards, from home-cooked meals to rides to campus. And last, but most certainly not least, I want to thank my wonderful fiancée, Elly Chang. Elly, your strength and love, even from cities (and sometimes continents) away, was felt all through this thesis. I know I certainly was difficult at times during this process, and your patience means so much to me. Thank you for keeping me sane and whole!

Table of Contents

Chapter 1: Introduction

Chapter 2: 'All three-in-one': ferromagnetic interactions, single-molecule magnetism and magnetocaloric properties in a new family of [Cu_4Ln] (Ln^{III} = Gd, Tb, Dy) clusters

Chapter 3: New dioximes as bridging ligands in 3*d*/4*f*-metal cluster chemistry: 1-D chains of {Cu_6Ln_2} clusters bearing acenaphthenequinone dioxime and exhibiting slow magnetization relaxation and magnetocaloric properties

List of Schemes

List of Figures

List of Tables

List of Publications

CHAPTER 2:

P. Richardson, D. I. Alexandropoulos, L. Cunha-Silva, G. Lorusso, M. Evangelisti, J. Tang, T. C. Stamatatos. "'All three-in-one': ferromagnetic interactions, single-molecule magnetism and magnetocaloric properties in a new family of $[Cu_4Ln]$ (Ln^{III} = Gd, Tb, Dy) clusters", Inorganic Chemistry Frontiers, *2*, 945, **2015**.

CHAPTER 3:

P. Richardson, K. J. Gagnon, S. J. Teat, G. Lorusso, M. Evangelisti, J. Tang, T. C. Stamatatos. "New dioximes as bridging ligands in 3*d*/4*f*-metal cluster chemistry: 1-D chains of $\{Cu_6Ln_2\}$ clusters bearing acenaphthenequinone dioxime and exhibiting slow magnetization relaxation and magnetocaloric properties", Inorganic Chemistry, In Progress.

List of Abbreviations

$(N^nBu_4)(MnO_4)$	*tert*-butylammonium permanganate
μ, μ_3	Bridging modes of ligands
μ_β	Bohr magneton
0-, 1-, 2-, 3-D	0-, 1-, 2-, 3-Dimensional
^3He	Helium-3
Å	Angstrom
ac	Alternating current
$acac^-$	Acetylacetonate
$acndH_2$	Acenaphthenequinone dioxime
C	Curie constant
c	Speed of light
$catH_2$	Catechol
$CHCl_3$	Chloroform
cm^{-1}	Wavenumber
CShM	Continuous Shape Measures
D	Zero field splitting parameter
$dapdoH_2$	2,6-diacetylpyridine dioxime
dc	Direct current
DMF	Dimethylformamide
$dmgH_2$	Dimethylglyoxime
DNA	Deoxyribonucleic acid
dobdc	2,5-dioxido-1,4-benzenedicarboxylate

EPR	Electron paramagnetic resonance
Et_2O	Diethyl ether
Et_4NOH	Tetraethylammonium hydroxide
EtOH	Ethanol
g	Landé factor
GGG	Gadolinium gallium garnet
gly	Glycolate
H	Magnetic field
H_2L	*N*,*N*′-bis(3-methoxysalicylidene)-1,3-diamino-2,2-dimethylpropane
hmpH	2-(hydroxymethyl)pyridine
Hz	Hertz
I	Nuclear spin
IR	Infrared
J	Total angular momentum
J_1, J_2…	Magnetic exchange coupling constants
K	Kelvin
KOH	Potassium hydroxide
k_β	Boltzmann constant
L	Bridging/chelating ligand
L	Orbital angular momentum
L’	Terminal ligand
M	Magnetization
M	Metal
MCE	Magnetocaloric effect

m_e	Mass of an electron
MeCN	Acetonitrile
MeOH	Methanol
m_s	Microstate
n	Number of unpaired electrons
N_A	Avogadro's number
$NaHCO_3$	Sodium bicarbonate
NaOMe	Sodium methoxide
ndH_2	Naphthalene-2,3-diol
$NH_2OH \cdot HCl$	Hydroxylamine hydrochloride
nm	Nanometer
NMR	Nuclear magnetic resonance
paoH	2-pyridinealdoxime
$pdmH_2$	pyridine-2,6-dimethanol
Q_c	Heat absorbed by refrigerant during isothermal demagnetization
S	Spin angular momentum
S_e	Electronic entropy
S_i	Spin quantum number
S_m	Magnetic entropy
SMM	Single molecule magnet
SQUID	Superconducting Quantum Interference Device
S_r	Lattice entropy
S_{total}	Total entropy
T	Temperature
T_{ad}	Adiabatic temperature

T_B	Blocking temperature
T_C	Curie temperature
T_N	Néel temperature
TPA	Tritylphosphonic acid
U	Barrier to magnetization reversal
XMCD	X-ray magnetic circular dichroism
Z	Effective nuclear charge
α	Sommerfield's fine structure constant
β	Transfer integral
ζ	Free-ion spin-orbit coupling constant
η^1, η^2, η^3	Coordination modes of ligands
θ	Weiss constant
λ	Spin-orbit coupling constant
ν	Frequency
τ	Relaxation time
τ_o	Pre-exponential factor
χ'	Real or in-phase susceptibility
χ''	Imaginary or out-of-phase susceptibility
χ^D	Diamagnetic susceptibility
χ_g	Mass magnetic susceptibility
χ_M	Molar magnetic susceptibility
χ^P	Paramagnetic susceptibility
χ_v	Volume magnetic susceptibility

CHAPTER 1: Introduction

1.1. Polynuclear Metal Complexes

When it comes to the miniaturization of devices, the "top-down" approach has been used almost exclusively throughout history. Starting from the macroscopic scale, moving to the microscopic, and then ultimately to the nanoscale, the "top-down" approach has proven capable of continually producing devices, and components of devices, of steadily decreasing size. However, the limits of the "top-down" approach are beginning to be reached. Around the scale of 100 nm, it becomes incredibly difficult for the "top-down" approach to synthesize materials with desired properties and functions. Therefore, it is important to think of an alternative of producing these compounds. In 1960, Prof. Richard Feynman posed a challenge to the scientists of the world. He suggested that the feat of being able to create a motor the size of a fingertip using the "top-down" approach was not as great a feat as it was made out to be, and that a new approach should be considered. Famously quoted by saying "There is plenty of room at the bottom", he suggested that instead of breaking down macroscopic materials to make smaller and smaller devices, it could be possible to build up devices from the atomic scale to the nanoscale by utilizing building blocks, atomic elements and molecules.[1] This has since been described as the "bottom-up" approach to the miniaturization of devices.

While both of these synthetic approaches are different, they are both closely related in their goals. Both attempt to miniaturize devices and components of devices, but from different initial

dimensions. The “top-down” approach involves breaking down macroscopic materials into smaller and smaller nanoparticles, with the goal of retaining the bulk properties of the material in the nanoparticles. On the other hand, the “bottom-up” approach makes use of individual elements and molecules, combined under various reaction conditions, to try and form molecules that reach nanoscale dimensions. It would be prudent at this time to define what a molecule is, compared to nanoparticles. A molecule can be defined as a thermodynamically stable, dimensionally discrete and electrically neutral species, containing at least two atoms held together through covalent interactions. This differentiates molecules from a few other important types of compounds, namely ionic and multidimensional compounds. Ionic compounds consist of cations and anions, which have positive and negative charges, respectively. A representative example would be a crystal of NaCl, made up of Na^+ and Cl^- ions. The lines become a little blurred when talking about multidimensional compounds. Multidimensional compounds are polymeric species consisting of repeating units that extend their structures in more than one dimension through covalent bonds.[2] Both discrete molecules and multidimensional compounds can be of large size and possess well-defined structural motifs. These two approaches are linked to each other through the field of “molecular nanoscience”.[3]

Ultimately, the goal of the “bottom-up” approach is to isolate a collection of different molecular components in such a way that they all work to achieve a given function. The individual molecules of the collection would all work in their own individual way, while the collection as a whole would perform the given task at hand. These functions would operate through change in surrounding environment, either atomic or electric.[4] Asides from the benefit of miniaturizing devices to pack more functionality into machines, making discrete molecular devices also holds the benefit of allowing scientists to probe the fundamentals of physical

properties of molecules, and where given properties, such as magnetic and optical properties, arise in a given molecule. This information provides scientists with valuable information on how to further improve their devices, enhancing the properties within.[3]

Molecular nanoscience makes use of simple starting materials that are usually small in size. These include simple metal salts as metal sources, and simple organic molecules called "ligands", which will bind to the metal ions. Ligands can be divided into two separate categories; these are "chelating/bridging" ligands, denoted as L, and terminal ligands, denoted as L′. Chelating and bridging ligands are used to allow the metal ions to aggregate into large nuclearity motifs, in an attempt to reach nanoscale dimensions. These ligands will contain donor atoms, such as N and O, which will form coordination bonds with the metal ions. In addition to the bridging capabilities of these ligands, they also quite often act as chelating agents as well. This enhances the thermodynamic stability of the complexes, allowing for the isolation of crystalline materials, the importance of which will be discussed later. Terminal ligands are added to reaction systems to prevent excessive aggregation of the metal ions, occupying vacant coordination sites on the metals' coordination spheres and providing further thermodynamic stability. The combination of these three components can give rise to the formation of polynuclear metal complexes, also called "coordination clusters" or "cluster" compounds. These complexes will have the general formula of $[M_x(L)_y(L')_z]^n$.[5] 'x' is any integer value that is larger or equal to three, while 'y' and 'z' are integer values. The value of n can be either 0 for neutral compounds, a positive integer for cationic compounds, or a negative integer for anionic compounds.

Molecular nanoscience makes use of the "bottom-up" approach to try and isolate polynuclear metal complexes of the types described above. These 0-D species provide certain advantages compared to the "top-down" approach, specifically the advantages conferred to it from the

molecular chemistry. One of the biggest advantages is the conditions under which the "bottom-up" approach can operate. The "top-down" approach to nanoscale materials involves the breakdown of bulk materials into nanoparticles, a process which requires high temperatures and pressures. However, the "bottom-up" approach requires "low energy" conditions, such as ambient temperature and pressure.[2] Other advantages of molecular chemistry are also present; these are the monodispersity, the presence of the organic ligands, the solubility and crystallinity, and the good degree of separation between the molecules.[2,6] Monodispersity describes how every particle in a crystal is of identical size and shape. In the case of polynuclear metal complexes, these particles are the actual metal clusters present in the crystal lattice itself. When using the "top-down" approach, the lack of synthetic control renders it extremely difficult to isolate nanoparticles of uniform size and shape. This holds great implications of the properties of the material, because the properties may change from particle to particle. For example, one nanoparticle with a given size and shape may exhibit desirable magnetic or optical properties, but another particle with a different size and shape may not share those properties at all. However, the products formed by the "bottom-up" approach, since they are crystalline in nature, are expected to be monodisperse and consequently possess identical properties. An example of a monodisperse crystal system can be seen in Figure 1.1.[7]

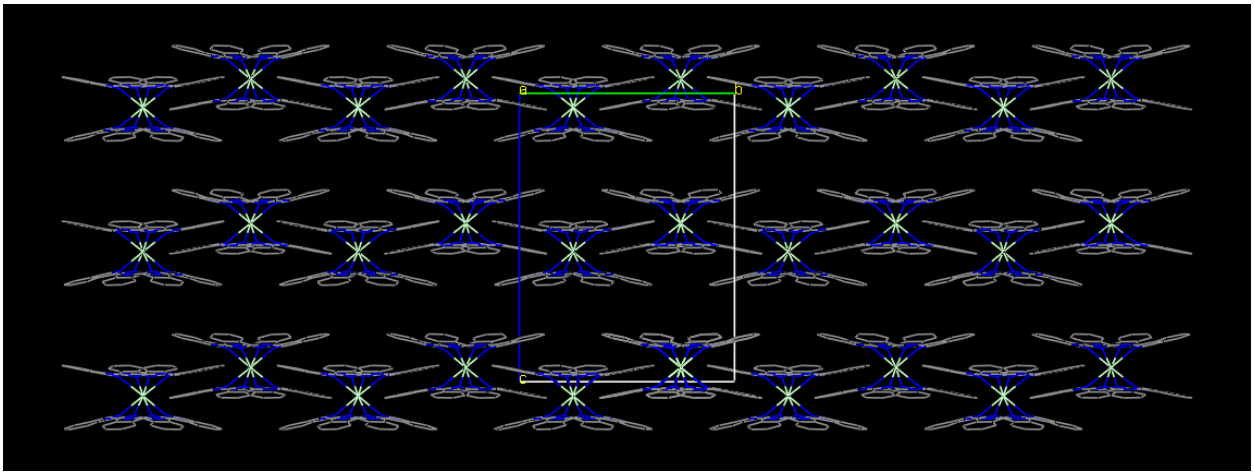

Figure 1.1. An example of a monodisperse crystal packing of a $[Tb(Pc)_2]^-$ molecule, viewed along the crystallographic *a*-axis. Colour scheme: Tb^{III}, light green; N, blue; C, grey. Reproduced from Ref. 7.

The presence of the organic ligands used in the synthesis of polynuclear metal complexes also has an effect on the chemical properties, such as solubility, crystallinity and purity. As mentioned before, the ligands have the ability to form coordination bonds with the metal ions through the presence of donor atoms. The organic shells allow the clusters to organize into crystalline motifs, which is highly important for the analysis of the physical properties. Solubility is also another property that the "bottom-up" approach holds as an advantage over the "top-down" approach. The shell of organic ligands that make up the polynuclear metal complex enhances the solubility of these complexes in a variety of polar or non-polar solvents, thus allowing for the growth of single-crystals suitable for X-ray diffraction studies. This property, coupled with the potential of the cluster compound to maintain its structure in solution, is essential; it allows the cluster to be purified if it is needed, or processed for other applications such as deposition on surfaces. On the other hand, the nanoparticles yielded by the "top-down"

approach are usually insoluble, yielding only suspensions in different solvents. This hinders the effectiveness and potential applications of these materials. The crystallinity of polynuclear metal complexes allows for an accurate determination of the structure, and consequently the potential to link the physical properties to the molecular structure of the cluster. Due to the irregularities in nanoparticles formed by the "top-down" approach, it is difficult to isolate crystalline variants of these materials. Finally, the coordination compounds in the crystals are well-separated from each other, due to the peripheral shell of organic ligands and the presence of solvate molecules and/or counterions in the crystal lattice. This is important for the proper analysis of certain physical properties, such as the magnetic properties. Crystals are also usually free of the defects that affect nanoparticles on a regular basis, such as surface irregularities, roughness, etc. These advantages make the utilization of the "bottom-up" approach an attractive synthetic technique for chemists interested in designing molecule-based materials with nanoscale dimensions.

If synthetic chemists wish to reach nanoscale dimensions with their polynuclear metal complexes, they must obviously increase the nuclearity (i.e., the total number of metal ions present) of the compounds they synthesize. While crystallizing these very large metal complexes can be a difficult task, it is not unheard for clusters with astoundingly large nuclearities to be isolated. These large nanosized clusters, in addition to their interesting physical properties, are aesthetically pleasing to look at with unusual structures and topologies, which is an added bonus on top of all the other advantages conferred by this chemistry. The record nuclearity in homometallic Cu^{II} chemistry is the $\{Cu_{44}\}$ cluster isolated by Powell and coworkers in 2004 (Figure 1.2).[8] With regards to homometallic lanthanide(III) chemistry, the record is shared, with a $\{Gd_{104}\}$ reported by Zheng and coworkers in 2014, and a $\{Dy_{104}\}$ reported by Gu and Xue in 2007 (Figure 1.3 and Figure 1.4, respectively).[9,10] Finally, in heterometallic Cu^{II}/Ln^{III} chemistry,

the record nuclearity is held by a $\{Cu_{36}Ln_{24}\}$ cluster, reported by Tong and coworkers in 2012 (Ln = Dy and Gd; Figure 1.5).[11]

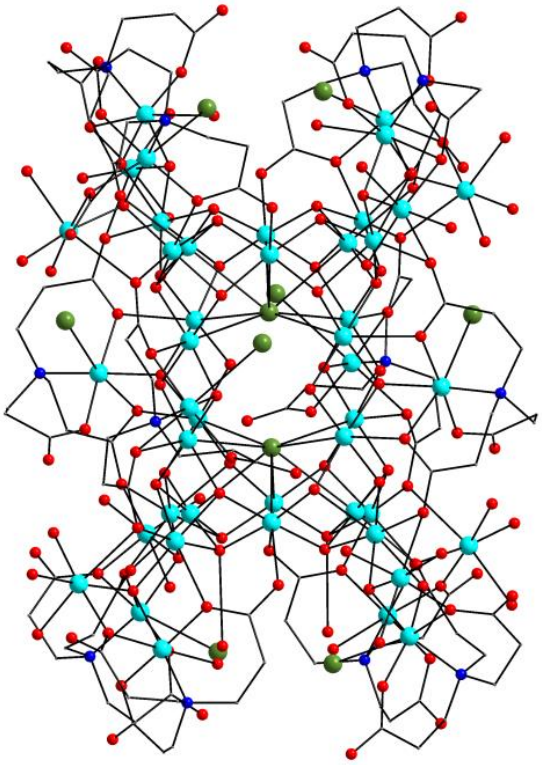

Figure 1.2. Structure of the $\{Cu_{44}\}$ of Powell and coworkers. The structure can be described as a central $[Cu_{24}]$ unit anchored with two Br^- anions, surrounded by a shell of Cu^{II}/ligand units. H atoms are omitted for clarity. Colour scheme: Cu^{II}, cyan; Br^-, olive green; N, blue; O, oxygen; C, grey. Reproduced from Ref. 8.

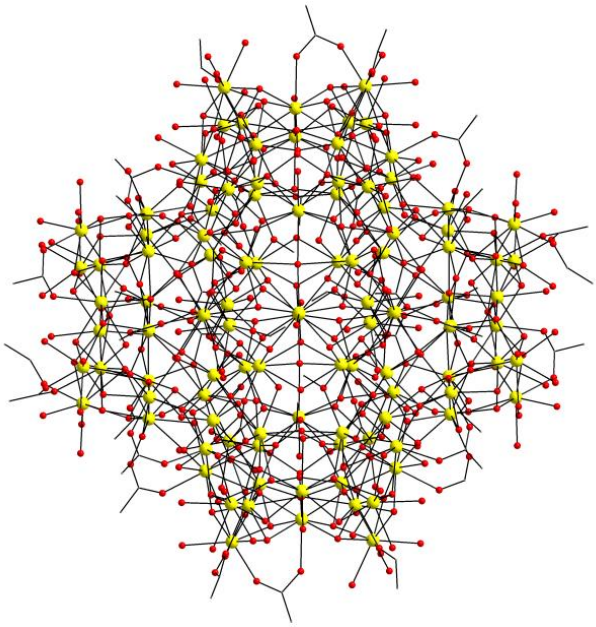

Figure 1.3. Structure of the {Gd_{104}} of Zheng and coworkers, described as a "Keplerate"-like structure. H atoms are omitted for clarity. Colour scheme: Gd^{III}, yellow; O, red; C, grey. Reproduced from Ref. 9.

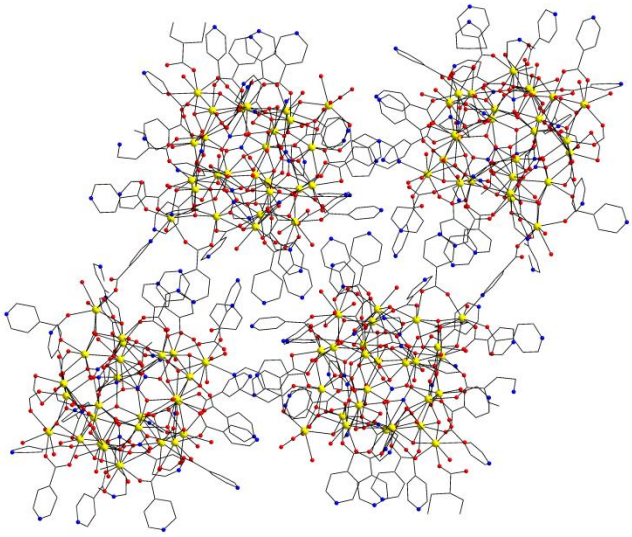

Figure 1.4. Structure of the {Dy_{104}} cluster reported by Gu and Xue. It can be described as a tetramer of {Dy_{26}} clusters. H atoms are omitted for clarity. Colour scheme: Dy^{III}, yellow; N, blue; O, red; C, grey. Reproduced from Ref. 10.

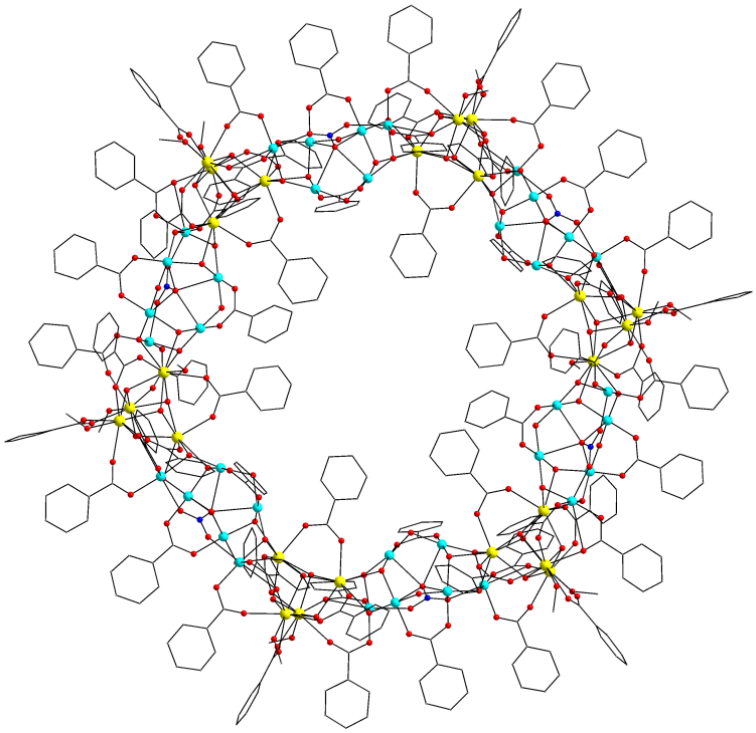

Figure 1.5. Structure of the $\{Cu_{36}Ln_{24}\}$ cluster reported by Tong and coworkers, showing a metallo-ring motif. H atoms are omitted for clarity. Colour scheme: Ln^{III}, yellow; Cu^{II}, cyan; N, blue; O, red; C, grey. Reproduced from Ref. 11.

1.2. Synthetic Routes for the Synthesis of 3*d*/4*f*-Metal Clusters

Currently, there are two main approaches when it comes to the synthesis of polynuclear metal complexes. The first attempts to follow routes similar to those used by synthetic organic chemists, treating atoms and molecules as singular building blocks to target towards specific products. This approach is called the "design approach", also called the "ligand-directed approach".[12] This method makes use of rigid ligands that possess specific binding modes, as well as metals that have well defined coordination sites and coordination geometry. Using this

method, a high level of design is introduced into the synthetic method, as well as some predictability to what the final products may be. This has led to the isolation of many different products, as well as aesthetically pleasing structures, with structures resembling various highly symmetric polyhedra (Figure 1.6).[13]

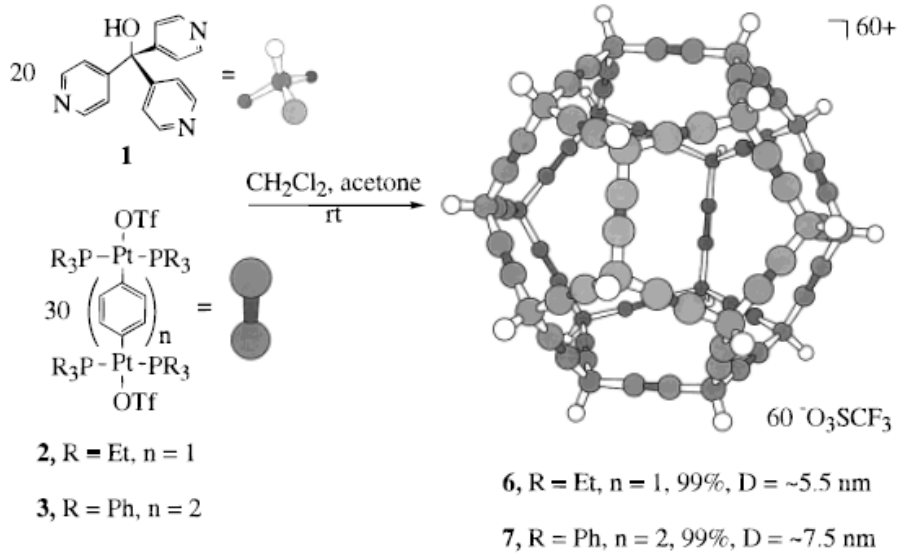

Figure 1.6. An example of the ligand-directed approach, resulting in the synthesis of a dodecahedral compound. The dimensions of the dodecahedron vary based on the ligands used in the synthesis, and approaches the nanoscale dimensions. Used with permission from the American Chemical Society, from Ref. 13.

Researchers such as Stang and Fujita have made use of this process with a variety of different ligands to isolate new products.[14,15] Some examples of ligands used in the ligand-directed approach can be seen in Figure 1.7.[16] However, there is a distinct downside to the ligand-directed approach. While the products can be predicted, and the building blocks can be viewed as molecular Lego®, the desire for control greatly restricts what products can be formed. The

ligands used in the ligand-directed approach do not allow for unexpected bridging modes, following only their strict shapes. The metal ions used in this approach as well, can adopt specific coordination geometries. For example, Pt^{II} and Pd^{II} are often employed in this approach because they have distinct preferred square planar coordination geometries. Transition metal ions (e.g. Cu^{II}) and lanthanides (e.g. Gd^{III}, Tb^{III}, Dy^{III}) can adopt many different coordination geometries, and this flexibility is undesirable in this approach. Consequently, there must be another technique that can make use of these components, or else synthetic chemists are simply eliminating a large portion of their toolbox that is the periodic table of elements.

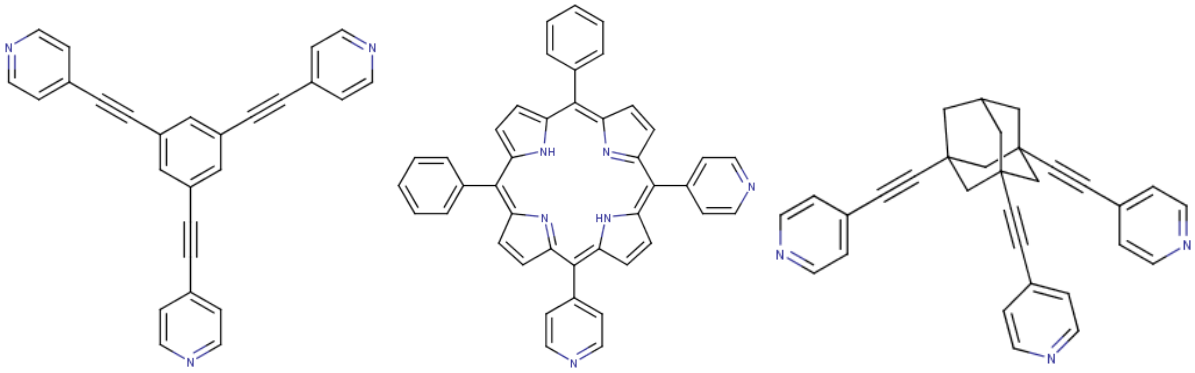

Figure 1.7. Some examples of ligands used in the ligand-directed approach. These ligands possess rigid frameworks and few donor atoms, restricting their freedom of movement and binding, but allowing for the resulting structures to be predicted and targeted. Reproduced from Ref. 16.

The other technique used in the synthesis of polynuclear metal complexes is called "serendipitous assembly" or "self-assembly".[17] The hallmark of this synthetic approach is its complete flexibility; any metal ion and organic ligand could be used in this approach to potentially isolate polynuclear metal complexes. In essence, simple metal salts or even small

metal clusters, in conjunction with multitopic ligands, are combined in a variety of reaction solvents and conditions.[18] This is the most widely used technique towards the synthesis of polynuclear metal complexes. While the structures formed through this method can only be predicted with extremely limited reliability, the flexibility of this technique allows for a wide variety of structures to be potentially isolated. Two representative examples of serendipitous assembly in action can be seen in both homometallic 3*d*-metal chemistry and heterometallic 3*d*/4*f*-metal cluster chemistry. From homometallic 3*d*-metal chemistry, the use of serendipitous assembly led to the largest in nuclearity Mn-containing complex to date, a $\{Mn^{III}_{84}\}$ cluster (Figure 1.8).[19] The cluster can be described as a torus containing repeating units of almost linear $[Mn_3O_4]$ units and $[Mn_4O_2(OMe)_2]$ cubanes, and was synthesized through the combination of a smaller $[Mn_{12}O_{12}(O_2CMe)_{16}(H_2O)_4]$ cluster and $(N^nBu_4)(MnO_4)$ in the presence of acetic acid. The torus of the $\{Mn_{84}\}$ possesses an interior diameter of approximately 1.9 nm, a total diameter of approximately 4.2 nm, and a thickness of approximately 1.2 nm. These dimensions place the $\{Mn_{84}\}$ on a similar scale of size comparable to classic nanoparticles made through the "top-down" approach.

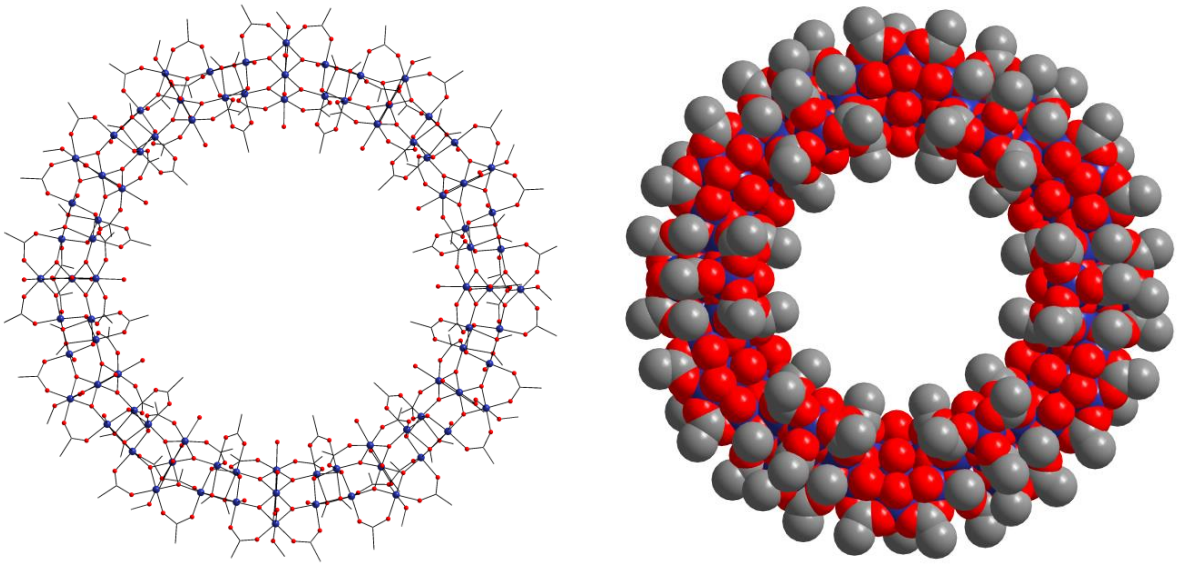

Figure 1.8. Ball-and-stick (left) and space-filling (right) representations of the {Mn_{84}} cluster, reported by Christou and coworkers. H atoms are omitted for clarity. Colour scheme: Mn^{III}, blue; O, red; C, grey. Reproduced from Ref. 19.

From heterometallic 3*d*/4*f*-metal cluster chemistry, an interesting structure made through the serendipitous assembly method is a {$Cu_{24}Dy_8$} cluster, reported by Winpenny and coworkers (Figure 1.9).[20] The overall structure of the complex is described as a central [Cu^{II}_{12}] cuboctahedron, encapsulated by a [Dy^{III}_8] cube. The [Dy^{III}_8] cube is then surrounded by six [Cu^{II}_2] dimers. The inner [Cu^{II}_{12}] cuboctahedron is connected through one NO_3^- and twenty-four OH^- bridging ligands. This complex was formed through the combination of $Dy(NO_3)_3$, $Cu(O_2CMe)_2$, and the ligand tritylphosphonic acid (TPA) in a 1:2:1 ratio, in solvent MeCN. It was found that, similar to the {Mn_{84}} cluster, the {$Cu_{24}Dy_8$} cluster acts as a single-molecule magnet (*vide infra*).

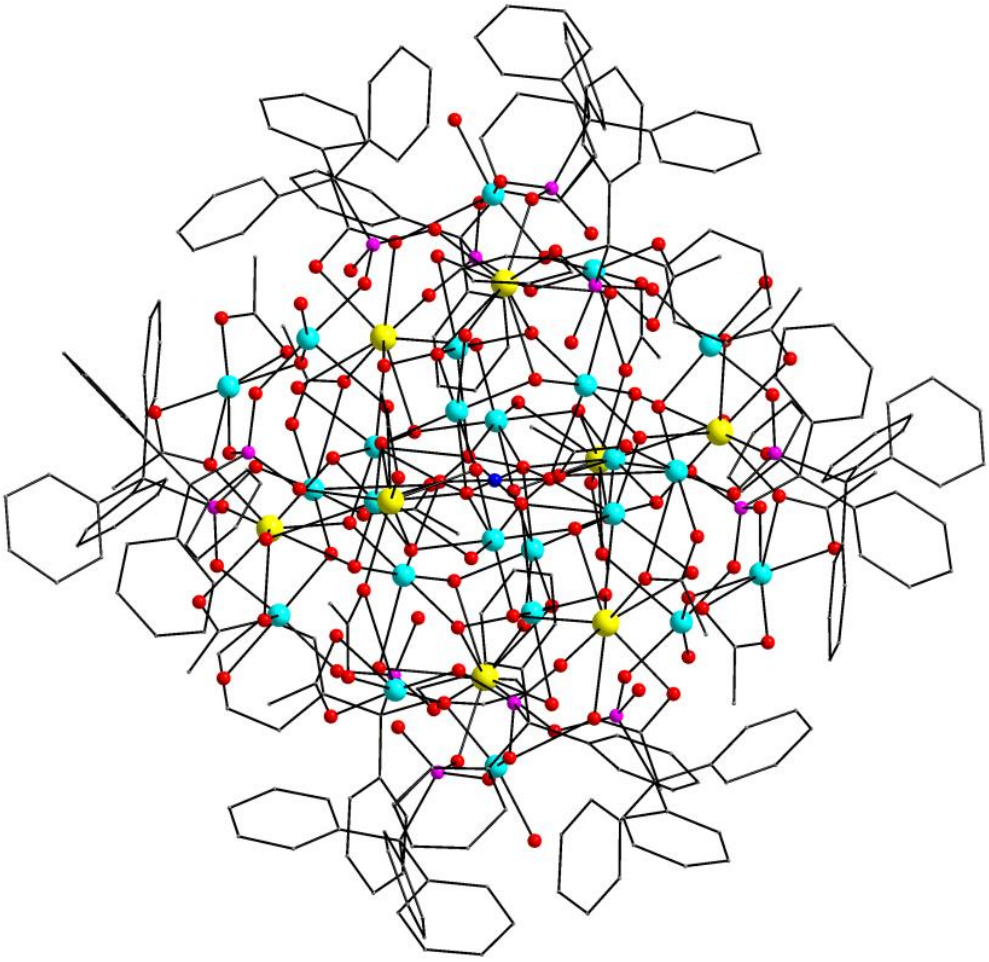

Figure 1.9. Structure of the $\{Cu_{24}Dy_8\}$ cluster, reported by Winpenny and coworkers. H atoms are omitted for clarity. Colour scheme: Dy^{III}, yellow; Cu^{II}, cyan; P, purple; O, red; N, blue; C, grey. Reproduced from Ref. 20.

It is impossible to have predicted these structures from the starting point of this research, and there is no rationale that could explain why these complexes formed in solutions and subsequently crystallized out of them. The only information that can be inferred through their synthesis is that these complexes are the most thermodynamically stable ones, and thus were capable of crystallizing. In the case of the $\{Mn_{84}\}$, aggregating so many of the two different

repeating units discussed before into a torus motif, would be highly improbable due to the versatility of the ancillary carboxylate ligands to take on different binding modes. When discussing the $\{Cu_{24}Dy_8\}$ cluster, to try and plan out how to encapsulate a cuboctahedron of $[Cu^{II}_{12}]$ within a $[Dy^{III}_8]$ cube is quite a daunting task. This does not mean, however, that the serendipitous assembly approach is completely random and without thought. A synthetic chemist must always consider carefully not just the metal ions, their oxidation states and ligands used in a given reaction system, but also the conditions under which the given reaction and crystallization techniques will take place (e.g. varying temperature, pressure, pH, solvent mixtures, etc.).[2] Once a structure has been crystallographically determined, a synthetic chemist can then begin to take rational steps to try and affect the structure that was initially synthesized. This is known as "chemical reactivity", and can involve modifying the pH, the solvents, and even the ligands involved.[21] Only a single synthetic parameter is changed at each step to try and determine what is essential towards the formation of the cluster, and what variations can change the structure. Changing something as simple as a H atom to a larger atom (e.g. a halide) on a ligand's scaffold may affect the steric properties of the ligand and consequently have drastic effects on the original structure. It would be shortsighted for synthetic chemists to remove all of this potential from their synthetic toolbox, considering all the possibilities that the serendipitous assembly approach offers to the field of molecular nanoscience.

1.3. The Choice of the Organic Chelating/Bridging Ligands

While synthetic techniques such as serendipitous assembly seem to have little rationale by definition, the simplicity of the method belies a careful selection of every reactant used. Each

starting material, from the metal sources to the bases, is deliberately chosen with specific reasoning in mind. This is doubly true for the choice of ligand to be used in the reaction system. Recall from before that ligands are molecules that contain donor atoms, such as N and O, and that these ligands can act either as bridging/chelating ligands (L) or as terminal ligands (L′).[22] When a ligand acts as a bridging/chelating ligand, it aggregates the metal ions into a polynuclear motif, connecting metals through coordination bonds via its pairs of electrons in the valence shell of the donor atoms. This can lead to the isolation of very large and aesthetically pleasing metal clusters.[23] However, it is sometimes not enough to only add a bridging/chelating ligand. If the resulting metal cluster is too large, the cluster may come out of solution too quickly, preventing crystallization and thus removing the possibility of characterizing the structure through single-crystal X-ray crystallography. This is where terminal ligands may be employed. Terminal ligands are usually monodentate, occupying only one coordination site on a metal ion. These molecules are added to prevent excessive aggregation of the metal ions, blocking polymerization from occurring to target for single-crystal materials. When designing a synthetic route towards the isolation of new polynuclear metal complexes, a chemist must take into advantage this knowledge, and can come up with a ligand system that can best serve the problem at hand.

Many different types of bridging ligands are used in polynuclear metal complexes. Figure 1.10 shows some representative examples of organic bridging ligands used in polynuclear metal cluster chemistry.[24] These ligands range from the most simplistic (carboxylates, alcohols, etc.) and move onwards to some more complex ligands (Schiff bases, oximes/dioximes, etc.). The important feature of all of these molecules is their flexibility when it comes to coordinating to a large number of metal ions.

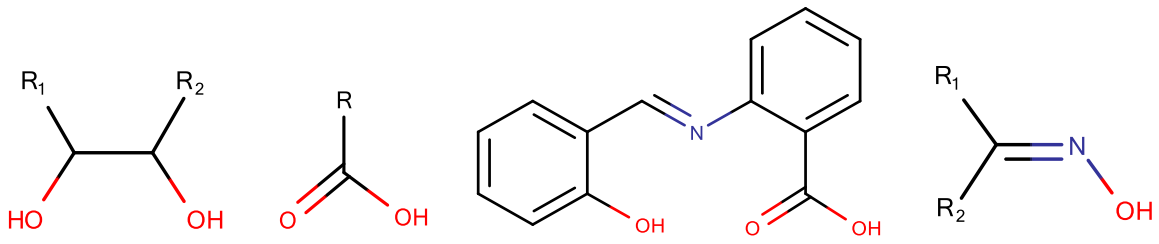

Figure 1.10. Some representative examples of ligands that are commonly employed in polynuclear metal cluster chemistry. From left to right: substituted diols, substituted carboxylates, Schiff bases and substituted oximes. Reproduced from Ref. 24.

More specifically, in the context of this thesis, two different families of organic bridging/chelating ligands were employed. The first family of these ligands is the diols. Scheme 1.1 shows some representative examples of diols that have been previously used in metal cluster chemistry, as well as the ligand that was employed for the first chapter of this thesis, naphthalene-2,3-diol (ndH_2). These ligands possess two O donor atoms, both of which can be deprotonated to allow the ligand to coordinate up to a potential five metal ions. Furthermore, the ligand ndH_2 has the ability to also chelate metal ions, forming a 5-membered chelate ring upon coordination of a metal ion by using both of the O-donor atoms. The nature of the donor atoms is also important. O-donor atoms are considered as hard Lewis bases, and thus prefer coordination to hard Lewis acids, according to the Hard Soft Acid Base theory. As such, O atoms prefer metals in moderate to high oxidation states (+2 and larger).[25] This confirms that ndH_2 and its deprotonated forms (ndH^-/nd^{2-}) can potentially bind to transition metal ions. Furthermore, lanthanide ions are well documented as oxophilic metal ions, preferring coordination with O-donors over N-donor atoms. This makes ndH_2 and its deprotonated forms (ndH^-/nd^{2-}) good

ligand systems for coordination to 4*f*-metal ions as well as transition metals in moderate to high oxidation states.[25]

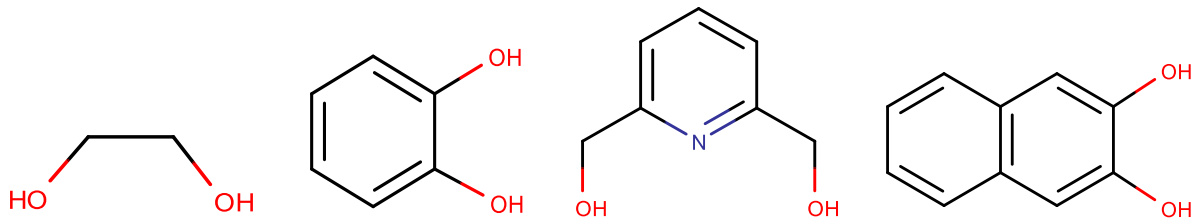

Scheme 1.1. Examples of diols that have been used in polynuclear metal cluster chemistry. From left to right: ethylene glycol (egH_2), catechol ($catH_2$), pyridine-2,6-dimethanol ($pdmH_2$), naphthalene-2,3-diol (ndH_2).

The ligand ndH_2 has been previously employed in 4*f*-metal cluster chemistry, as well as in 3*d*/4*f*-metal cluster chemistry. Figure 1.11 shows an example of a structure synthesized through the use of ndH_2 in homometallic 4*f*-metal cluster chemistry.[26] Reported by Stamatatos and coworkers, the combination of $Ln(NO_3)_3{\cdot}6H_2O$, ndH_2 and Et_4NOH in a 2:1:2 ratio in MeCN yielded a new family of octanuclear clusters with formula $(Et_4N)_4[Ln_8O(nd)_8(NO_3)_{10}(H_2O)_2]$, where Ln^{III} was Eu^{III}, Gd^{III}, Tb^{III}, and Dy^{III}, and nd^{2-} is the double-deprotonated form of naphthalene-2,3-diol. The magnetic interactions found in this complex were shown to be antiferromagnetic in nature, but the anisotropy of the $\{Dy_8\}$ analogue led to the complex to act as an SMM. While the SMM properties most likely arose from the single-ion effects of the individual Dy^{III} ions, this research was a first step in showing the excellent bridging and chelating abilities of the ndH_2 ligand.

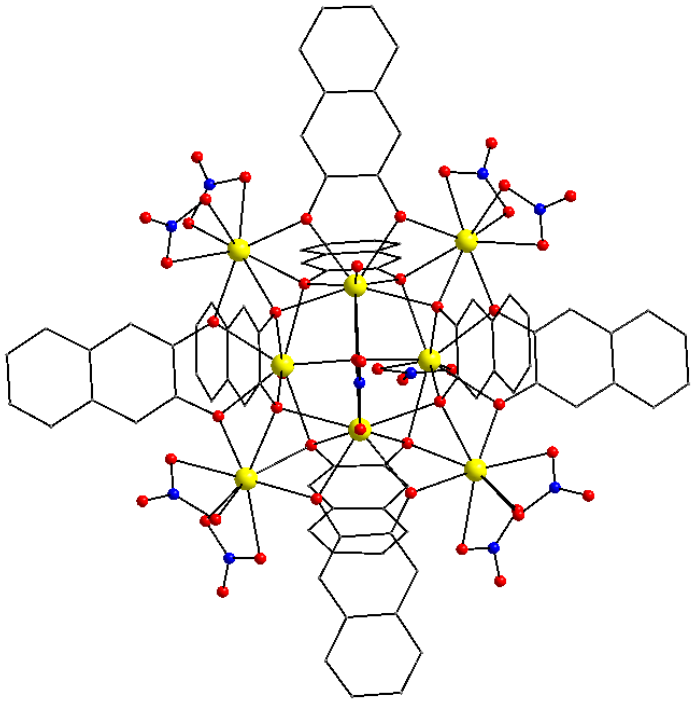

Figure 1.11. Structure of the {Ln_8} cluster, as reported by Stamatatos and coworkers. H atoms are omitted for clarity. Colour scheme: Ln^{III}, yellow; O, red; N, blue; C, grey. Reproduced from Ref. 26.

Figure 1.12 presents an example of ndH_2 employed in 3*d*/4*f*-metal cluster chemistry.[27] Through the use of $M(NO_3)_2{\cdot}6H_2O$ and $Ln(NO_3)_3{\cdot}6H_2O$ (M^{II} = Co^{II}, Ni^{II}, Zn^{II}; Ln^{III} = Gd^{III}, Dy^{III}) in equimolar amounts, with two equivalents of ndH_2 and Et_3N in $MeCN/Et_2O$, a family of isoskeletal complexes with the general formula $[M_6Ln_6(NO_3)_6(nd)_{12}(H_2O)_x(MeCN)_y]$ was synthesized, where *x* and *y* are variable among the different complexes. These complexes exhibited predominant antiferromagnetic interactions between the 3*d* and 4*f* metal ions, but the {Ni_6Dy_6} and {Zn_6Dy_6} analogues revealed out-of-phase *ac* magnetic susceptibility signals, again arising from the single-ion effects of the highly anisotropic Dy^{III} ions. These results

showed that ndH$_2$ could be successfully employed in 3*d*/4*f*-metal cluster chemistry. Furthermore, these results begged the question if this ligand could be employed successfully in Cu^{II}/Ln^{III} metal cluster chemistry and if the resulting complexes would be similar to the previously obtained or totally new.

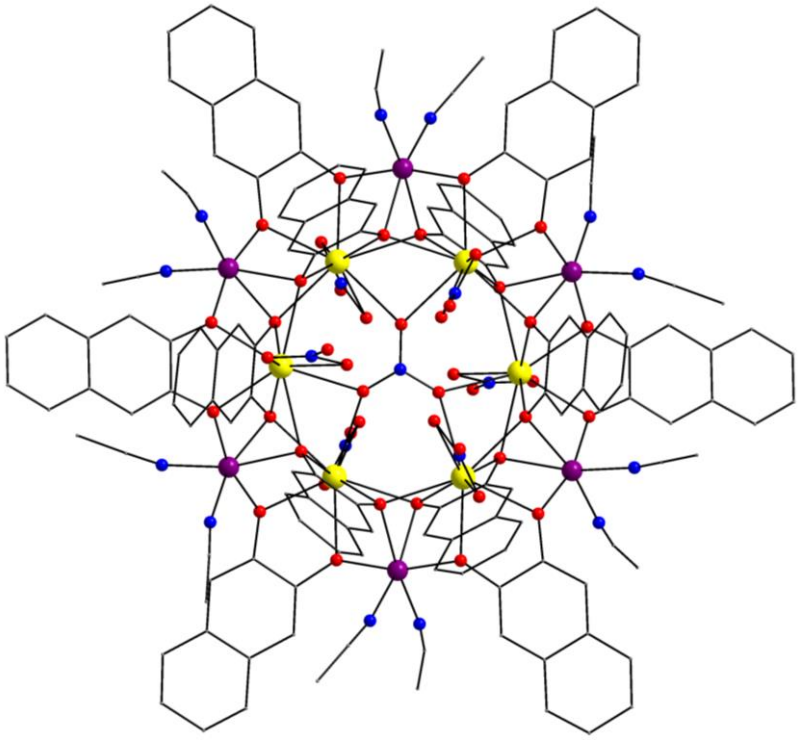

Figure 1.12. Structure of {M_6Ln_6}, where M = Co^{II}, Ni^{II}, and Zn^{II}, while Ln = Gd^{III} and Dy^{III}. H atoms have been omitted for clarity. Colour scheme: M^{II}, purple; Ln^{III}, yellow; O, red; N, blue; C, grey. Reproduced from Ref. 27.

Another family of organic chelating/bridging ligands that has received considerable attention in recent years is the family of oximes and dioximes. Scheme 1.2 shows many examples of different oxime and dioxime ligands. When there are aldehyde or ketone groups present in an organic molecule, a reaction can take place in the presence of hydroxylamine to convert the

aldehyde or ketone groups to oximes.[28] For dioximes, two of these functionalities must be present and two equivalents of hydroxylamine must be used to prevent synthesis of solely the monoxime. The use of bulky dioximes is of particular interest in polynuclear metal cluster chemistry for a few reasons. Firstly, dioximes have been found to enhance the solubility of cluster compounds in both polar and non-polar solvents.[29] This is important towards the isolation of crystalline materials, where a wide variety of different solvents may need to be tested in order to isolate the desired crystals. Oximes and dioximes have also been shown to promote strong magnetic coupling when bridging multiple metal ions together.[30] There is the potential for these interactions to be also ferromagnetic, which is extremely important for a variety of different properties like single-molecule magnetism and the magnetocaloric effect (discussed in detail later on). Furthermore, many different oximes are not commercially available. Since the synthesis of oximes and dioximes is well established, researchers can readily make new oximes and dioximes that have not been previously employed in polynuclear metal cluster chemistry. Due to this, there is a large gap in which many new ligand systems could arise as potential candidates towards the isolation of new polynuclear metal complexes with unprecedented structural motifs and interesting physicochemical properties.

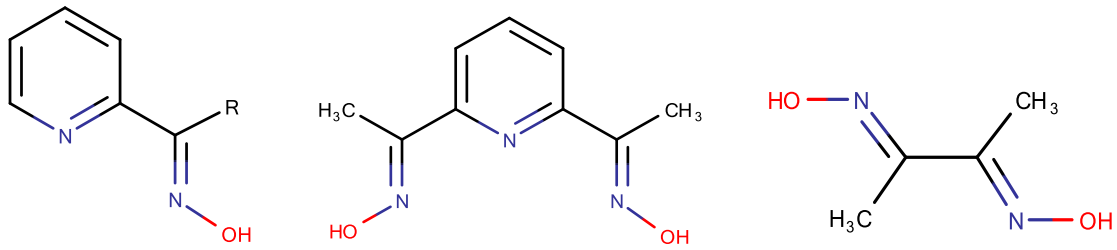

Scheme 1.2. Examples of oximes and dioximes that have been used previously in polynuclear metal cluster chemistry. From left to right: 2-pyridinealdoxime (paoH), 2,6-diacetylpyridine dioxime (dapdoH_2), dimethylglyoxime (dmgH_2).

Oximes and dioximes have been employed to great success in polynuclear metal cluster chemistry, as outlined in an extensive review by Milios, Stamatatos, and Perlepes.[31] Some representative examples of clusters are shown here. In 2010, Perlepes, Christou, and coworkers reported a new complex through the employment of the ligand 2-pyridinealdoxime (paoH).[32] The reaction of $Ni(ClO_4)_2 \cdot 6H_2O$, $Dy(NO_3)_3 \cdot 6H_2O$, paoH, and NaOMe, in a 1:1:3:3 ratio in MeOH yielded the structure shown in Figure 1.13, with the formula $[Ni_8Dy_8O(OH)_4(pao)_{28}](ClO_4)_5(NO_3)$. The organic pyridyl oxime ligand was found to take on three different binding modes, always forming a 5-membered chelate ring and further bridging through the deprotonated O atom of the oximate group (Figure 1.13). Furthermore, although the complex exhibited predominant antiferromagnetic exchange interactions between the metal ions, it was still found to act as an SMM. The capabilities of this oxime-based ligand to form such an interesting cluster lead to further work involving oxime-based ligands.

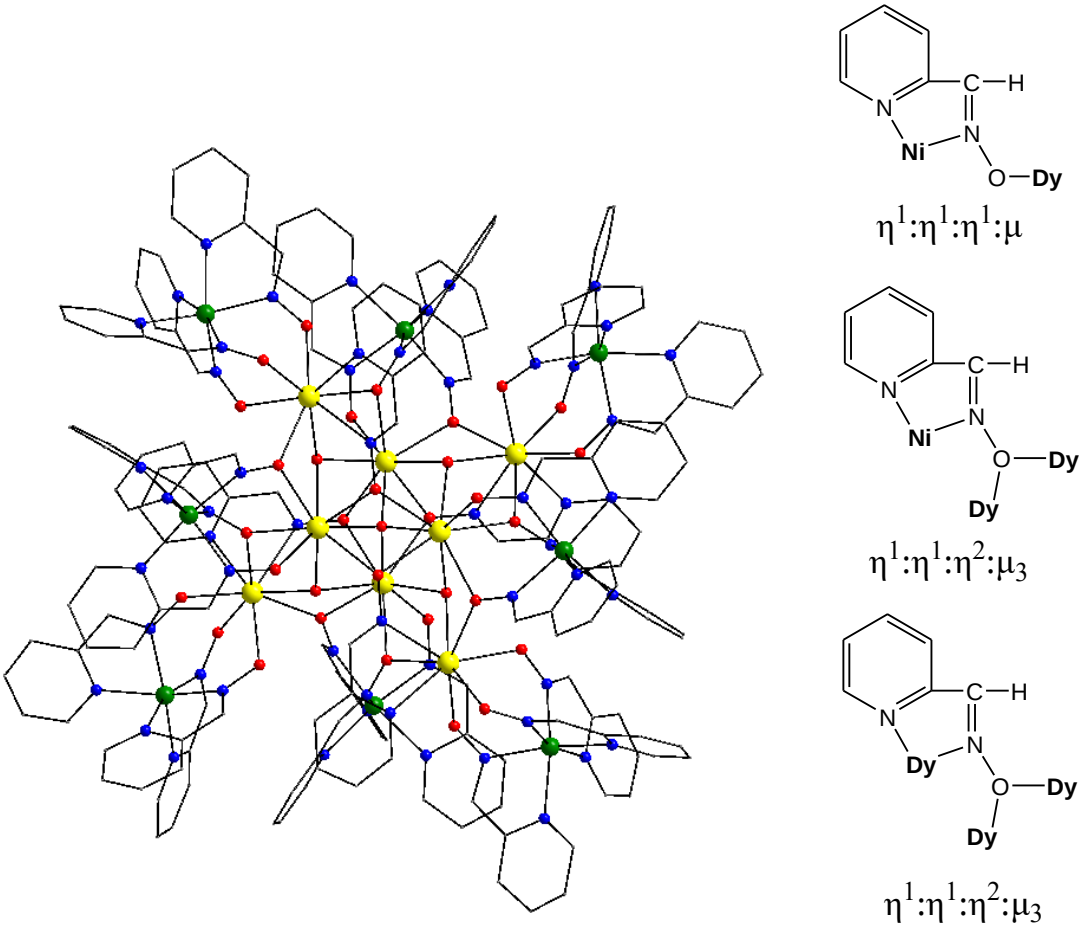

Figure 1.13. (left) Structure of the $\{Ni_8Dy_8\}$ cluster reported by Perlepes, Christou, and coworkers, and (right) the crystallographically established coordination modes of the pao^- ligands present in complex $\{Ni_8Dy_8\}$. H atoms are omitted for clarity. Colour scheme: Dy^{III}, yellow; Ni^{II}, green; O, red; N, blue; C, grey. Reproduced from Ref. 32.

Dioximes can also lead to interesting structures as well. One of the most widely used and representative examples of the family of dioxime ligands is the 2,6-diacetylpyridine dioxime ($dapdoH_2$, Scheme 1.2). With its ability to form two 5- or 6-membered chelate rings (depending on the donor atoms involved into the binding), as well as a vast bridging potential upon deprotonation of both O atoms, it has been employed in many different types of chemistry,

ranging from homometallic 3*d*- and 4*f*- to heterometallic 3*d*/4*f*-metal cluster chemistry. For example, in 2009, Christou and coworkers reported an unusual structure through the employment of $dapdoH_2$ in Mn/Gd chemistry, as shown in Figure 1.14.[33] The use of $Mn(O_2CPh)_2{\cdot}2H_2O$, $Gd(NO_3)_3{\cdot}6H_2O$, $dapdoH_2$, and Et_3N in a 1:1:2:4 ratio in MeCN yielded an unusual triangle-like structure with the formula $[Mn^{IV}Gd^{III}_2O(O_2CPh)_3(O_2CMe)(dapdo)(dapdoH)_2]$. These results demonstrated not only the ability of $dapdoH_2$, in its single- and double-deprotonated forms, to bridge transition metal ions and lanthanides, but also that the magnetic coupling through these dioximate bridges is of great interest. It was found that the complex displayed both ferromagnetic and antiferromagnetic exchange interactions between the Mn^{IV}-Gd^{III} and Gd^{III}-Gd^{III} pairs as propagated by oximate and carboxylate groups, respectively. This shows that the magnetic coupling through dioxime type ligands could conceivably lead to ferromagnetic interactions, which is of great importance to this research.

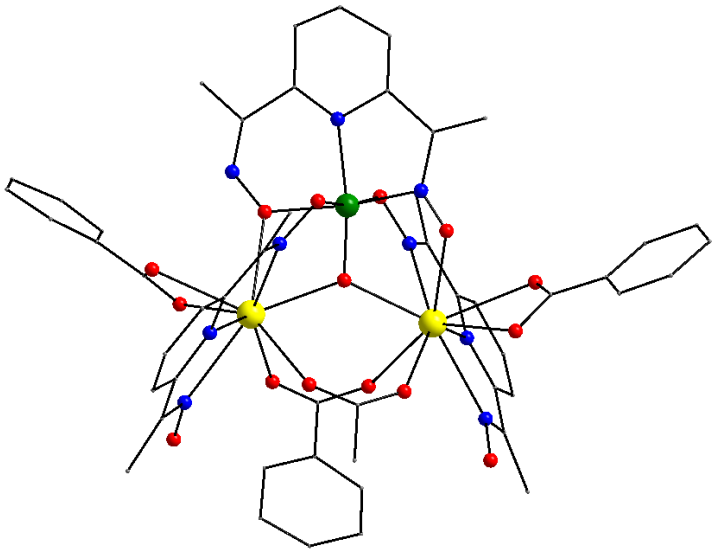

Figure 1.14. Structure of the $\{Mn^{IV}Gd^{III}_2\}$ cluster, reported by Christou and coworkers. H atoms are omitted for clarity. Colour scheme: Gd^{III}, yellow; Mn^{IV}, green; O, red; N, blue; C, grey. Reproduced from Ref. 33.

Other dioximes have also been used in 3*d*/4*f*-metal cluster chemistry. In 2008, Ishida and coworkers presented results employing the ligand dimethylglyoxime ($dmgH_2$). $[Cu(dmgH)_2]$, $[Dy(hfac)_3(H_2O)_2]$, and KOH were dissolved in $MeOH/Me_2CO$, yielding crystals of a new structure with the formula $[\{Dy(hfac)_2(MeOH)\}_2\{Cu(dmg)(dmgH)\}_2]_n$ (Figure 1.15).[34] The complex was found to act as a single-chain magnet, a class of superparamagnetic-like complexes similar to single-molecule magnets. The interesting feature of this work is that it displayed the capability of dioximes to yield not only 0-D discrete cluster compounds, but also 1-D coordination polymers based on repeating units which are small in nuclearity metal clusters.

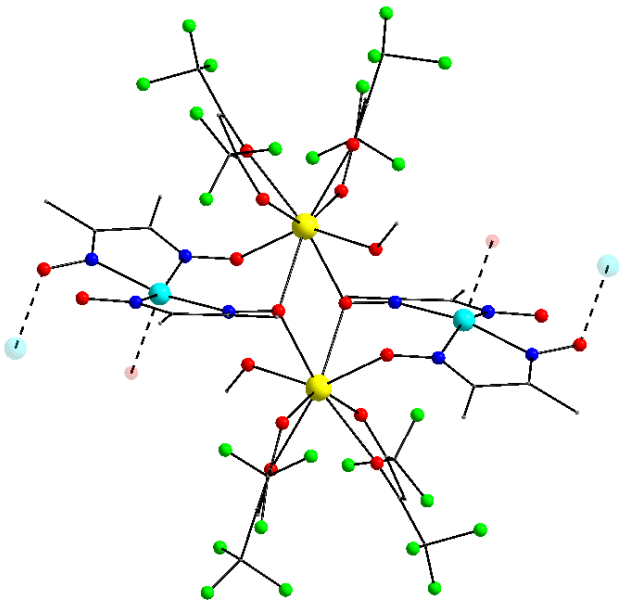

Figure 1.15. Structure of the $\{Cu_2Dy_2\}$ repeating unit within the 1-D chain-like complex $[\{Dy(hfac)_2(MeOH)\}_2\{Cu(dmg)(dmgH)\}_2]_n$, reported by Ishida and coworkers. H atoms are omitted for clarity. Extension points of the 1-D chain are indicated by the hashed bonds and the transparent atoms. Colour scheme: Dy^{III}, yellow; Cu^{II}, cyan; O, red; N, blue; F, green; C, grey. Reproduced from Ref. 34.

Both diol- and dioxime-type ligands have been used to isolate many different structures that have interesting physical properties. When paramagnetic metals are present, the metals can magnetically interact through the donor atoms. This leads to a net magnetic moment and consequently a spin ground state. However, to discuss the interactions that can lead to the interesting magnetic properties in polynuclear metal clusters, first a discussion regarding the principles of molecule-based magnetism should be undertaken.

1.4. Fundamentals of Molecular Magnetism

The study of polynuclear metal complexes has implications in many different fields of research. Delving particularly into the field of magnetism, single molecules that can act as magnets hold important implications in the development of new technologies, such as quantum computers and spintronic devices.[35] To be able to talk accurately about these properties, a discussion about magnetism must first be undertaken.

Magnetic properties are a consequence of the movement of electrons in their respective orbitals. The movement of the electrons consists of two different components. The first of these is the spin of the electron itself, called the spin angular momentum, *S*. When described as a spherical particle, the electron can be imagined as having a rotation, which gives rise to this value of *S*. The second component is the orbital itself, giving rise to the orbital angular momentum, *L*.[36] Recall that electrons are contained within an orbital of a given atom, and that the atom and consequently its orbital has a momentum associated with it as well. The movement of the electron, which is a charged particle, produces a small magnetic moment. If there are multiple electrons present in the atom, the vector sum of all of the individual magnetic moments

gives rise to the total magnetic moment of the atom. The orbital angular momentum has implications with regards to the spin-orbit coupling effect, which will be discussed at a later point.

Whether it is on the atomic scale, the molecular scale, or the bulk scale, all materials are influenced in some way by an external magnetic field. This property is called "volume magnetic susceptibility", denoted by the symbol χ_v.[37] Defined properly, the magnetic susceptibility is the magnetization of a given species when introduced to an external magnetic field. It is a dimensionless quantity, and is described by Equation 1.1.

$$\chi_v = \frac{M}{H} \qquad \textbf{(Eqn. 1.1)}$$

The magnetization is defined by *M*, and the external magnetic field is defined by *H*. When the values of *H* are small, χ_v acts independently of the external magnetic field, and accurate depictions of the susceptibility can be determined. Furthermore, the value of χ_v can be modified to give a more accurate depiction of the susceptibility, through the knowledge of the density of the species, and its molecular weight. Equations 1.2 and 1.3 describe the mass susceptibility (χ_g) and the molar susceptibility (χ_M), respectively.

$$\chi_g = \frac{\chi_v}{d} \qquad \textbf{(Eqn. 1.2)}$$

$$\chi_M = \chi_g \cdot MW \qquad \textbf{(Eqn. 1.3)}$$

In Equation 1.2, *d* describes the density of the species, and the units of χ_g is $cm^3\ g^{-1}$. In Equation 1.3, *MW* describes the molecular weight (molar mass) of the species in $g\ mol^{-1}$, which leads to χ_M possessing units of $cm^3\ mol^{-1}$.

The magnetic susceptibility, χ, can be further divided into two terms, shown in Equation 1.4. The magnetic susceptibility consists of the χ^D and χ^P, which represent the diamagnetic susceptibility and paramagnetic susceptibility, respectively.[38]

$$\chi = \chi^D + \chi^P \qquad \textbf{(Eqn. 1.4)}$$

Diamagnetism is a property that is present in all matter, even paramagnetic species. It arises from the interactions of oppositely paired electrons in an orbital. Recall that a total magnetic moment is the vector sum of the individual magnetic moments of the electrons. Since paired electrons in an orbital have opposite spins, their magnetic moments cancel out, resulting in a net magnetic moment of zero. As a result, diamagnetic compounds experience repulsion towards external magnetic fields, due to their tendency to move towards areas of lower field strength. The diamagnetic contributions in a compound can be calculated using Pascal constants which are standard values that are different for not only different types of atoms, but also different types of bonds. However, in paramagnetic compounds, the χ^P term is so much larger than the χ^D term, that it overwhelms the diamagnetic susceptibility in terms of magnitude. Opposite to diamagnetic compounds, paramagnetic compounds experience an attraction towards external magnetic fields. Paramagnetism is exhibited by matter that has a number of unpaired electrons present in an atomic or molecular orbital. This leads to a net magnetic moment in the compound, and is often a temperature-dependent property.

Bulk magnetic properties describe the interactions of many different spin carriers in a given material, and can be divided into a few different terms: 1) paramagnetism; 2) ferromagnetism; 3) antiferromagnetism; and 4) ferrimagnetism. Magnetic susceptibility studies can be used to

elucidate what magnetic properties are present. These different forms of magnetism are shown in Figure 1.16.[39]

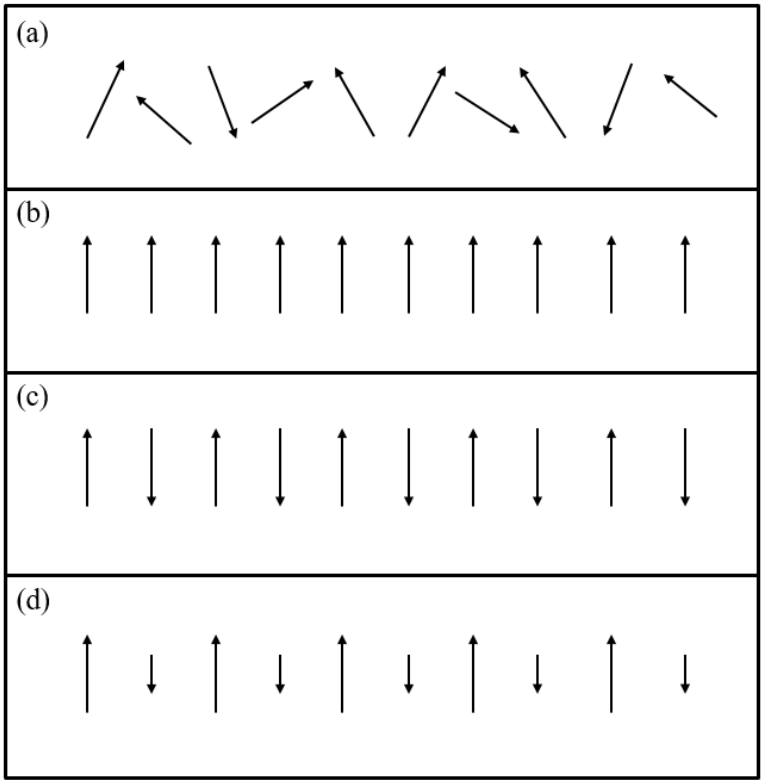

Figure 1.16. Different forms of magnetism exhibited in bulk materials: (a) paramagnetism; (b) ferromagnetism; (c) antiferromagnetism; and (d) ferrimagnetism. Reproduced from Ref. 39.

Paramagnetism, as described before, is a magnetic behaviour exhibited by compounds with unpaired electrons. However, since the net magnetic moment is a vector sum of the magnetic moments of the unpaired electrons, a paramagnetic compound consists of spins with random orientations, and the spins in the species do not interact with each other. Due to the random nature of the spins, there is no net magnetic moment in the compound, but in the presence of an external magnetic field, the spins will align parallel with the field, resulting in an attraction to the magnetic field. The magnetic susceptibility of a paramagnetic material is both field- and

temperature-dependent, as shown in Equations 1.1 and 1.5, respectively. The Equation 1.5 is also known as the Curie law.[39]

$$\chi_{\mathrm{M}} = \frac{N_{\mathrm{A}} g^2 \mu_{\beta}^2}{3 k_{\beta} T} S_{\mathrm{i}}(S_{\mathrm{i}} + 1) \qquad \textbf{(Eqn. 1.5)}$$

In this equation, N_{A} is Avogadro's constant, g is the Landé g-factor, μ_{β} is the Bohr magneton, k_{β} is the Boltzmann constant, T is the temperature, and S_{i} is the spin quantum number. S_{i} is equal to the number of unpaired electrons present in the species divided by 2. N_{A} has a value of 6.022×10^{23} mol^{-1}, μ_{β} has a value of 9.274×10^{-24} J T^{-1}, and k_{β} has a value of 1.380×10^{-23} J K^{-1}. The Landé g-factor is described by Equation 1.6, where S is the spin angular momentum, L is the orbital angular momentum, and J is the total angular momentum of the species. The value of g for a free electron is approximately 2.00, and is commonly used as an approximation for calculating the χ_M.

$$g = \frac{3}{2} + \frac{S(S+1) - L(L+1)}{2J(J+1)} \qquad \textbf{(Eqn. 1.6)}$$

Equation 1.5 can be further simplified to a form that is more commonly seen (Equation 1.7).

$$\chi_{\mathrm{M}} = \frac{C}{T} \qquad \textbf{(Eqn. 1.7)}$$

In the above equation, C is defined as the Curie constant. The Curie constant consists of all the terms in Equation 1.5, except for the temperature. Therefore, this is a material-dependent constant. The importance of this equation is the demonstration of the dependence of χ_{M} with the T. As the temperature of the species decreases, the molar susceptibility will consequently increase in a paramagnetic material.

The magnetization of a paramagnetic material is also a field-dependent term. This is demonstrated in the magnetization versus field plot shown in Figure 1.17.[40] At low field values, the magnetization shows a linear dependence on the field, rationalized through the rearrangement of Equation 1.1. However, at higher field values, the magnetization plateaus even while the field increases. This magnetization value is called saturation of magnetization, M_s, and is described by Equation 1.8.

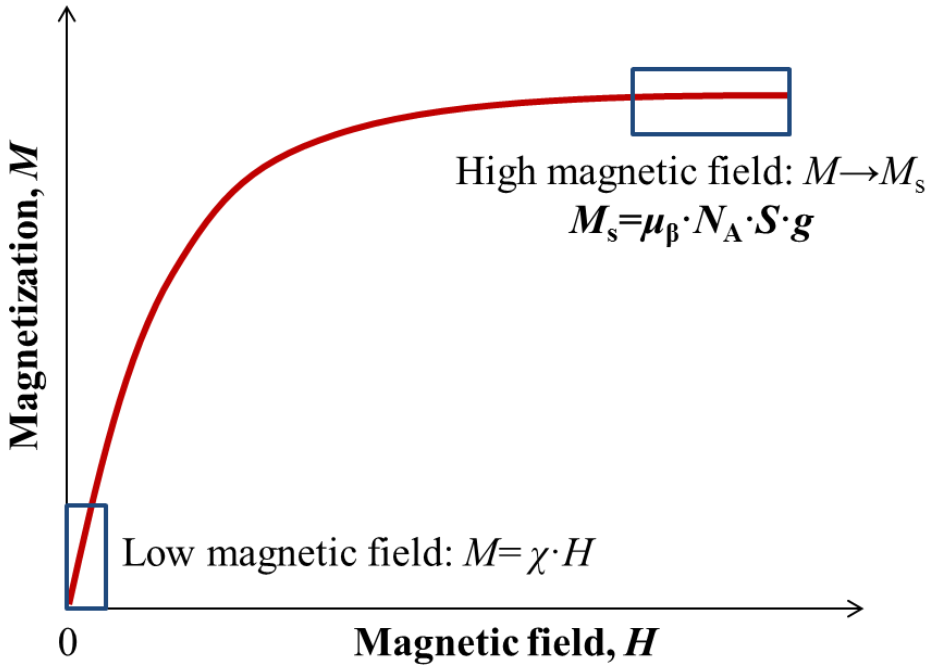

Figure 1.17. Example of *M* versus *H* plot. At small external magnetic fields, the magnetization behaves linearly. At large external magnetic fields, the magnetization plateaus, denoting saturation of the magnetization. Reproduced from Ref. 40.

$$M_s = \mu_\beta N_A S g \qquad \textbf{(Eqn. 1.8)}$$

When magnetization versus field data is plotted, it is common to divide the magnetization by $\mu_\beta N_A$, yielding Equation 1.9, which describes the reduced magnetization. This equation allows for the confirmation of a spin ground state for a given paramagnetic species, which is important for other magnetic properties like the energy barrier to the magnetization reversal and the magnetic entropy (*vide infra*).

$$\frac{M_s}{\mu_\beta N_A} = Sg \qquad \textbf{(Eqn. 1.9)}$$

Paramagnetism becomes a more complex property when the individual spin carriers interact magnetically, leading to either ferromagnetic, antiferromagnetic, or ferrimagnetic interactions. In ferromagnetically-coupled materials, the spin carriers of the material all possess spins that are aligned parallel with one another. This yields a large net magnetic moment, and the material will experience a strong attraction to an external magnetic field. However, there is a caveat to note about bulk ferromagnetic materials; this is the presence of magnetic domains in the material. While the material may be overall ferromagnetic, there may be a number of domains present in the material, all of which may have different orientations of the aligned spins.[40] Therefore, it is conceivable that a paramagnetic material that possesses ferromagnetic domains may exhibit a net magnetic moment of zero, if the domains cancel each other out. The domains remain randomly aligned outside of an external magnetic field, but upon introduction of an external field, the domains will all align parallel with the field, resulting in the attractive force discussed previously. Antiferromagnetic materials possess spin carriers that have repeating equal and opposite spin values, usually resulting in a net magnetic moment of zero.[40] Upon introduction of the material to an external magnetic field, the antiferromagnetic material experiences a repulsion

against the field, exhibiting similar behaviour to diamagnetic compounds, even though the material is paramagnetic. Finally, ferrimagnetic materials have similarities with both ferromagnetic and antiferromagnetic materials. While the spin carriers in the material have their spins aligned in opposite directions, the magnitude of these spins are different, yielding a net magnetic moment that is smaller than a purely ferromagnetic material comprising identical components. Ferrimagnetic compounds can also exist in domains, similar to ferromagnetic compounds, which give rise to the potential for the domains to cancel each other out, leading to a net magnetic moment of zero. Furthermore, similar to ferromagnetic materials, ferrimagnetic materials experience an attractive force when introduced to an external magnetic field. Ferromagnetic, antiferromagnetic, and ferrimagnetic materials all experience these interactions through long-range magnetic ordering. However, this ordering is a temperature-dependent property. These critical temperatures are called the Curie temperature (T_c, for ferromagnetic and ferrimagnetic materials) and the Néel temperature (T_N, for antiferromagnetic materials). Above these critical temperatures, the materials act as paramagnetic materials, with their spins randomly aligned. This is because the thermal energy dominates over the magnetic ordering at temperatures higher than T_c and T_N. However, when the temperature of the material is brought below T_c or T_N, the long-range magnetic ordering reveals itself.

As mentioned previously, the magnetic susceptibility of a paramagnetic compound shows a dependence upon the temperature. This is commonly shown in a $\chi_M T$ versus T plot, where T is the temperature in Kelvin, and the $\chi_M T$ product possesses units of $cm^3\,mol^{-1}\,K$. Examples of how paramagnetic, ferromagnetic, antiferromagnetic, and ferrimagnetic materials behave at different temperatures is shown in Figure 1.18.[40,41]

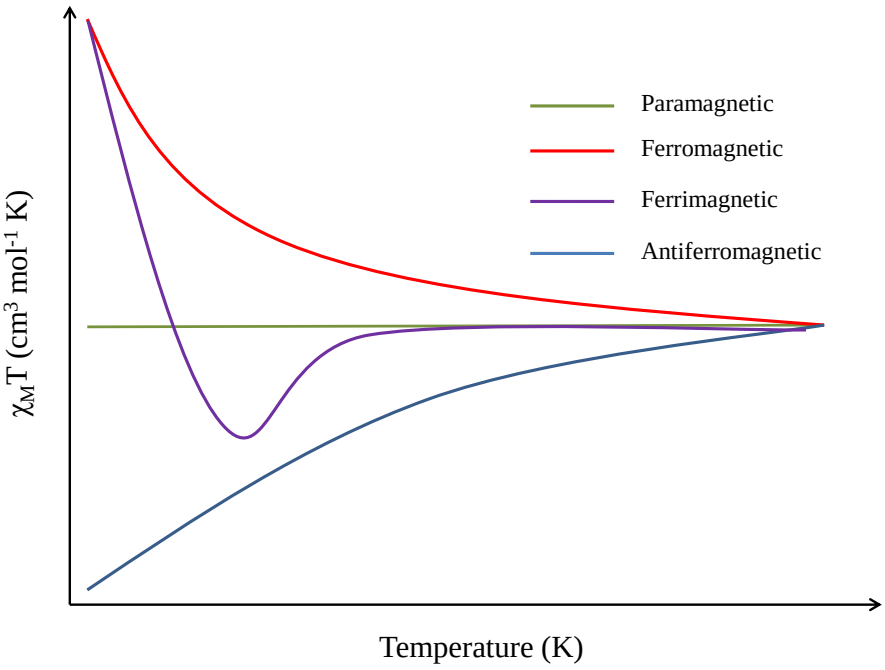

Figure 1.18. Behaviour of different magnetic materials, as shown through a $\chi_M T$ versus T plot. Reproduced from Ref. 40.

In a paramagnetic material, the $\chi_M T$ product remains constant, due to the lack of interactions between the individual spin carriers. Consequently, due to the long-range magnetic ordering in the other types of materials, there are deviations from the simple paramagnetic behaviour. Ferromagnetic materials experience an increase in the $\chi_M T$ product as the temperature decreases; antiferromagnetic materials see a decrease in the $\chi_M T$ product with decreasing temperature; the majority of ferrimagnetic materials will experience a decrease followed by an increase in the $\chi_M T$ as the temperature decreases. The value of the $\chi_M T$ is related to the spin quantum number of a given material, as related to Equation 1.10.[41]

$$\chi_M T = \frac{g^2}{8} S(S+1) \qquad \textbf{(Eqn. 1.10)}$$

Other relevant information can be determined through the plotting of χ_M^{-1} versus T (Figure 1.19).[41] In this plot, an ideal paramagnetic compound with no long-range magnetic ordering will exhibit a linear relationship passing through the origin of the plot. However, ferromagnetic, ferrimagnetic and antiferromagnetic compounds will show deviations from the ideal paramagnetic behaviour. This deviation of the χ_M^{-1} plots from the origin is defined by the Curie-Weiss law (Equation 1.11).

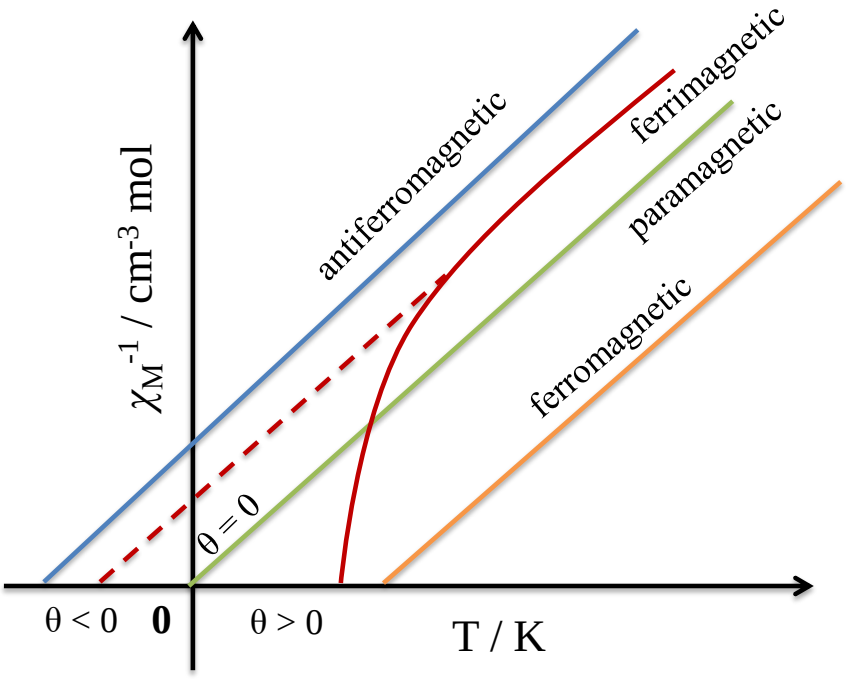

Figure 1.19. Sample χ_M^{-1} versus T plot, showing the effect of the Weiss constant on the magnetic susceptibility. Reproduced from Ref. 41.

$$\chi_M = \frac{C}{T-\theta} \qquad \textbf{(Eqn. 1.11)}$$

In the above equation, θ is the Weiss constant, and will take on different values depending on the long-range magnetic ordering. When θ is positive, the material shows ferromagnetic

ordering, and when θ is negative, the material shows antiferromagnetic ordering. This is further confirmed by the Equation 1.12.

$$\theta = \frac{zJ'S(S+1)}{3k_\beta} \qquad \textbf{(Eqn. 1.12)}$$

In the above equation, J' describes the intermolecular interactions (or magnetic ordering) in the bulk materials. This accounts for the deviations from the ideal paramagnetic case.

Understanding the magnetic properties of bulk materials is important for starting to understand magnetism on the molecular level. However, magnetism is not just affected by temperature and external field. The magnetism of a material, particularly a molecule-based material, has a directional dependence as well. This is called magnetic anisotropy, and is described as a preferential orientation of the net magnetic moment along an axis. This is denoted as the "easy axis". In addition to the "easy axis" is the "hard plane", which is perpendicular to the "easy axis". Magnetic anisotropy is a result of the combination of the spin angular momentum of an electron with the orbital angular momentum of orbital which contains the electron. This combination is called spin-orbit coupling.

1.5. Spin-Orbit Coupling and Magnetic Anisotropy

The field of quantum mechanics has advanced quite far in terms of describing the different sorts of phenomena that can occur at the molecular level. From initially describing the shape of the sole orbital of a hydrogen atom to more complex systems involving *p* and *d* orbitals, to describing molecular orbitals as combinations of atomic orbitals and onwards. Quantum mechanics has also helped account for various spectroscopic phenomena, such as the absorption

spectra of atoms and molecules as well as their emission features in band and line spectra. However, when the field was still emerging, only the most intense and characteristic bands of the spectra could be defined, leaving much to be discovered. As the resolution of spectroscopic technology improved, in addition to the development of new spectroscopic techniques, more spectral features were found. These new features possessed shifts to different wavenumbers that could not be accounted for by the equations used at the time, so new formulas needed to be derived. A bit of information was already known by this point. In particular, it was known that an electron possessed a spin, and therefore an angular momentum existed, called *S*. It was also known that the orbitals of an atom also possessed their own angular momentum, called *L*. It was through the use of this information that in 1923, Russell and Saunders suggested that these two different angular momenta interact with each other, essentially coupling and sharing energy.[42] Such type of interaction, dubbed as LS coupling, was also known as the spin-orbit coupling of an atom.

The spin-orbit coupling parameters always take the form of a term symbol, according to the formulation ${}^{(2S+1)}L_J$.[43] In this case, the *S* is the total spin angular momentum of the electrons, *L* is the total orbital angular momentum and *J* is the overall angular momentum of the system itself. An example of how the orbits interact in LS coupling can be seen in Figure 1.20.[44] The value of *S* is determined from the sum of the spins of the individual electrons, which all possess an $m_s = \pm 1/2$. The value of *L* is determined through the sum of the individual orbital angular momenta. These values are assigned to the free ion and can be determined from the orbital splitting diagram; an example can be seen in Figure 1.21.[43] Finally, the value of *J* can be also elucidated, but it has some prerequisites to follow. If the orbitals of the free ion are less than half-filled, that is, for instance, less than n = 3 electrons for *p* orbital systems or less than n = 5 for *d* orbital

systems, then $J = |L\text{-}S|$. However, if the opposite case occurs, then $J = L+S$. Finally, if $L = 0$, then $J = S$. This latter situation occurs in isotropic atoms with no orbital angular momentum, such as the Mn^{II} d^5 system and the Gd^{III} f^7 one.[45] Eventually, with all of these values calculated, a term symbol, $^{(2S+1)}L_J$, for an electronic configuration can be determined. Traditionally, the spin part is expressed as a "spin multiplicity", $(2S+1)$, which accounts for the number of spin-orbit states found in most cases. While $(2S+1)$ and J can be calculated, L will change based on its integer value. The form of L will be S, P, D, F, G, H, etc., corresponding to the values of L = 0, 1, 2, 3, 4, 5, and onwards. Therefore, using the example of Cu^{II}, which is a $3d^9$ metal ion, a term symbol of $^2D_{5/2}$ is derived (Figure 1.21). All transition metals and heavier metals will possess some form of this LS coupling scheme, which holds importance in the spectroscopic and magnetic properties of these metal ions.

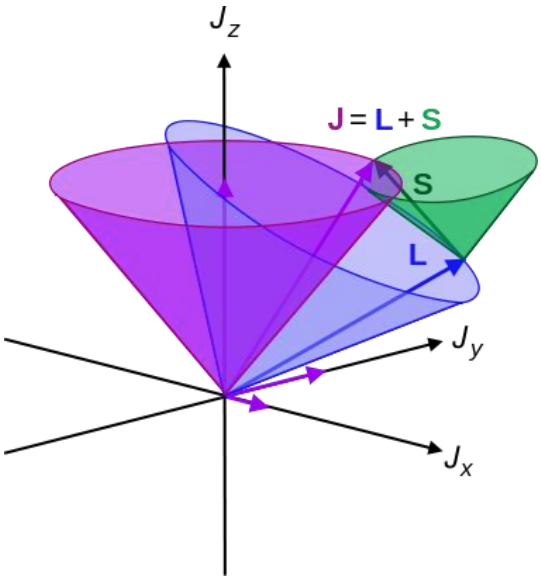

Figure 1.20. Graphical representation of the Russel-Saunders (LS) coupling scheme. The spin angular momentum (*S*, green) is summed with the orbital angular momentum (*L*, blue) to give the resulting overall angular momentum (*J*, purple). Adapted through Creative Commons License (Public Domain), Ref. 44.

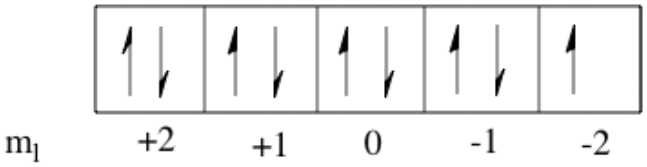

Figure 1.21. Representative example of calculating the value of *L*, using the degenerate *d* orbitals of a d^9 system. Reproduced from Ref. 43.

There are also different forms of spin-orbit coupling, named first- and second-order spin-orbit coupling. First-order spin-orbit coupling describes the interactions of the spin angular momentum and the orbital angular momentum that occur within the same atom, or in this case, a 3*d* metal ion. However, if different metal ions are brought within close enough proximity, there may be spin-orbit coupling effects between the two different metal ions. This is called second-order spin-orbit coupling, since it occurs within the second coordination sphere of a 3*d* metal as opposed to the first coordination sphere directly surrounding the metal centre.[46] While second-order spin-orbit coupling is usually very weak in energy terms, there are certain cases where it needs to be accounted for. For example, Gagliardi and coworkers showed that in a metal-organic framework involving Fe^{II} and a ligand called dobdc, where dobdc is 2,5-dioxido-1,4-benzenedicarboxylate, only using the first-order spin-orbit coupling term in theoretical calculations did not provide reliable data to describe the single-ion magnetic anisotropy.[46] However, upon introduction of the second-order spin-orbit coupling term, from two adjacent Fe^{II} ions, to the theoretical calculations, the values associated to the single-ion magnetic anisotropy were found to increase the accuracy of the calculations.[46] There are also some fundamental rules that dictate what kind of transitions between different orbitals can occur. One of these rules is the Laporte selection rule and the other is the spin selection rule.[43] The Laporte selection rule

dictates that $\Delta L = \pm 1$, meaning that the total orbital angular momentum of a system cannot change by more than 1 or -1 for an allowed transition, and all other transitions are forbidden.[43] For example, a transition from $^4D \rightarrow {}^4F$ is allowed, but a transition from $^4F \rightarrow {}^4P$ would be forbidden ($\Delta L = 1$ in first case, $\Delta L = -2$ in the second). Transitions may also occur from the $u \rightarrow g$ state or the $g \rightarrow u$ state, where "*g*" stands for "gerade" and "*u*" for "ungerade", but not from the $g \rightarrow g$ state and so on.[43] The spin selection rule goes on further and puts on prerequisites to the *S* and *J* values. The spin selection rule for the spin angular momentum, *S*, states that $\Delta S = 0$ for an allowable transition, or that only transitions to the same spin multiplicity are allowed to occur.[47] The spin selection rule for the overall angular momentum, *J*, is that of $\Delta J = 0$ or $\Delta J = \pm 1$, or that only transitions that retain the total angular momentum or only change it by ±1 are allowed.[43] All of these spin-orbit coupling interactions are responsible for the characteristic spectroscopic and physicochemical properties of coordination metal compounds.

Spin-orbit coupling has a few significant consequences on the spectral features of transition metals at a given oxidation state. It leads to a variety of different splitting patterns based on the spin multiplicity, as well as spectral shifts up- or down-field based on the nature of the metal, and the splitting of degenerate orbital states into different orbital splitting diagrams. Firstly, the splitting of energy states occurs when the degeneracy of orbitals is removed upon the addition of energy from an external source. In first-row transition metals, the spin-orbit coupling effect is quite small compared to the larger crystal field effects imparted by the crystal lattice and/or coordinating ligands; however, its effect is still large enough to be accountable.[48] The splitting of the orbitals relies on the total orbital angular momentum, and the sub-states to which it splits are transformed according to the irreducible representations (usually designated by Mulliken symbols) of a given symmetry point group. The irreducible representations are associated with

the symmetry point group. It is a general mathematical object, which can be applied to many systems, including molecular systems. The energy states are classified according to the irreducible representations of symmetry point groups and/or according to the total orbital angular momentum, when the corresponding Hamiltonian commutes with *L*. The latter is true for the spherical symmetry of a free ion, so one can classify the states according to the eigenvalues of *L*. Strictly speaking, this cannot be accurately considered for an ion in a field, where the classification by the irreducible representations still holds. However, a correlation can be established for relatively weak fields. These correlations are shown in Table 1.1.[43]

Table 1.1. Energy levels and their corresponding sub-states of orbital angular momentum.

Energy Level	Sub-states
S	A_1
P	T_1
D	$E + T_2$
F	$A_2 + T_1 + T_2$
G	$A_1 + E + T_1 + T_2$
H	$E + T_1 + T_1 + T_2$
I	$A_1 + A_2 + E + T_1 + T_2 + T_2$

What is important to emphasize at is the correlation of the total orbital angular momentum, or the projections of the total orbital angular momentum, with the generated irreducible representations. From the S level, the only sub-state comes from A_1, which is explained by the shape of the spherical orbital itself. The P level of energy is split to the T_1 sub-state, which is a

triply degenerate state of orbitals. These can be associated to the p_x, p_y, and p_z orbitals. Finally, the D energy level splits to the E and T_2 sub-states, which are related to the e_g and t_{2g} orbitals, for example, found in octahedral 3*d*-metal complexes. Table 1.2 summarizes the ground state angular momentum terms and the corresponding high-spin ground state irreducible representations in an octahedral geometry for various $3d^n$ metals.[49] It also contains the overall irreducible representations present in those electronic configurations once the spin-orbit coupling is accounted for. All these electronic details have direct implications to the spectroscopic, physicochemical and magnetic characteristics usually seen in the first row 3*d*-metal ions.

Table 1.2. Ground state angular momenta and irreducible representations of various 3*d*-metal ions.

Configurations	Ground State	HS Ground State in O_h	Spin in O_h	Degree of Splitting	Overall Symmetry in O_h
$3d^0$	$^1S_0$	$^1A_{1g}$	A_{1g}	1	A_{1g}
$3d^1$	$^2D_{3/2}$	$^2T_{2g}$	E_{2g}	2	$E_{1g} + G_g$
$3d^2$	$^3F_2$	$^3T_{1g}$	T_{1g}	4	$E_g + T_{1g} + T_{2g} + A_{1g}$
$3d^3$	$^4F_{3/2}$	$^4A_{2g}$	G_g	1	G_g
$3d^4$	$^5D_0$	^5E_g	$E_g + T_{2g}$	5	$A_{1g} + A_{2g} + E_g + T_{1g} + T_{2g}$
		$^3T_{1g}$	T_{1g}	4	$E_g + T_{1g} + T_{2g} + A_{1g}$
$3d^5$	$^6S_{5/2}$	$^6A_{1g}$	$G_g + E_{1g}$	2	$G_g + E_{1g}$
		$^2T_{2g}$	E_{2g}	2	$G_g + E_{1g}$
$3d^6$	$^5D_2$	$^5T_{2g}$	$E_g + T_{2g}$	6	$A_{1g} + E_g + T_{1g} + T_{1g} + T_{2g} + T_{2g}$
		$^1A_{1g}$	A_{1g}	1	A_{1g}
$3d^7$	$^4F_{9/2}$	$^4T_{1g}$	G_g	4	$E_{1g} + E_{2g} + G_g + G_g$
		^2E_g	E_{2g}	1	G_g
$3d^8$	$^3F_4$	$^3A_{2g}$	T_{1g}	1	T_{2g}
$3d^9$	$^2D_{5/2}$	^2E_g	E_{2g}	1	G_g

In the above table, the third column describes the ground state of a given $3d^n$ configuration when the metal ion is high spin; the fourth column gives the representation when the metal ion possesses O_h symmetry. The constants for the spin-orbit coupling of first-row transition metals have been calculated,[50,51] and can be used to calculate the energy needed to either help remove the degeneracy of the total orbital angular momentum or to shift the spectral bands shown, for instance, in absorption and emission spectroscopies. Table 1.3 shows the energy of the spin-orbit coupling of various first row transition metals at various oxidation state levels.[50] Values that are not within parentheses have been accurately determined through spectroscopic techniques while values in parentheses have been calculated by theoretical means. These values can be incorporated into various Hamiltonian equations used to account for the energy provided by the spin-orbit coupling effect. This has effects on various spectroscopic techniques such as electron paramagnetic resonance (EPR), X-ray magnetic circular dichroism (XMCD) and nuclear magnetic resonance (NMR). It can also have implications on properties such as the anisotropy of a metal ion, the magnetic coupling interactions between various metals, and charge-transfer interactions.

Table 1.3. Energies (in cm^{-1}) of spin-orbit coupling seen in selected transition metal ions at different oxidation states.

$3d^n$ oxidation state	0	1	2	3	4
Mn	250	(305)	350	400	465
Fe	350	405	(445)	(515)	585
Co	455	525	570	(640)	(720)
Ni	605	650	720	(790)	(880)
Cu		830	880	(960)	(1070)

EPR is a spectroscopic technique that is further affected by the spin-orbit coupling present in a metal ion. While it was mentioned before that the spin-orbit coupling is a small effect compared to the crystal field effects in terms of removing the orbital degeneracy in 3*d* transition metals, it must still be taken into account.[52] Figure 1.22 shows an example of the *d*-orbital splitting of a metal due to the crystal field effects and spin-orbit coupling.[53]

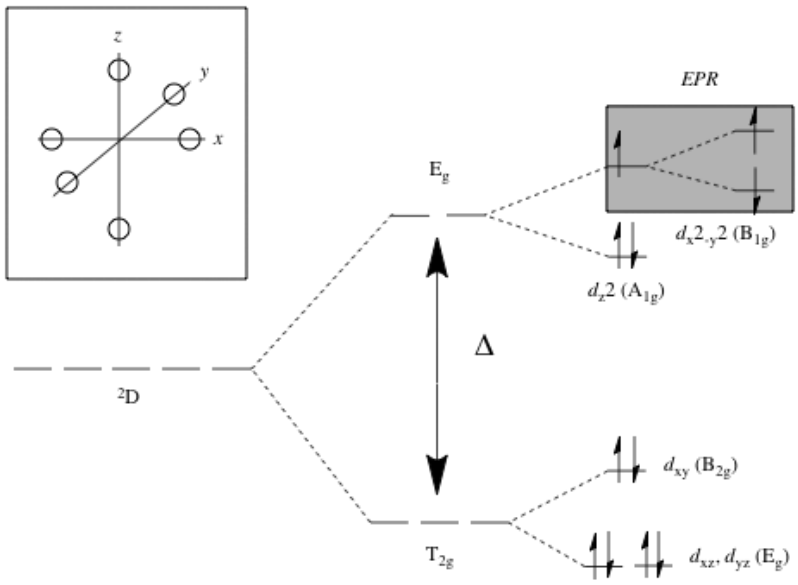

Figure 1.22. An example of an orbital splitting diagram due to crystal field effects and spin-orbit coupling in a d^9 system. Reproduced from Ref. 53.

It has also been shown that the EPR signals of certain metal ions depend on the electron spin and the overall symmetry of a system.[43] Figure 1.23 shows some representative EPR data for various 3*d*-metal ions.[43] One of the most striking comparisons comes from the Mn^{II} and Fe^{III} EPR data. Both of these ions are d^5 systems and experience spin-orbit coupling, which splits their respective spectra into five different lines. However, not only is the spin-orbit coupling important here, but so is the nuclear spin, or *I*, of the atom.[43] An interaction also occurs between the angular momentum of the nucleus and the angular momentum of the electrons, which gives rise to additional splitting of the spectral signals. In the case of Mn^{II}, the signal is firstly split into five distinct lines due to the $S = 5/2$, in accordance with the allowed transitions between the different spin states of the electron, but those five lines are further split due to the presence of a nuclear spin of $I = 5/2$. Each one of the five bands is further split into six lines due to this interaction.

However, in the case of Fe^{III}, there is no further splitting of the signal due to the lack of a nuclear spin, leaving only the $S = 5/2$ to split the signal into five discrete lines.

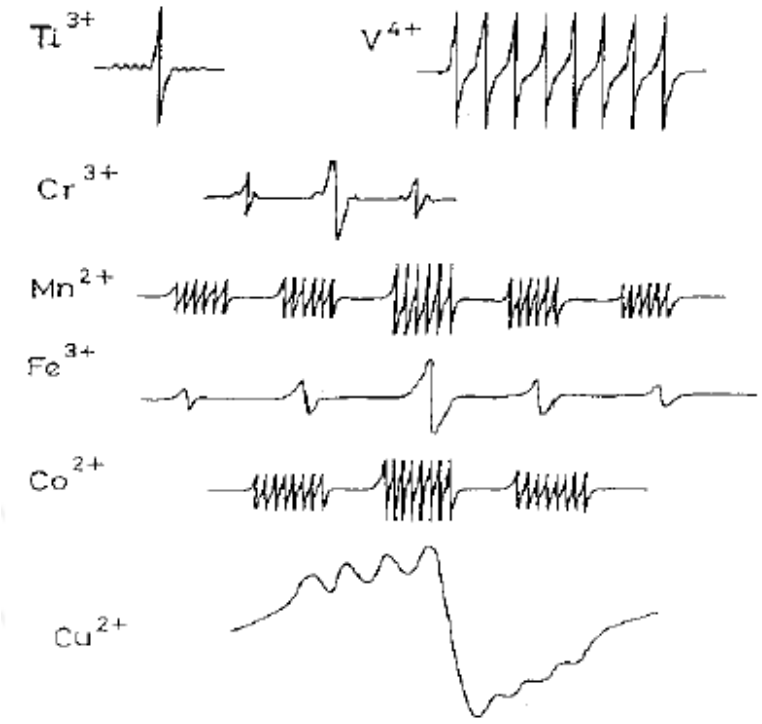

Figure 1.23. Characteristic EPR data of some $3d^n$ metal ions. Adapted from Ref. 43.

The spin-orbit coupling of a system can also have an effect on the magnetic anisotropy of a system, specifically in mononuclear transition metal-based single-ion magnets. It has been shown that in most cases involving first-row transition metal coordination complexes, the ligand field interactions usually reduce the strength of the spin-orbit coupling and consequently quench the orbital angular momentum and anisotropy of the system.[36] However, while this is true for metal complexes with large coordination numbers, it has been found that reducing the coordination number of a system, the contribution of the ligand field is weakened, which leaves

the spin-orbit coupling to act as the primary force affecting the magnetic anisotropy.[54] In 2009, Riordan and coworkers showed that a mononuclear Fe^{II} complex with only four donor atoms (3 S and 1 C) and a pseudotetrahedral geometry possesses a large and negative zero-field splitting parameter, *D*, which was calculated as -33 cm^{-1}.[55] This was attributed to the specific character of the lowest-lying orbitals, separated by an energy gap small enough to allow mixing through spin-orbit coupling; such type of mixing resulted in a negative zero-field splitting. In 2010, Long and coworkers also showed that spin-orbit coupling has an effect on the anisotropy of a system, this time however in conjunction with the use of heavy atom ligands and first-row transition metals.[56] They were able to show that octahedral, mononuclear Cr^{II} and Cr^{III} complexes showed enhanced anisotropy when a ligand with heavy auxiliary groups (i.e., Cl, Br, and I) was used. This effect occurs due to the spin-orbit coupling imparted by the heavy atoms in the ligands.

The property of spin-orbit coupling becomes even more pronounced when discussing heavy metals, such as the lanthanides. This is due to the electronic structure of the lanthanide itself. Lanthanides possess valence electrons in the 4*f* orbitals. However, these orbitals are localized in the inner shell, shielded by the 5*s* and 5*p* orbitals. This has implications on the magnitude of the spin-orbit coupling, as shown by Equation 1.13, which describes the spin-orbit coupling constant for hydrogen-like orbitals.[57]

$$\lambda = \frac{m_e}{2} Z^4 \alpha^4 c^2 \frac{1}{n^3\left(l+\frac{1}{2}\right)(l+1)} \qquad \textbf{(Eqn 1.13)}$$

In the above equation, λ is the spin-orbit coupling constant, m_e is the mass of an electron, *Z* is the effective nuclear charge, *c* is the speed of light, *n* is the number of unpaired electrons, *l* is the orbital angular momentum, and α is Sommerfield's fine-structure constant. As shown in the equation, the spin-orbit coupling is related to the *Z*, among other parameters. Consequently, if

effective nuclear charge increases (i.e., the electrons move closer to the nucleus and the mass of the element increases), then the magnitude of the spin-orbit coupling constant increases as well.[58] Therefore, it follows that the heavier the lanthanide ion, the stronger the spin-orbit coupling. Certain lanthanides, particularly Tb^{III} and Dy^{III}, have been of great interest in their potential to act as single-molecule magnets (*vide infra*). Table 1.4 describes some important constants of these two free lanthanide ions in particular.[59]

Table 1.4. Properties of free Tb^{III} and Dy^{III} ions.

Ln^{III}	$4f^n$	$^{2S+1}L_J$	ζ (cm^{-1})	g_J	$\chi_M T$ ($cm^3\ mol^{-1}\ K$)
Tb^{III}	$4f^8$	$^7F_6$	1709	3/2	11.82
Dy^{III}	$4f^9$	$^6H_{15/2}$	1932	4/3	14.17

In the above table, ζ describes the free-ion spin-orbit coupling constant, g_J is the Landé *g*-factor for the lanthanide ion, and $\chi_M T$ describes the magnetic susceptibility of the lanthanide ion at 300 K. Note that ζ is the one-electron spin-orbit coupling constant and is useful when comparing the relative magnitudes of spin-orbit coupling for different free ions. For ground states, the λ (which is the resultant spin-orbit coupling between the resultant spin magnetic moment and the resultant orbital moment for many electron ions) and ζ constants are simply related by: $\lambda = \pm \zeta/2S$, where S is the spin multiplicity of the ion. In practice, λ is what is usually measured, and the plus sign refers to d^1-d^4 ions whereas the minus sign refers to d^6-d^9 ions.

Spin-orbit coupling is an important parameter when discussing both 3*d*- and 4*f*-metal ions. Not only does this property have an effect on the spectroscopic properties of the metals, but also

has important implications when it comes to discussing the potential for metal cluster compounds to act as single-molecule magnets.

1.6. Single-Molecule Magnets

Up to this point, the discussion has fallen primarily on the basic principles of magnetism that is found in bulk materials. While these features are important for the determination of what types of magnetic interactions are present in the material, this is not the only target of this thesis. Instead, the research undertaken in this thesis is linked towards the synthesis of single-molecule magnets and molecular magnetic refrigerants. While bulk magnetic materials possess domains, which exist in three-dimensional regions, the magnetic properties in single-molecule magnets arise solely from the molecule-based compounds present in the crystal lattice itself.[60] This allows for a deeper understanding of the magnetization dynamics, as well as the potential applications to numerous different fields of research. In this section, a description of single-molecule magnets and some representative examples will be shown.

Single-molecule magnets (SMMs) are zero-dimensional (0-D) compounds that become magnetized upon introduction to an external magnetic field.[61] Similar to SMMs, single-chain magnets (SCMs) are one-dimensional (1-D) chains of repeating units that exhibit superparamagnetic-like properties. Furthermore, SMMs retain their magnetization for a period of time upon removal of the external magnetic field. This property is only present below a certain temperature, called the blocking temperature, T_B. Above this temperature, the compound acts as a paramagnetic compound, with no retention of magnetization. The blocking temperature is not the only important factor for a single-molecule magnet. Also required is the presence of a barrier

to the reversal of magnetization, denoted as *U*. This barrier, also known as the anisotropy barrier, prevents the spin of the molecules from reorienting immediately, giving rise to the retention of the magnetization. The magnetic anisotropy is described as the directional dependence of magnetization in the compound. For a single-molecule magnet, it can be broken down into two terms; the "easy axis" and the "hard plane".[62] In magnetically anisotropic compounds, the magnetization will preferentially align with the "easy axis", perpendicular to the "hard plane". As a result of the presence of magnetic anisotropy, the spin ground state, *S* or *J* (depending on the spin-orbit coupling effect) of a compound becomes bistable, taking values of m_S or m_J, respectively. The presence of a bistable ground state, in conjunction with the magnetic anisotropy, leads to a "double-well" through which the magnetization may predominantly relax (Figure 1.24).[63]

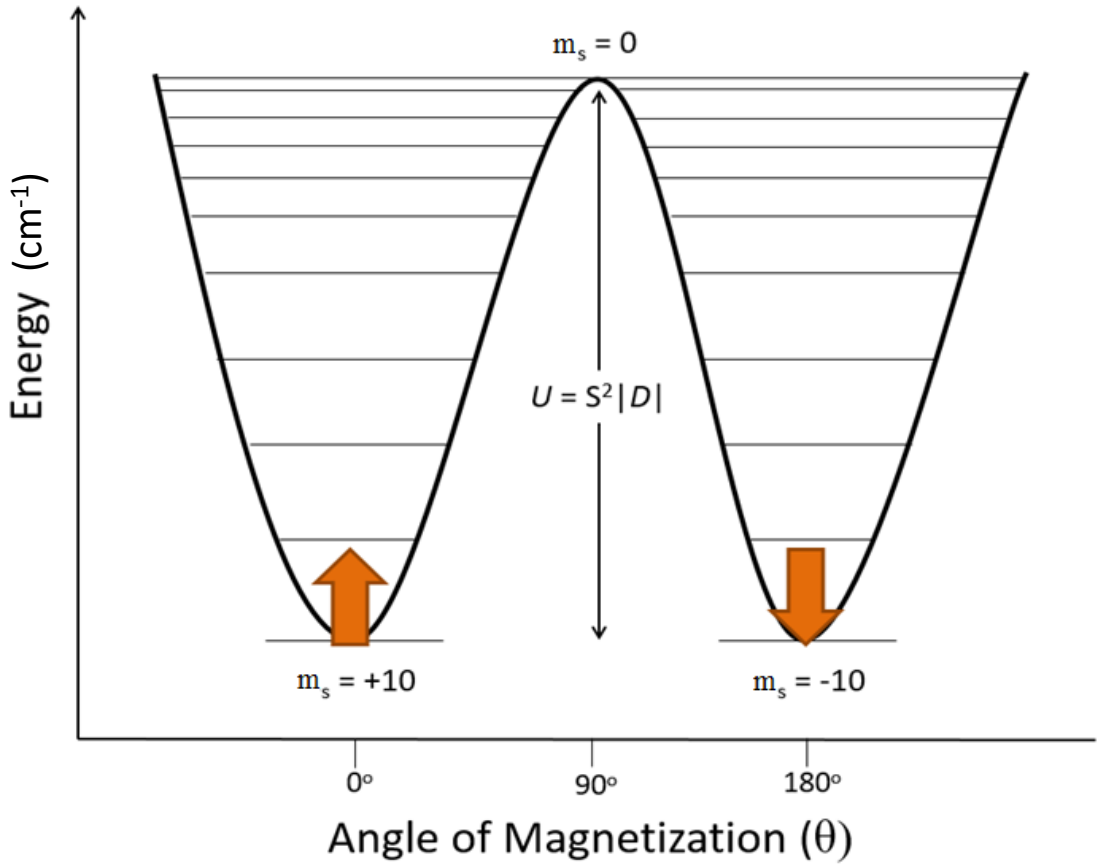

Figure 1.24. A representative example of a "double-well" for a complex with an S = 10 spin ground state. The S = 10 spin ground state is split to the m_S = +10 and m_S = -10 microstates, and the magnetization must relax either over the anisotropy barrier or through the barrier. Reproduced from Ref. 63.

The bistable ground state is separated by the anisotropy barrier U. The magnitude of the barrier, in wavenumbers (cm^{-1}), can be calculated using either Equation 1.14 or Equation 1.15, for integer and half-integer spin systems, respectively.

$$U = |D|S^2 \qquad \textbf{(Eqn. 1.14)}$$

$$U = |D|(S^2 - \frac{1}{4}) \qquad \textbf{(Eqn. 1.15)}$$

In the double-well diagram, each of the individual m_S levels describe a different orientation of the spins in the compound with respect to the anisotropic axis. Upon introduction to an external magnetic field, the spins of the compounds align parallel with the "easy axis", indicated by the upwards arrow in Figure 1.24. Upon removal of the external magnetic field, if the compound is at a temperature lower than T_B, the spins remain trapped at the lowest value of m_S. After a period of time, the magnetization will relax, and the spins of the system will flip to the opposite direction of the anisotropic axis (180^o) to the opposite m_S value. This relaxation process can occur through two different processes; these are the thermally assisted process and the quantum tunneling process.[64] In the thermally assisted process, the magnetization passes through each individual m_S state stepwise over the barrier to the reversal of magnetization, and relax back down to the opposite m_S level. This process is much slower, and therefore the magnetization of the compound is retained for a longer period. However, a competing relaxation process is also present, called the quantum tunneling of magnetization. Quantum tunneling can only occur through degenerate m_S states, but it is a very fast process since it is not governed by the anisotropy barrier. The term 'degenerate m_S states' refers to the m_S microstates with practically the same energy. At low temperatures, if there is the presence of mixing of energetically degenerate m_S states, the magnetization can pass through the barrier as opposed to relaxing over it, and it takes an immediate opposite spin. Since this process is much faster and ignores the anisotropy barrier, the barrier takes on a value much smaller than the expected one of U, leading to an effective anisotropy barrier U_{eff}. It is desirable for quantum tunneling to be non-existent in a single-molecule magnet, or if present, very slow. Quantum tunneling can arise through two different mechanisms. One is the ground state quantum tunneling, which was just previously

described. The second process involves a combination of thermal relaxation and quantum tunneling. The magnetization of the compound relaxes to an exited m_S state through a thermally-assisted process, and then it finds a degenerate excited m_S state which allows it to tunnel through the barrier, and consequently relaxes down to the ground state of opposite spin. This process is called thermally-assisted quantum tunneling, or excited state quantum tunneling. Again, this process leads to a U_{eff} which is smaller than the actual U of the system. A goal in the field of single-molecule magnets is to have the U_{eff} be as large and as close to the U as possible by surpassing the contribution from the quantum tunneling process.

Single-molecule magnets can be identified through two different forms of physical study. The first is through alternating-current (*ac*) magnetic susceptibility studies. While similar to direct-current (*dc*) magnetic susceptibility studies, there is a distinct difference that separates the two. In *dc* magnetic susceptibility studies, a static magnetic field is applied to a sample at a variety of different temperatures. However, in *ac* magnetic susceptibility studies, an oscillating magnetic field of frequency v is applied to the sample. Since the field oscillates, the spins of the compound continually flip to try and keep up with the oscillation of the external magnetic field, leading to a phase shift relative to the external magnetic field.[58] Performed at different frequencies, a profile of the magnetization dynamics can be determined, shown in Figure 1.25.

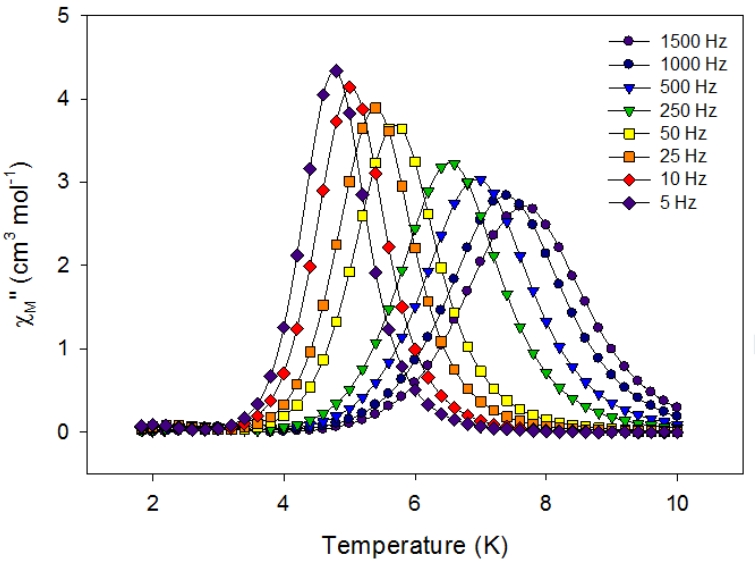

Figure 1.25. A χ_M'' versus *T* plot showing frequency-dependent, out-of-phase signals at different temperatures. Adapted from Ref. 64 with permission from the Royal Society of Chemistry.

The *ac* studies can be divided into two different components; the real component (in-phase), χ', and the imaginary component (out-of-phase), χ''. These components are related to the magnetic susceptibility, χ, through Equations 1.16 and 1.17, respectively.

$$\chi' = \chi cos\varphi \qquad \textbf{(Eqn. 1.16)}$$

$$\chi'' = \chi sin\varphi \qquad \textbf{(Eqn. 1.17)}$$

In the above equations, φ denotes the phase shift relative to the external magnetic field. Using the data found through *ac* magnetic susceptibility studies, an accurate determination of the U_{eff} of the compound can be determined. This is shown in Equation 1.18.[65]

$$\tau = \tau_o e^{(U_{eff}/k_\beta T)} \qquad \textbf{(Eqn. 1.18)}$$

The equation is a variation of the Arrhenius equation, where τ_o is a pre-exponential factor that varies from system to system, and k_β is the Boltzmann constant. From the χ'' versus T plot, if the compound acts as a single-molecule magnet, there will be the presence of frequency-dependent, out-of-phase signals. To determine the relaxation time at a given temperature, the following equation is used (Equation 1.19).

$$\frac{1}{\tau} = 2\pi\nu \qquad \textbf{(Eqn. 1.19)}$$

In the above equation, the relaxation time is defined by τ and the frequency of the oscillating external magnetic field is defined by ν. The temperature for a given relaxation time is determined by finding the temperature at which the peak maximum of a χ'' curve is observed. This gives rise to a series of different relaxation times, τ, for different temperatures, T. With this data, a plot of the $\ln(\tau)$ (or $\ln(1/\tau)$) versus $1/T$ can be formed, and the U_{eff} can be determined using Equation 1.20.[65]

$$\ln \tau = \ln \tau_o + \frac{U_{\text{eff}}}{k_\beta T} \qquad \textbf{(Eqn. 1.20)}$$

An example of the plots needed for the determination of the barrier of magnetization reversal can be seen in Figure 1.26.[64] Knowing the U_{eff} is essential in the determination of the quality of a single-molecule magnet, and it is the most common parameter used to describe the single-molecule magnetism behaviour of a paramagnetic compound.

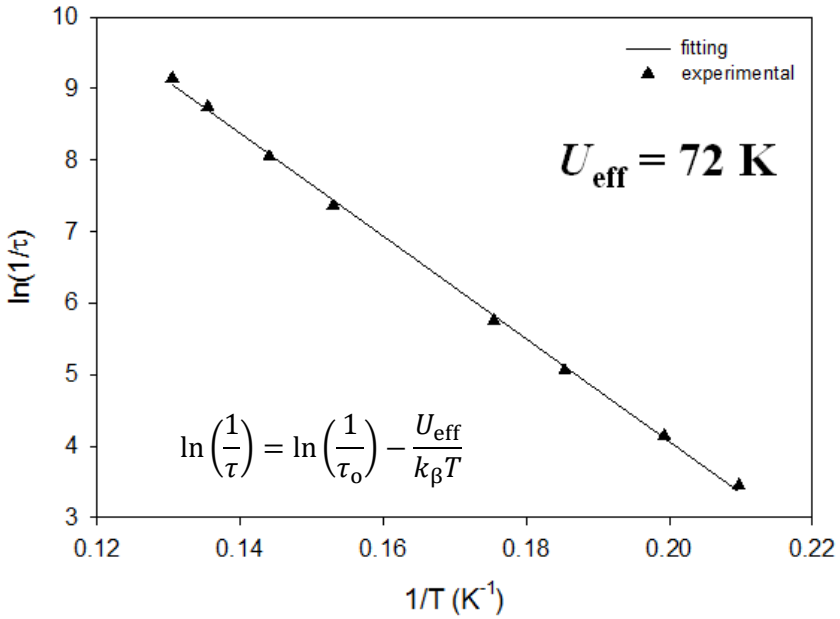

Figure 1.26. An example of the Arrhenius-type plot for the representative {Mn_{12}} complex (discussed later). The plot relates the relaxation time at different temperatures to the U_{eff} of the molecule. Adapted from Ref. 64 with permission from the Royal Society of Chemistry.

However, a χ'' versus T plot is only the first indicator that a compound may be a single-molecule magnet. The final determination of whether or not a compound is a single-molecule magnet is through the presence of magnetic hysteresis in a magnetization versus field plot (M versus H). To check for hysteresis, an external *dc* magnetic field is applied to a single-crystal of the compound. The external magnetic field is increased from 0 to large field values of $+H$, normally to a maximum of 7 T. Similar to the previous M versus H plot described in Section 1.4, the higher fields are used to try and saturate the magnetization, so that all the spins of the compound align parallel with the external magnetic field, $+H$. If saturation is achieved, it is seen as a plateau in the magnetization. Saturation may not be achieved if two different cases arise: a)

there is the presence of low-lying excited states with energies close to the energy of the ground state, in which case, the compound will most likely not function as an efficient single-molecule magnet; and b) there is the presence of magnetic anisotropy, which is one of the prerequisites for a single-molecule magnet.[66] To determine which case is true, the direction of the external *dc* field is then reversed to the -*H* direction. If the magnetization passes through 0 and saturates in the opposite direction, then no loop is observed and magnetic hysteresis is absent; the compound is not a single-molecule magnet. However, upon reaching zero external *dc* field (over the process of +*H* to -*H*), if the value of the magnetization is non-zero, there is some magnetization remaining in the compound in the absence of an external *dc* field. This is called the remnant magnetization. Furthermore, if the direction of the external *dc* field is changed again, from -*H* to +*H*, there is a point where the magnetization of the compound is zero in the presence of the external *dc* field. This is called the coercive field, and it is the value of external *dc* field that the compound can withstand before losing its magnetization.[67] With the presence of remnant magnetization and a coercive field, a hysteresis loop is generated. Magnetic hysteresis loops are exhibited by all bulk magnets, and are also seen in single-molecule magnets. It is this plot that determines if the compound can act as a single-molecule magnet. An example of magnetic hysteresis can be seen in Figure 1.27.[64] In the plot shown below, *M* versus *H* studies were performed at a variety of different temperatures. This type of plot can elucidate T_B for a given SMM, where the T_B is described as the first temperature where a hysteresis loop opens up in *M* versus *H* studies.[64]

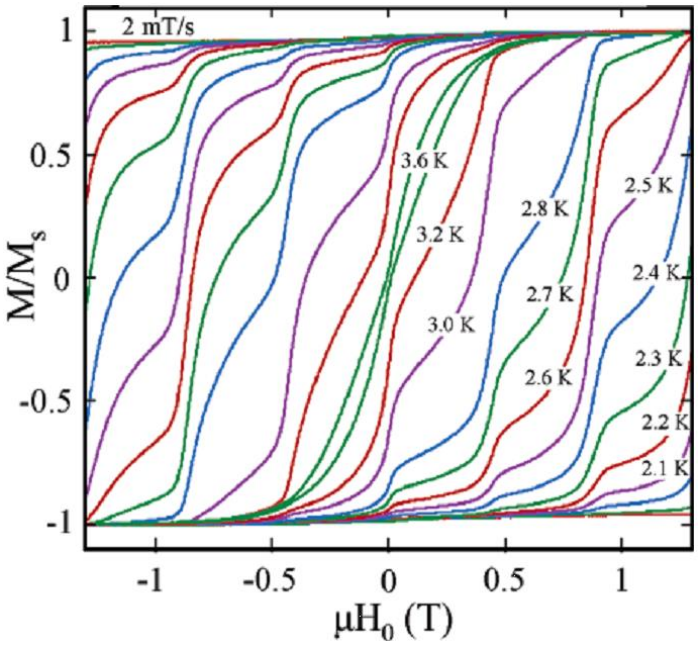

Figure 1.27. An example of the magnetic hysteresis loops produced at different temperatures from the {Mn_{12}} SMM (*vide infra*). Adapted from Ref. 64 with permission from the Royal Society of Chemistry.

In the above figure it can be seen that the hysteresis loops are not smooth curves, as seen in all bulk magnets, but rather have "steps", sudden drops in the magnetization at certain field values.[68] These are indicative of quantum tunneling processes for the relaxation of magnetization. However, there are methods for suppressing quantum tunneling of magnetization. If the *ac* magnetic susceptibility studies are performed in the presence of a small external *dc* field, the mixing of the degenerate m_S states is reduced. This forces the magnetization to relax over the anisotropy barrier rather than tunnel through the barrier; such compounds are called "field-induced" single-molecule magnets, due to their reliance on the external *dc* field.[69]

The first SMM discovered is the well-known, deeply studied {Mn_{12}}, reported by Gatteschi, Christou, Hendrickson, and coworkers.[70] Also known as Mn_{12}-acetate, the structure of the compound can be seen in Figure 1.28. The complete formula of the compound is $[Mn^{III}_8Mn^{IV}_4O_{12}(O_2CMe)_{16}(H_2O)_4]$, and can be described as a central cubane structure of four Mn^{IV} metal ions surrounded by eight Mn^{III} metal ions. Bridging ligation in the complex is provided by both oxide and carboxylate groups from μ_4-O^{2-} and μ-acetate molecules, respectively. The ring of Mn^{III} is nonplanar, and all of the Jahn-Teller axes of Mn^{III} ions align in the same direction. This gives rise to a large and negative axial (or 'easy axis'-type) anisotropy (D = -0.5 cm^{-1}). The compound was found to have a spin ground state of S = 10. This was rationalized by the antiferromagnetic coupling between the outer Mn^{III} ring and the inner Mn^{IV} cubane, while each individual metal ion in the separate units is ferromagnetically-coupled with each other (8 Mn^{III}, S = 16; 4 Mn^{IV}, S = 6). The {Mn_{12}} compound was found to have a U_{eff} = 51 cm^{-1} or 73 K, and a T_B = 3 K, which was the record for a long period of time in the field of 3*d*-metal based single-molecule magnets.

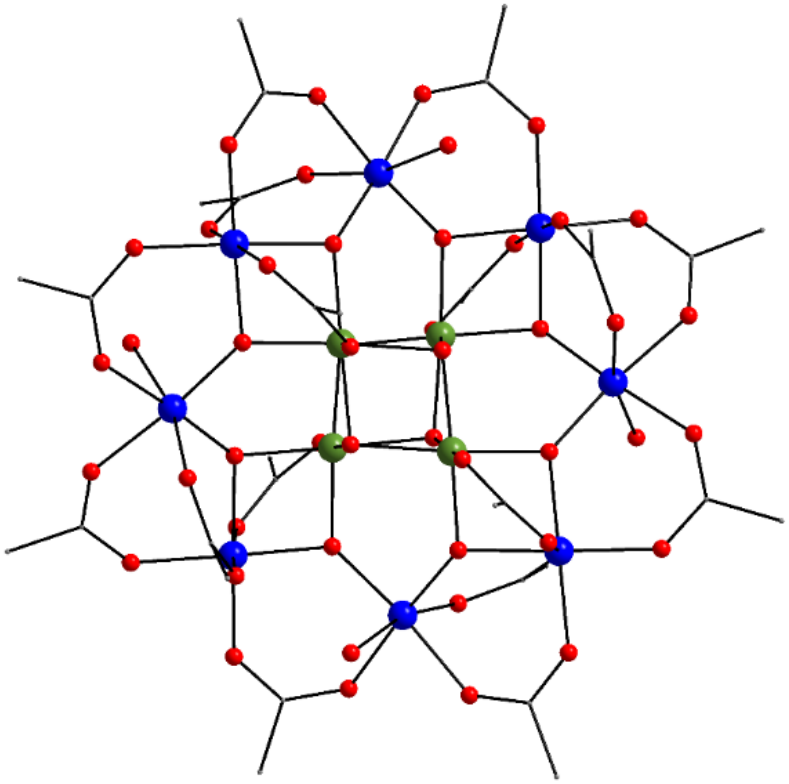

Figure 1.28. Structure of the Mn_{12}-acetate, reported by Gatteschi, Christou, Hendrickson, and coworkers. H atoms are omitted for clarity. Colour scheme: Mn^{IV}, olive green; Mn^{III}, blue; O, red; C, grey. Reproduced from Ref. 70.

For many years, synthetic chemists thought that the primary way to improve upon the U_{eff} of single-molecule magnets was by increasing the spin ground state values, S, to higher and higher values, based on Equation 1.13. This led chemists to try and tailor complexes with ferromagnetic exchange interactions, giving rise to large spin ground state values. Indeed, in 2006, Powell and coworkers reported a $\{Mn_{19}\}$ polynuclear metal complex with the record spin ground state to date of $S = 83/2$ (Figure 1.29).[71] It was expected that with such an enormous spin ground state, the U_{eff} would therefore be very large. However, no single-molecule magnetism behaviour was

observed. It was found that the geometrical arrangement and strong ferromagnetic interactions between the spin carriers lead to a structure that had low anisotropy, even though the Mn^{III} ions showed a high degree of Jahn-Teller distortion.

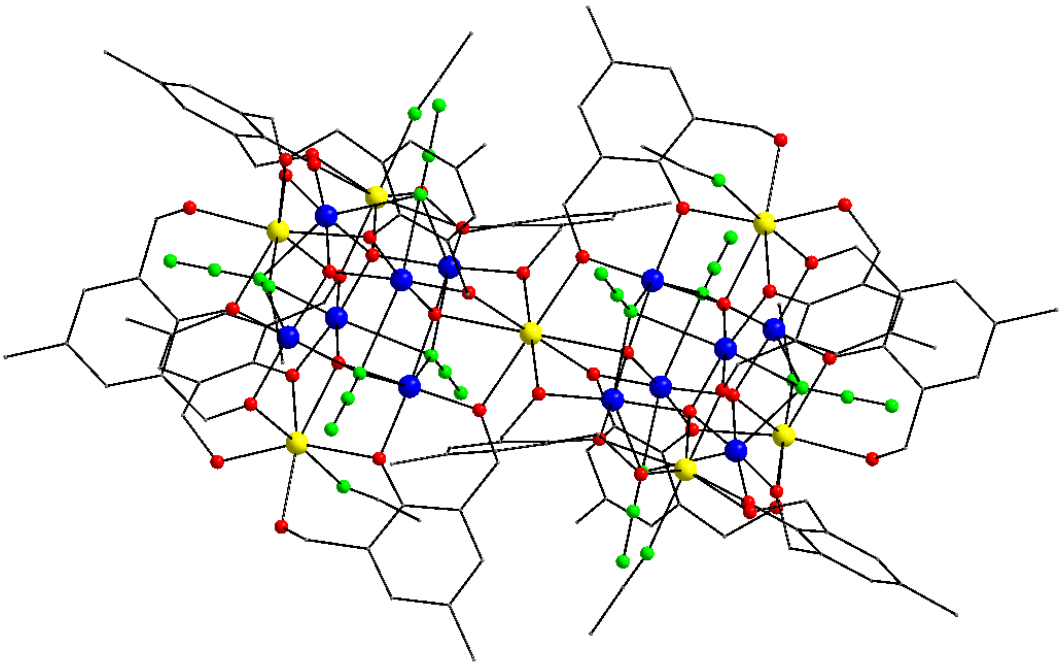

Figure 1.29. Structure of the $\{Mn_{19}\}$ reported by Powell and coworkers, which has the record highest spin of any polynuclear metal complex with S = 83/2. H atoms are omitted for clarity. Colour scheme: Mn^{III}, blue; Mn^{II}, yellow; O, red; N, green; C, grey. Reproduced from Ref. 71.

Due to this discovery, synthetic chemists decided to start focusing more on enhancing the magnetic anisotropy of complexes, rather than increasing the spin. This naturally led scientists to start studying highly anisotropic metal ions, that is, 4*f*- and 5*f*-metal ions (lanthanides and actinides, respectively). In 2003, Ishikawa and coworkers reported a family of complexes with the formula $[Pc_2Ln]^-$, where Pc^{2-} is phthalocyanine and Ln^{III} = Tb^{III}, Dy^{III}, Ho^{III}, Er^{III}, Tm^{III} and

Yb^{III} (Figure 1.30).[7] The compound consists of a single Ln^{III} ion sandwiched between two double-deprotonated phthalocyanine ligands, and the Tb^{III} and Dy^{III} analogues exhibited slow relaxation of magnetization. The $[Pc_2Tb]^-$ analogue possessed U_{eff} values as large as 584 cm^{-1}, depending on the conditions of the reaction.

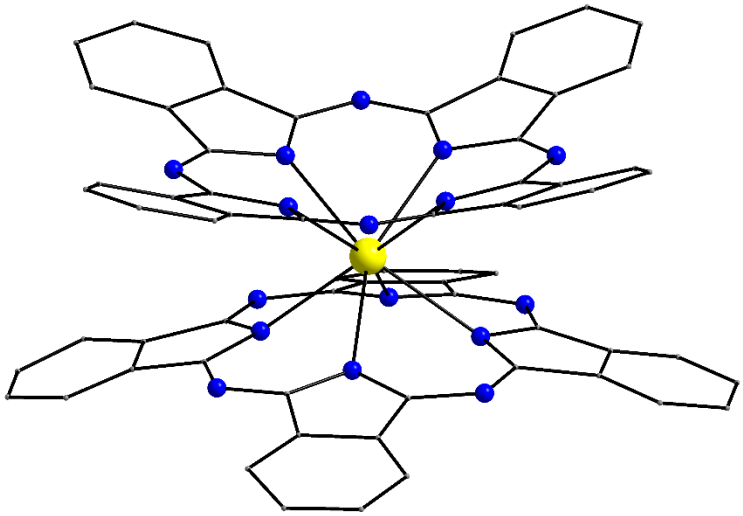

Figure 1.30. Structure of $[Pc_2Ln]^-$, reported by Ishikawa and coworkers (Ln^{III} = Tb^{III}, Dy^{III}, Ho^{III}, Er^{III}, Tm^{III} and Yb^{III}). H atoms are omitted for clarity. Colour scheme: Ln^{III}, yellow; N, blue; C, grey. Reproduced from Ref. 7.

The single-molecule magnetism behaviour of the $[Pc_2Ln]^-$ compounds was further explored by Rinehart and Long in 2011.[72] It was found that the spin-orbit coupling of the lanthanide ion gave rise to the large single-ion anisotropy, and that the interaction of the ligand field with the shape of the lanthanide's electron density enhances this interaction and consequently the overall magnetic anisotropy (Figure 1.31). For example, Tb^{III} ion, with an electronic configuration of $[Xe]4f^8$, possesses an oblate electron distribution. To enhance the intrinsic magnetic anisotropy

of the Tb^{III} ion, the optimal ligand field is one where the ligands are present above and below the *xy* plane, in a sandwich-like motif. This explains the large U_{eff} of the $[Pc_2Tb]^-$, where the ligands are in the correct orientation to enhance the intrinsic anisotropy of the oblate Tb^{III} metal ion.

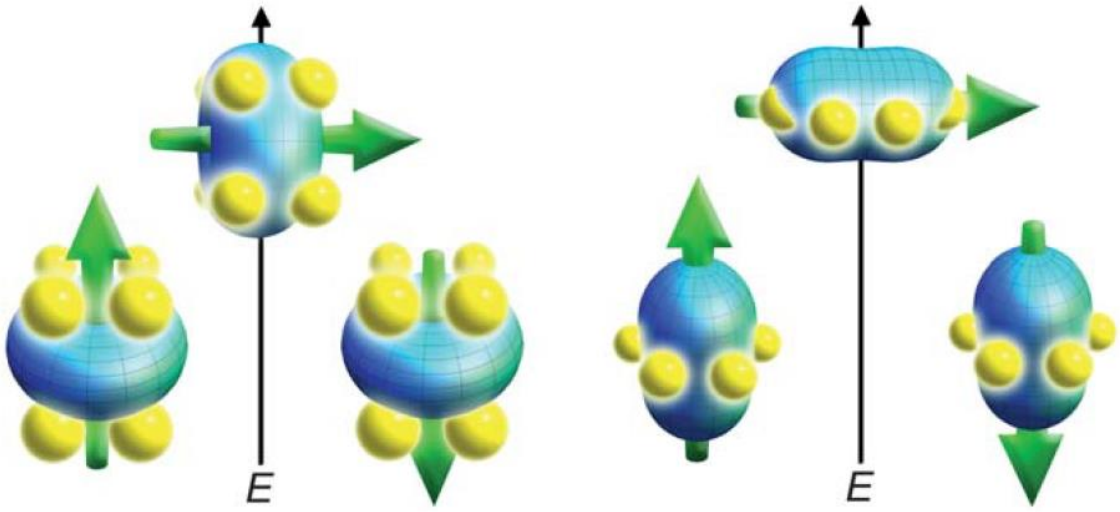

Figure 1.31. Depictions of the combination of the ligand field (yellow spheres) with the electron distribution (blue ovoid) of an oblate (left) or a prolate (right) Ln^{III} metal ion. Oblate lanthanides prefer axial "sandwich"-type ligand fields, while prolate lanthanides prefer equatorial ligand fields. Adapted from Ref. 72 with permission from the Royal Society of Chemistry.

However, there is a downside to solely employing 4*f*-metal ions towards the synthesis of single-molecule magnets. Recall that the spin is still tied to the determination of the U_{eff}, so the spin ground state of the molecule is still important. The spin ground state is a result of the magnetic exchange interactions of the spin carriers in a molecule. However, in homometallic 4*f*-metal cluster chemistry, the interactions between lanthanide metal ions are very weak and basically unaffected by the ligands bound to them - and therefore crystal field splitting

parameters are weak. This is due to the efficient shielding of the 4*f* electrons by the filled 5*s* and 5*p* orbitals.[73] Furthermore, a phenomenon called lanthanide contraction also has an effect. The 4*f* orbitals of a lanthanide poorly shield outer electrons from the nuclear charge, and consequently the outermost electrons experience a stronger pull towards the nucleus, reducing the atomic radius and consequently the ionic radius of the lanthanide. Therefore, lanthanide metal ions do not interact through a superexchange mechanism as seen in 3*d*-metal ions, but through a dipole interaction.[74] Consequently, the interactions between lanthanides are commonly weak and antiferromagnetic in nature. To address this challenge, scientists decided to combine 3*d*- and 4*f*-metal ions together to form polynuclear heterometallic 3*d*/4*f*-metal complexes. The goal behind this combination was to gain access to the large spin ground state values provided by the interactions of 3*d*-metal ions with each other and 4*f*-metal ions, as well as access to the large single-ion anisotropy of the 4*f*-metal ions arising from the ligand field and the electron distribution of the lanthanide. A representative example of a dinuclear heterometallic 3*d*/4*f* single-molecule magnet is shown in Figure 1.32.[75]

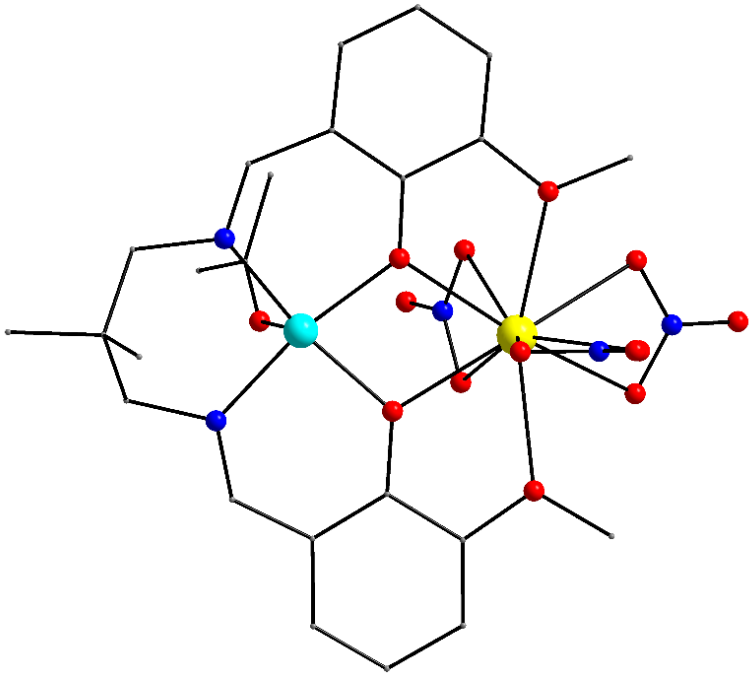

Figure 1.32. Structure of the {CuLn} complex reported by Nojiri and coworkers (Ln^{III} = Gd^{III}, Tb^{III}, Dy^{III}, Ho^{III} and Er^{III}). H atoms are omitted for clarity. Colour scheme: Ln^{III}, yellow; Cu^{II}, cyan; O, red; N, blue; C, grey. Reproduced from Ref. 75.

This compound, reported by Nojiri and coworkers, consists of a five-coordinate Cu^{II} with a square pyramidal coordination geometry and a ten-coordinate Ln^{III} ion, where Ln^{III} is Gd^{III}, Tb^{III}, Dy^{III}, Ho^{III} and Er^{III}. The overall formula of a representative example of this family of complexes is $[CuLn(L)(C_3H_6O)(NO_3)_3]$, where H_2L is *N*,*N*′-bis(3-methoxysalicylidene)-1,3-diamino-2,2-dimethylpropane. The double-deprotonated ligand L^{2-} acts as a tetradentate chelating ligand to the Cu^{II} metal ion, forming three 6-membered chelate rings. The remaining coordination site on the Cu^{II} ion is occupied by a terminally-bound acetone molecule. L^{2-} further bridges the Cu^{II} metal ion with the Ln^{III} metal ion through two alkoxido bridges, and further acts as a tetradentate chelating ligand to the Ln^{III} as well, forming two 5-membered chelate rings. *Dc* magnetic

susceptibility studies showed a decrease of the $\chi_M T$ product at low temperatures, attributed to the depopulation of the Stark (m_J) sublevels, the presence of single-ion Ln^{III} anisotropy (except from Gd^{III}), as well as potential intra- and intermolecular antiferromagnetic exchange interactions. However, even with a decrease of the $\chi_M T$ product, the {CuTb} and the {CuDy} analogues were found to act as single-molecule magnets, with the {CuTb} analogue possessing the largest Cu^{II}/Ln^{III} U_{eff} to date (U_{eff} = 29.4 cm^{-1}).[75]

The field of single-molecule magnetism is still an active area of research for many scientists, from synthetic chemists to theoretical physicists. However, polynuclear metal complexes containing anisotropic metal ions are only part of the story when it comes to probing the magnetic properties of these compounds. Upon changing anisotropic metal ions to isotropic ones, the physical properties and consequently the magnetic properties change. This led scientists to begin studying polynuclear metal complexes as potential molecular magnetic refrigerants.

1.7. Magnetocaloric Effect and Molecular Magnetic Refrigerants

In addition to the property of single-molecule magnetism, polynuclear metal complexes can exhibit a property called the magnetocaloric effect (MCE). This effect, in the simplest terms, is a temperature change in the complex that is caused by the introduction or removal of an external magnetic field. Complexes that exhibit this effect are of great importance in not only understanding the physical changes that can occur in the presence of an external magnetic field, but also with respect to many different areas of research. Molecular magnetic refrigerants that can cool complexes to cryogenic temperatures could find applications in a wide variety of fields

such as medicine and industrial research.[76] The primary reason for researching molecular magnetic refrigerants is one of the utmost importance; the rising cost of ^{3}He. The rising cost of this rare isotope, which is used in cryogenic cooling processes, coupled with the scarcity of this isotope, has enhanced the desire for alternative techniques for cooling at cryogenic temperatures. Cryogenic cooling can be achieved through the use of lanthanide containing alloys like $Gd_3Ga_5O_{12}$ (gadolinium gallium garnet, GGG),[77] but research is continually ongoing to see if discrete molecules could act as similarly efficient refrigerants.

The magnetocaloric effect is linked to two different properties, both of equal importance to characterizing this effect; the isothermal change in magnetic entropy (ΔS_m) and the adiabatic temperature change (ΔT_{ad}). These processes are outlined in Figure 1.33.[78]

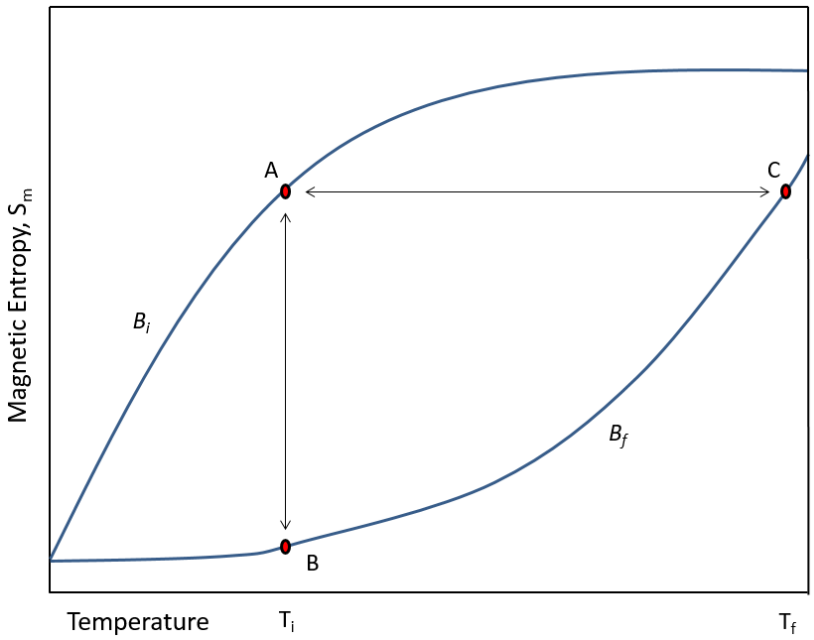

Figure 1.33. A plot of the magnetic entropy versus temperature (S_m versus T) at initial and final external magnetic fields (B_i and B_f, respectively). The points A, B, and C on the plot describe different thermodynamic processes that affect the temperature (A → C) and the magnetic entropy (A → B), respectively. Reproduced from Ref. 78.

Points A, B, and C on the chart correspond to different temperatures and magnetic entropies at different external magnetic field strengths. Process A → C describes an adiabatic magnetization/demagnetization process. In this process, the total entropy of the system remains constant while the temperature changes with changing magnetic field. Process A → B describes an isothermal magnetization/demagnetization process. In this process, the temperature remains constant (through the use of an external stimulus), and thus the magnetic entropy of the system changes.

Also important to note for molecular magnetic refrigerants is the total entropy of the system. The total entropy of a magnetic refrigerant consists of three terms; the magnetic entropy (S_m), the lattice entropy (S_r), and the electronic entropy (S_e). The magnetic entropy is a function of field (B) and temperature (T), while the lattice entropy and the electronic entropy are only functions of temperature. The relationship of these functions is shown in Equation 1.21.[79]

$$S_{\text{total}} = S_{\text{m}}(B,T) + S_{\text{r}}(T) + S_{\text{e}}(T) \qquad \textbf{(Eqn. 1.21)}$$

This equation explains the plot shown in Figure 1.33. In process A → C, the total entropy of the system does not change. However, since the spins of the electrons in the paramagnetic material have aligned parallel to the external magnetic field, the magnetic entropy of the system decreases. Consequently, there is an equal and opposite increase in the lattice and electronic entropies. Since these entropies are functions of temperature, the overall temperature of the material increases. Upon removal of the external magnetic field, the spins of the electrons in the system re-randomize, increasing the magnetic entropy with a concomitant decrease in the lattice and electronic entropies. In process A → B, the temperature of the system is kept constant through the use of an external source. Since the temperature is kept constant upon introduction to

an external magnetic field, the lattice and electronic entropies remain constant. However, the magnetic entropy decreases as the spins align parallel with the field, resulting in a net decrease of the total entropy of the system. Upon removal of the external magnetic field, the spins again re-randomize and the lattice and electronic entropies again experience a decrease. However, since the temperature was kept constant in this process, the reduction of these entropy terms leads to a temperature that is colder than the initial, constant temperature; the paramagnetic material acts as a refrigerant that takes on a load of heat from the surrounding environment.

The general steps involved in using a molecular magnetic refrigerant can be described as a Carnot cycle, as shown in Figure 1.34.[80] The Carnot cycle can be described as a series of sequential adiabatic and isothermal magnetizations, followed by an adiabatic and isothermal demagnetization. Two important equations arise from this cycle, as outlined in Equations 1.22 and 1.23.

$$\Delta T_{\mathrm{ad}} = T_{\mathrm{hot}} - T_{\mathrm{cold}} \qquad \textbf{(Eqn. 1.22)}$$

$$Q_{\mathrm{c}} = T_{\mathrm{cold}} \Delta S_{\mathrm{cold}} \qquad \textbf{(Eqn. 1.23)}$$

ΔT_{ad} describes the adiabatic temperature change when the entropy of the system remains constant.[80] This term consists of two variables; T_{hot} and T_{cold}. T_{hot} describes the temperature that must be reached through the use of an external refrigerant; the larger this temperature, the wider the range of temperatures the molecular magnetic refrigerant can cool. Furthermore, it allows for the use of milder external refrigeration techniques (e.g. liquid N_2 versus liquid ^{3}He). T_{cold} describes the temperature to which the molecular magnetic refrigerant can reach; for cryogenic applications, the goal is to reach the sub-Kelvin region. In the second equation, Q_{c}, describes the heat that is absorbed by the magnetic refrigerant through the isothermal demagnetization step.[80]

In addition to T_{cold}, this value is dependent upon ΔS_{cold}, which is the change in magnetic entropy at the temperature T_{cold}.

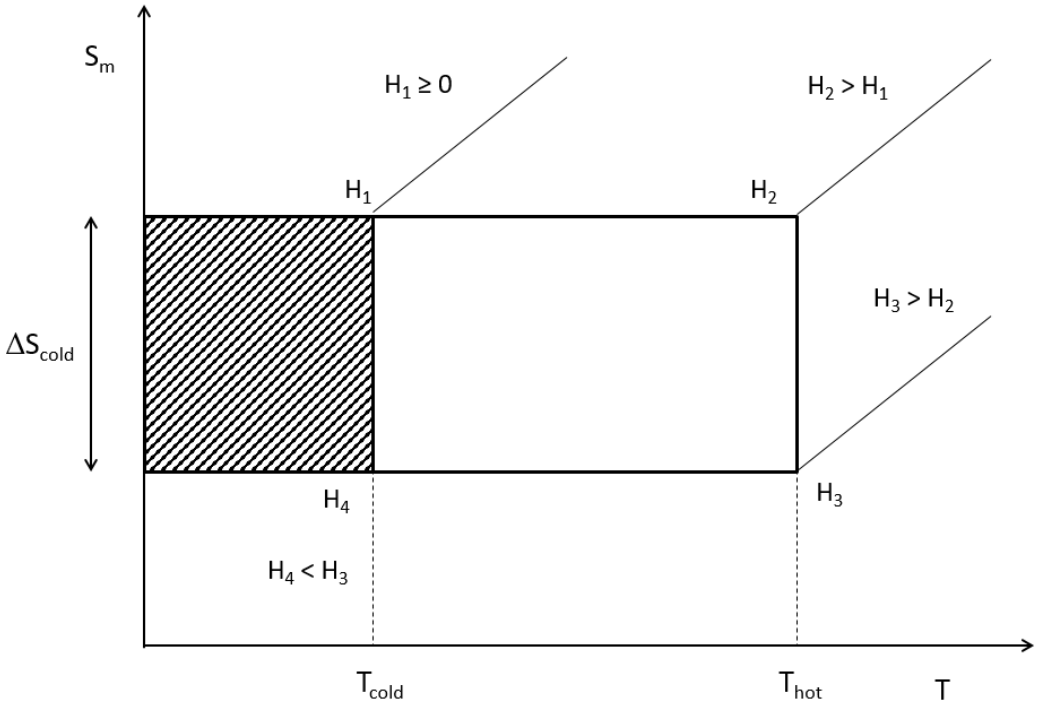

Figure 1.34. An example of a Carnot cycle; from $H_1 \rightarrow H_2$ and $H_2 \rightarrow H_3$, there is an adiabatic and isothermal magnetization taking place, respectively. From $H_3 \rightarrow H_4$ and $H_4 \rightarrow H_1$, there is an adiabatic and isothermal demagnetization taking place, respectively. Reproduced from Ref. 80.

The synthesis of molecular magnetic refrigerants is as well thought out as the synthesis for any single-molecule magnet, and much like single-molecule magnets, have specific properties that are targeted for enhancement of the MCE. These are: a) a large metal-to-ligand ratio (low overall molecular mass); b) moderate to weak ferromagnetic exchange interactions, leading to a large spin ground state value of *S*; and c) negligible magnetic anisotropy.[81] The large metal-to-ligand ratio, also described as a large magnetic-to-nonmagnetic ratio, is important for two

reasons, one of which is practical and the other of which is a matter of context. The practical aspect arises from the fact that when the molecule takes on a load of heat from the surrounding environment, the molecule itself must first reach the refrigeration temperature (T_{cold}) before it can effectively cool its surroundings. The matter of context arises when talking about what units to use for the molecular magnetic refrigerant. The common units for ΔS_m are J mol^{-1} K^{-1} (in terms of the ideal gas constant, *R*), J kg^{-1} K^{-1} (mass, accounting for the molar mass of the molecule), and mJ cm^{-3} K^{-1} (volumetric, accounts for the density of the material). In this thesis, values of ΔS_m will be described in units of J kg^{-1} K^{-1}. Secondly, it is desirable to have moderate to weak ferromagnetic exchange interactions between the metal ions in a molecular magnetic refrigerant. Ferromagnetic interactions lead to an increase in the spin ground state of the molecule, *S*, and are related to the magnetic entropy through the Equation 1.24.[81]

$$S_m = Rln(2S + 1) \quad \textbf{(Eqn. 1.24)}$$

However, this equation describes a molecular magnetic refrigerant in which all of the metal ions remain magnetically coupled at all values of external magnetic field. If the coupling between the metal ions is sufficiently weak, the external magnetic field could overcome the coupling of the metal ions, and allow them to act as their own individual spin carriers. This gives rise to the Equation 1.25.[81]

$$S_m = nRln(2S + 1) \quad \textbf{(Eqn. 1.25)}$$

In the above equation, *n* describes the number of a given paramagnetic metal ion in the compound, while *S* is the spin-only value of the paramagnetic metal ion. The largest possible values of ΔS_m arise from weakly coupled systems where the external magnetic field can overcome the coupling of the metal ions. Furthermore, the weaker the coupling of the metal ions,

the smaller the external field needed to force the metal ions to act as their individual spin carriers. This increases the probability for the molecular magnetic refrigerant to be used for more commercial applications, as opposed to solely in fields of fundamental research and cryogenics. Thirdly, the molecular magnetic refrigerant should have negligible magnetic anisotropy. Magnetic anisotropy serves to remove the degeneracy of m_s or m_J microstates of the molecule.[82] While having a well isolated spin ground state is desirable for an efficient single-molecule magnet, in a molecular magnetic refrigerant, it is preferable to have all of the m_s or m_J states degenerate to increase the degrees of freedom (i.e. the entropy) present at the spin ground state. Furthermore, recall that magnetic anisotropy describes the directional dependence of the magnetization. If the magnetic anisotropy is large, the polarization of the spins in the molecule are less sensitive to the external magnetic field, since the magnetization will prefer to align with the anisotropic ("easy") axis. Therefore, to align all of the spins parallel to the magnetic field, larger external magnetic fields would be needed, thus decreasing the efficiency of the MCE in the molecule.

Knowing the required parameters to target for the synthesis of molecular magnetic refrigerants, synthetic chemists look towards isotropic metal ions as their primary tool for synthesis. The most common metal ion used is Gd^{III}, a lanthanide ion with an electronic configuration of [Xe]4f^7. Gd^{III} has small intrinsic anisotropy, and possesses a large *S* value of 7/2, arising from the seven unpaired electrons present in its orbitals.[83] Furthermore, the *f* orbitals of gadolinium are efficiently shielded by the larger 5*s* and 5*p* orbitals, due to a phenomenon called lanthanide contraction. This weakens the strength of the interactions between adjacent Gd^{III} ions, and changes the nature of the interaction from a coupling interaction to an interaction of dipoles. The latter interactions are weak are much easier to overcome using an external

magnetic field. However, Gd^{III} is not the only metal ion used in the study of molecule magnetic refrigerants. Isotropic transition metal ions are also used, such as Mn^{II} and Cu^{II}, moving the focus from homometallic 4*f*-metal cluster chemistry to heterometallic 3*d*/4*f*-metal cluster chemistry. In particular, Cu^{II} is an interesting choice because of its ability to overcome the shielding over the 4*f* orbitals of Gd^{III} and consequently exhibit ferromagnetic exchange interactions between the two metal ions, as seen in Figure 1.35.[84]

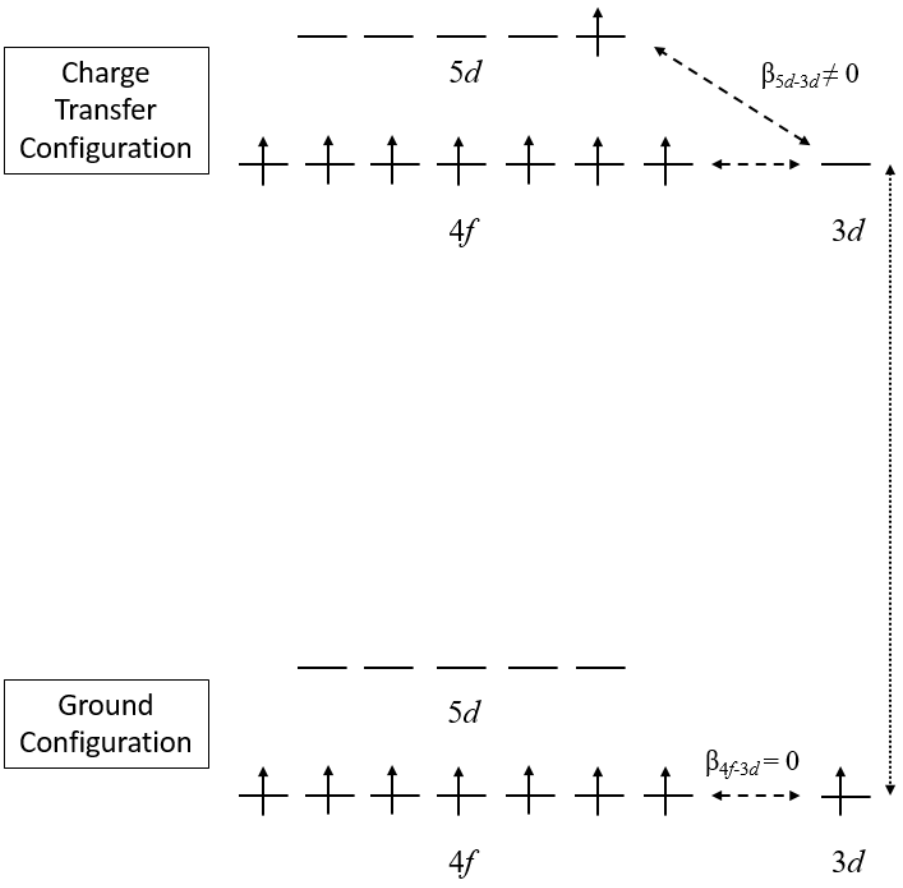

Figure 1.35. Diagram depicting the interaction between Cu^{II} and Gd^{III}. The term "β" is a transfer integral, describing whether or not electron transfer and therefore an interaction could occur. Reproduced from Ref. 84.

In the ground state configuration, the lone unpaired electron in the 3*d* orbital of Cu^{II} cannot effectively interact with the electrons of the 4*f* orbitals, as indicated by the exchange integral ($\beta_{4f\text{-}3d} = 0$). However, due to the size of the Gd^{III}, the 5*d* orbitals have been calculated to be very diffuse, and exist a long distance away from the nucleus of the Gd^{III}.[84] In fact, these orbitals are so diffuse such that they approach the 3*d* orbitals of the Cu^{II} ion when the two metals are bridged through an O donor atom. This gives the opportunity for the lone unpaired electron of the Cu^{II} to be transferred to the 5*d* orbital of the Gd^{III} from its 3*d* orbital. This charge transfer has a non-zero exchange integral ($\beta_{5d\text{-}3d} \neq 0$), and thus can rationalize the commonly seen ferromagnetic interactions between Cu^{II} and Gd^{III} ions. Consequently, this makes a heterometallic 3*d*/4*f* approach towards the synthesis of molecular magnetic refrigerants as attractive, if not more so than homometallic 4*f*-metal cluster chemistry. The 3*d*/4*f* approach allows for the combination of Cu^{II} and Gd^{III}, leading to ferromagnetic interactions and consequently large spin ground state values, *S*. This interaction can be further enhanced by the nature of the bonds between the Cu^{II} and the Gd^{III} ions. When bridged through O donor atoms, the average Cu^{II}–O–Gd^{III} angles and the average Cu^{II}–O–Gd^{III}–O torsion angles have a distinct effect on the magnitude and the sign of the *J* coupling constant between the two spin carriers.[85] Torsion angles close to 0° (planarity) and bond angles of ~96°–102° have been correlated to positive values of *J*, indicating ferromagnetic exchange interactions between the Cu^{II} and Gd^{III} ions in a given polynuclear metal cluster.

There have been many different examples of molecular magnetic refrigerants reported in the literature, ranging from discrete molecules to 2-D coordination polymers and 3-D metal-organic frameworks. Currently, the record holder for the largest $-\Delta S_m$ is a Mn^{II} monomer reported by Tong and coworkers (Figure 1.36).[86] The monomer consists of two chelating glycolate ligands,

with the remaining two coordination sites being occupied by water molecules. This compound, formed by the hydration of the $[Mn(gly)_2]_n$ polymer, possesses a $-\Delta S_m$ of 60.3 J kg^{-1} K^{-1} at a ΔB_o = 7 T, the largest of any molecular magnetic refrigerant to date.

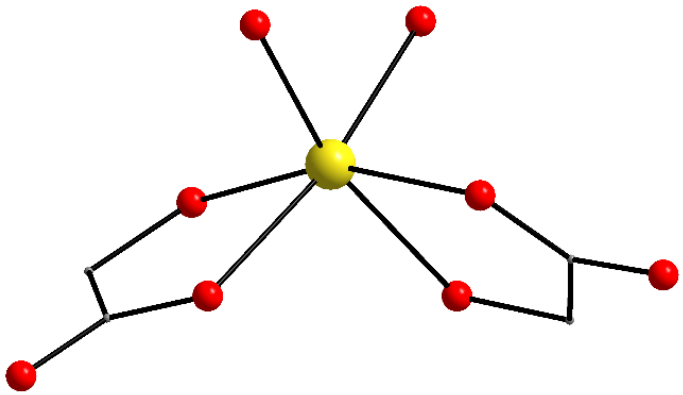

Figure 1.36. Structure of $[Mn(gly)_2(H_2O)_2]$ reported by Tong and coworkers. This complex holds the record value of $-\Delta S_m$ for all molecular magnetic refrigerants. H atoms are omitted for clarity. Colour scheme: Mn^{II}, yellow; O, red; C, grey. Reproduced from Ref. 86.

However, there are also many good examples of heterometallic 3*d*/4*f*-metal clusters that can act as molecular magnetic refrigerants, particularly ones that make use of Cu^{II} and Gd^{III} ions for the reasons detailed above. The record holder for a discrete Cu^{II}/Gd^{III} molecule is a $\{Cu_5Gd_4\}$ cluster, reported by Brechin, Evangelisti, Murray, and coworkers in 2011 (Figure 1.37).[87] The compound was synthesized using serendipitous assembly, combining $Cu(NO_3)_2{\cdot}3H_2O$, $Gd(NO_3)_3{\cdot}6H_2O$, triethanolamine, pivalic acid, and Et_3N, in solvent MeOH. The resulting solution was layered over Et_2O and yielded blue crystals. The compound was subsequently characterized using *dc* magnetic susceptibility studies, and was found to exhibit ferromagnetic exchange interactions between the metal ions. The spin ground state was determined to be *S* =

31/2 according to magnetization versus field studies, which is not the maximum possible spin ground state of 33/2 for a system comprising 5 Cu^{II} and 4 Gd^{III} ions ferromagnetically-coupled to each other. This was attributed to the central Cu^{II} ion of the structure as being antiferromagnetically-coupled with the remaining metal ions. Magnetothermal studies were performed as well, experimentally determining a $-\Delta S_m$ of approximately 31 J kg^{-1} K^{-1} at ΔB_o = 9 T. This value is currently the largest $-\Delta S_m$ of any Cu^{II}/Gd^{III} discrete molecule to date.

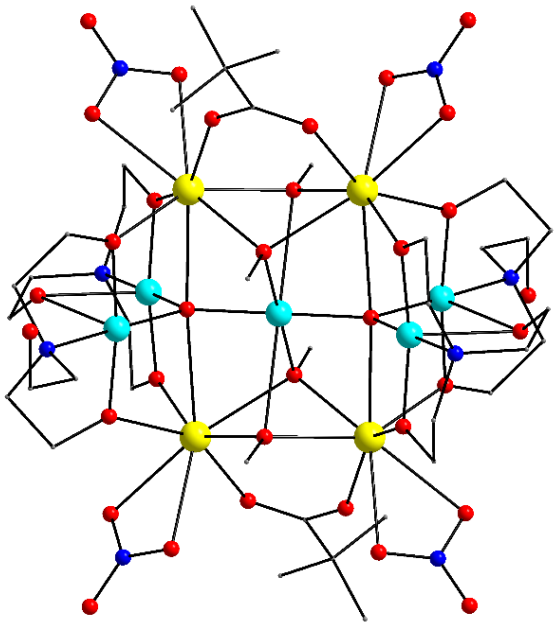

Figure 1.37. Structure of the $\{Cu_5Gd_4\}$ cluster, reported by Brechin, Evangelisti, Murray, and coworkers. This complex holds the record $-\Delta S_m$ for all discrete Cu^{II}/Gd^{III} molecular magnetic refrigerants. Its structure can be described as a "bow-tie" of Cu^{II} ions sandwiched on top and bottom by two Gd^{III} metal ions. H atoms are omitted for clarity. Colour scheme: Gd^{III}, yellow; Cu^{II}, cyan; O, red; N, blue; C, grey. Reproduced from Ref. 87.

Discrete 3*d*/4*f*-metal clusters are not the only form of compounds that have been assessed for the magnetocaloric effect. 1-D coordination polymers containing Cu^{II}/Gd^{III} are also of interest for their magnetocaloric properties. In 2013, Ruiz, Tong, and coworkers reported a 1-D chain containing repeating $\{Cu_2Gd_2\}$ units (Figure 1.38).[88] The compound was synthesized using a combination of 2-pyridinemethanol, $Gd(NO_3)_3 \cdot 6H_2O$, $Cu(O_2CMe)_2 \cdot H_2O$, and Et_3N, in a 1:1:2:2 molar ratio in solvent MeCN. An interesting feature of this polymer is that the *dc* magnetic susceptibility studies and magnetization versus field studies determined the presence of dominant antiferromagnetic interactions in the chain, but a non-zero spin ground state was also confirmed. While the presence of antiferromagnetic exchange interactions is not desirable for a molecular magnetic refrigerant, the non-zero spin ground state still allows for a change in the magnetic entropy. The compound was found to have an experimental $-\Delta S_m$ value of 25.7 J kg^{-1} K^{-1}. This value is the largest of any Cu^{II}/Gd^{III} 1-D chains found to date. The examples presented here show the promise in researching molecular magnetic refrigerants, and how much there is to learn and discover toward the isolation of compounds with larger values of $-\Delta S_m$.

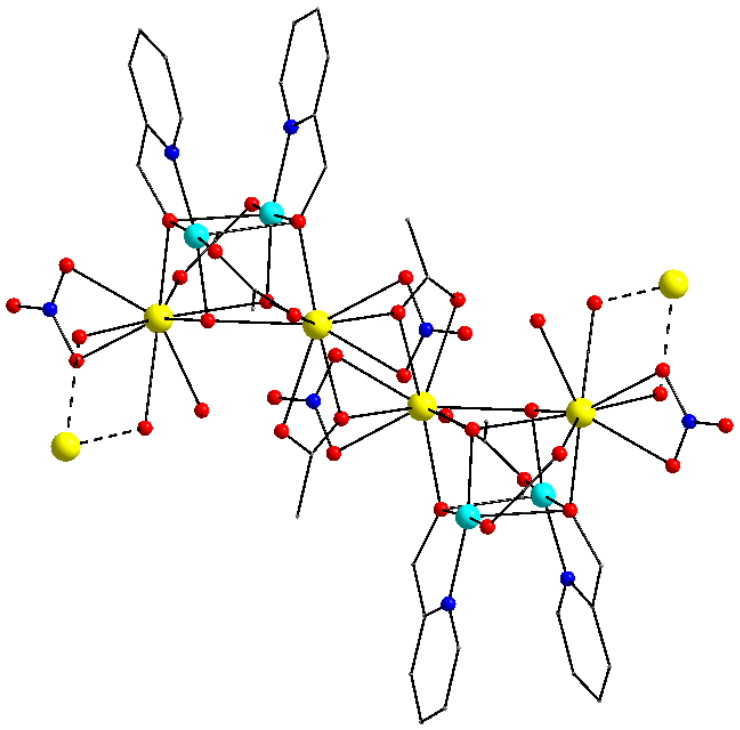

Figure 1.38. Structure of the $\{Cu_2Gd_2\}_n$ chain reported by Ruiz, Tong, and coworkers. The extension of the polymer in 1-D is indicated through the hashed bonds. H atoms are omitted for clarity. Colour scheme: Gd^{III}, yellow; Cu^{II}, cyan; O, red; N, blue; C, grey. Reproduced from Ref. 88.

1.8. Long- and Short-Term Research Objectives

Ultimately, the long-term objective presented in this thesis is the synthesis and characterization of novel polynuclear and heterometallic 3*d*/4*f*-metal clusters, employing Cu^{II} and various Ln^{III} ions. Further goals are for the isolated compounds to possess interesting structural motifs, but more importantly, for the compounds to exhibit single-molecule magnetism or the magnetocaloric effect, depending on the Ln^{III} ion used. To accomplish this long-term goal,

the project was divided into several short-term research objectives. These objectives are as follows: (a) the synthesis and structural characterization (through single-crystal X-ray crystallography) of heterometallic Cu^{II}/Ln^{III} clusters with the commercially available ligand naphthalene-2,3-diol (ndH_2, Scheme 1.3), as well as Cu^{II}/Ln^{III} clusters with the new dioxime ligand acenaphthenequinone dioxime ($acndH_2$, Scheme 1.3); (b) the complete spectroscopic and physicochemical characterization of all synthesized compounds; (c) the performance of *dc* and *ac* magnetic susceptibility studies to analyze the bulk magnetic properties of the compounds, as well as the magnetization dynamics; and (d) the performance of heat capacity studies on Cu^{II}/Gd^{III} compounds which show the potential to act as molecular magnetic refrigerants.

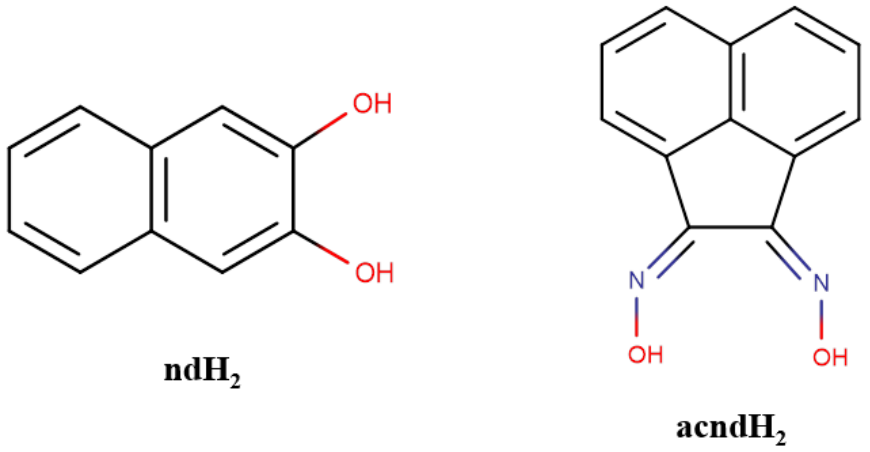

ndH_2 **$acndH_2$**

Scheme 1.3. The organic chelating/bridging ligands used in the present thesis for the synthesis of new Cu^{II}/Ln^{III} metal clusters.

CHAPTER 2: 'All three-in-one': ferromagnetic interactions, single-molecule magnetism and magnetocaloric properties in a new family of [Cu_4Ln] (Ln^{III} = Gd, Tb, Dy) clusters

2.1. Experimental Section

2.1.1. Physical Measurements

Elemental Analysis: Elemental analyses (C, H, N) were performed on a Perkin-Elmer 2400 Series II Analyzer.

FT-IR spectroscopy: Infrared (IR) spectra were recorded in the solid state using a Bruker FT-IR spectrometer (ALPHA Platinum ATR single reflection) in the 4000-400 cm^{-1} range. The notation for the IR bands is as follows: vs, very strong; s, strong; m, medium; w, weak; b, broad.

Magnetic susceptibility studies: Variable-temperature direct and alternating current (*dc* and *ac*, respectively) magnetic susceptibility studies were performed at the State Key Laboratory of Rare Earth Resource Utilization, part of the Changchun Institute of Applied Chemistry in the Chinese Academy of Sciences. Data was collected using a Quantum Design SQUID magnetometer, equipped with a 7 T magnet and with an operating temperature range of 2 – 300

K. The *dc* magnetic susceptibility studies were carried out in an applied field of 0.1 T, while the *ac* studies utilized an oscillating field of 0.0003 T under a variety of different *ac* frequencies.

Specific heat studies: Specific heat measurements were carried out at temperatures down to 0.3 K by using a Quantum Design PPMS magnetometer equipped with a ^{3}He cryostat. The experiments were performed on thin pressed pellets (approximately 1 mg) of a polycrystalline sample, thermalized by approximately 0.2 mg of Apiezon N grease, whose contribution was subtracted using a phenomenological expression.

2.1.2. Synthesis

General Considerations: All experiments were performed under aerobic conditions and at ambient temperature. The chemicals needed for the synthesis of the reported compounds were acquired from Alfa Aesar and Sigma Aldrich (reagent grade). These chemicals were all used as received. Solvents (reagent grade) were also used as received.

$(NHEt_3)_5[Cu_4Gd(nd)_8]$ (1): To a stirred, colourless solution of ndH_2 (0.11 g, 0.7 mmol) and NEt_3 (196 μL, 1.4 mmol) in MeOH (20 mL) were added $Cu(ClO_4)_2{\cdot}6H_2O$ (0.04 g, 0.1 mmol) and $Gd(ClO_4)_3{\cdot}6H_2O$ (0.06 g, 0.1 mmol). The resulting dark green solution was kept under stirring at room temperature for about 20 min, filtered, and the filtrate was diffused with Et_2O (40 mL). Slow mixing gave after 5 days dark green plate-like crystals of **1**, which were collected by filtration, washed with cold MeOH (2 x 2 mL) and Et_2O (2 x 2 mL), and dried under vacuum. The yield was 68 %. Elemental analysis (%) calculated for lattice solvent-free $C_{110}H_{128}Cu_4GdN_5O_{16}$ (**1**): C 60.39, H 5.90, N 3.20; found: C 60.48, H 5.97, N 3.06.

$(NHEt_3)_5[Cu_4Tb(nd)_8]$ (2): This complex was prepared in the same manner as complex **1** but using $Tb(ClO_4)_3 \cdot 5H_2O$ (0.06 g, 0.1 mmol) in place of $Gd(ClO_4)_3 \cdot 6H_2O$. After 5 days, dark green plate-like crystals of **2** were collected by filtration, washed with cold MeOH (2 x 2 mL) and Et_2O (2 x 2 mL), and dried under vacuum. The yield was 60 %. Elemental analysis (%) calculated for lattice solvent-free $C_{110}H_{128}Cu_4TbN_5O_{16}$ (**2**): C 60.35, H 5.89, N 3.20; found: C 60.45, H 5.99, N 3.01.

$(NHEt_3)_5[Cu_4Dy(nd)_8]$ (3): This complex was prepared in the same manner as complex **1** but using $Dy(ClO_4)_3 \cdot 6H_2O$ (0.06 g, 0.1 mmol) in place of $Gd(ClO_4)_3 \cdot 6H_2O$. After 6 days, small dark green plate-like crystals of **3** were collected by filtration, washed with cold MeOH (2 x 2 mL) and Et_2O (2 x 2 mL), and dried under vacuum. The yield was 55 %. Elemental analysis (%) calculated for lattice solvent-free $C_{110}H_{128}Cu_4DyN_5O_{16}$ (**3**): C 60.25, H 5.88, N 3.19; found: C 60.35, H 6.04, N 3.11.

2.1.3. Single-crystal X-ray Crystallography

Single-crystals of complexes **1** and **2** were selected and mounted on cryoloops using adequate oil.[89] Diffraction data were collected on a Bruker X8 Kappa APEX II Charge-Coupled Device (CCD) area-detector diffractometer controlled by the APEX2 software package[90] (Mo Kα graphite-monochromated radiation, λ = 0.71073 Å), and equipped with an Oxford Cryosystems Series 700 cryostream, monitored remotely with the software interface Cryopad.[91] Images were processed with the software SAINT+,[92] and the absorption effects were corrected by the multi-scan method implemented in SADABS.[93] The structures were solved using the algorithm implemented in SHELXT-2014,[94,95] and refined by successive full-matrix least-squares cycles on

F^2 using the latest SHELXL-v.2014.[95,96] Unfortunately, it has been unfeasible to grow crystals of suitable size for the acquisition of a complete X-ray data set for complex **3**.

All the non-hydrogen atoms of the complexes in both structures were successfully refined using anisotropic displacement parameters, while a few carbon atoms of the countercations were only refined with isotropic parameters. Hydrogen atoms bonded to carbon were placed at their idealized positions using appropriate *HFIX* instructions in SHELXL (43 for the aromatic carbons), and included in subsequent refinement cycles in riding-motion approximation with isotropic thermal displacement parameters (U_{iso}) fixed at 1.2 × U_{eq} of the relative atom. Unit cell parameters, structure solution and refinement details for **1** and **2** are summarized in Table 2.1.

Table 2.1. Crystallographic data for complexes **1** and **2**.

Parameter	**1**	**2**
Formula	$C_{110}H_{128}Cu_4GdN_5O_{16}$	$C_{110}H_{128}Cu_4N_5O_{16}Tb$
Fw / g mol^{-1}	2187.58	2189.25
Crystal type	Green plate	Green prism
Crystal size / mm^3	0.31 × 0.12 × 0.03	0.31 × 0.26 × 0.21
Crystal system	Tetragonal	Tetragonal
Space group	$P\bar{4}2_1/c$	$P\bar{4}2_1/c$
a / Å	30.4012(17)	30.3009(19)
b / Å	30.4012(17)	30.3009(19)
c / Å	23.676(3)	23.5735(15)
α / º	90	90

β / º	90	90
γ / º	90	90
Volume / Å^3	21882(4)	21664(3)
Z	8	8
Temperature / K	150(2)	150(2)
D_c / g cm^{-3}	1.328	1.344
μ / mm^{-1}	1.425	1.482
θ range (°)	3.69 – 25.02	3.71 – 25.03
Index ranges	$-36 \le h \le 35$	$-27 \le h \le 36$
	$-32 \le k \le 36$	$-35 \le k \le 36$
	$-27 \le l \le 28$	$-28 \le l \le 27$
Collected reflections	397362	120629
Independent reflections	19251 (R_{int} = 0.0916)	18921 (R_{int} = 0.0576)
Data completeness	to θ = 25.03º, 99.4%	to θ = 25.03º, 99.5%
Final $R^{a,b}$ indices [$I>2\sigma(I)$]	$R1$ = 0.0644	$R1$ = 0.0612
	$wR2$ = 0.1536	$wR2$ = 0.1510
Final R indices (all data)	$R1$ = 0.0784	$R1$ = 0.0788
	$wR2$ = 0.1623	$wR2$ = 0.1641
$(\Delta\rho)_{max,min}$ / e Å^{-3}	1.199 and −0.622	1.409 and −0.639

[a] $R1 = \Sigma(||F_o| - |F_c||)/\Sigma|F_o|$. [b] $wR2 = [\Sigma[w(F_o^2 - F_c^2)^2]/\Sigma[w(F_o^2)^2]]^{1/2}$, $w = 1/[\sigma^2(F_o^2) + (ap)^2 + bp]$, where $p = [\max(F_o^2, 0) + 2F_c^2]/3$.

2.2. Results and Discussion

2.2.1. Synthetic Comments

Initial work in the synthesis of heterometallic 3*d*/4*f* polynuclear metal clusters arose from a desire to study interesting magnetic properties. In addition to single-molecule magnetism properties, there was an interest in studying the magnetocaloric properties of the synthesized compounds, to see if the compounds would act as molecular magnetic refrigerants. The project was approached by using serendipitous assembly, employing Ln^{III} and Cu^{II} starting materials combined with the aromatic diol ligand naphthalene-2,3-diol (ndH_2).

Metal starting materials with the general formula LnX_3 and CuX_2 were employed in this project, in conjunction with the ligand ndH_2. Simple X^- ions, such as Cl^-, ClO_4^- and NO_3^-, have limited bridging affinity, and as such, the metal ions of such salts would likely be aggregated by the organic ligand alone in the reaction mixture. On the other hand, carboxylates and β-diketonates are groups that have additional bridging potential, which would have a distinct effect on the identity of any products isolated compared to the simple ions. In this research, no carboxylate- or β-diketonate-containing metal salts were used, allowing ndH_2 to act as the sole chelating/bridging ligand in the reaction mixture.

Many different metal-to-ligand ratios were used in this research, as well as different solvents, metal starting materials, and organic bases. Thus, the combination of $Cu(ClO_4)_2{\cdot}6H_2O$, $Ln(ClO_4)_3{\cdot}6H_2O$, ndH_2 and NEt_3 in solvent MeOH in a 1:1:7:14 molar ratio, under vapour diffusion with Et_2O, yielded a family of $\{Cu_4Ln\}$ clusters (Ln^{III} = Gd^{III}, Tb^{III}, Dy^{III}), as summarized in the stoichiometric Equation 2.1. Varying the stoichiometry did not yield any crystalline products but only brown amorphous precipitates whose identity was not identical to the $\{Cu_4Ln\}$ products (confirmed through IR spectroscopy). Varying the organic bases, which

facilitate the complete deprotonation of the ndH_2 ligand, it has been possible to obtain similar $\{Cu_4Ln\}$ complexes albeit with different countercations in the crystal lattice. Complexes **1-3** were therefore established as the most thermodynamically stable and crystalline compounds under the reported reaction conditions.

$$4\,Cu^{2+} + Ln^{3+} + 8\,ndH_2 + 16\,NEt_3 \xrightarrow{MeOH/Et_2O}$$

$$[Cu_4Ln(nd)_8]^{5-} + 16\,HNEt_3^+ \qquad \textbf{(Eqn. 2.1)}$$

$$Ln = Gd\ (\mathbf{1});\ Tb\ (\mathbf{2});\ Dy\ (\mathbf{3})$$

As an extension of this research, the diol ligand catechol ($catH_2$) was employed to see if any crystalline product could be isolated, using both the stoichiometric reaction (molar ratio; 4:1:8:16) as well as the identical initial synthetic conditions (molar ratio; 1:1:7:14). No crystalline products were isolated using $catH_2$, while only brown solids were obtained which have been impossible to crystallize and determine their crystal structures. This is indicative of the thermodynamic stability provided to the system through the naphthalene functionality of the ligand ndH_2.

The most notable difference between the IR spectrum of the free organic ligand, ndH_2, and the spectra of complexes **1-3** arises from the ν(O-H) stretching vibration. In the spectrum of ndH_2, the broad band seen in the region 3500-3200 cm^{-1} is indicative of the protonated -OH functional groups. However, in metal complexes **1-3**, this band disappears, confirming that the ligand has been doubly-deprotonated and coordinated to the metal ions. The IR spectra of complexes **1-3** are identical, as expected for isostructural compounds (see the Appendix).

2.2.2. Description of Structures

In view of the structural similarities of **1-3**, only the structure of $(NHEt_3)_5[Cu_4Gd(nd)_8]$ (**1**) will be described as a representative example. The molecular structure of the anion of **1** (Figure 2.1) consists of a central Gd^{III} ion surrounded by four Cu^{II} ions in a 'propeller'-like conformation. For polynuclear metal complexes, where metal ions are bridged by O- and N-donor atoms and not through metal-metal bonds, there is still a preference from the community in utilizing almost exclusively the eta (η) convention instead of kappa (κ). Indeed, according to the International Union of Pure and Applied Chemistry the eta (η) nomenclature should be used for any cases where the central atom is bonded to contiguous donor atoms (IUPAC; IR-9: Coordination Compounds). To that end, eight doubly deprotonated nd^{2-} ligands serve to bridge the Gd^{III} ion with the outer Cu^{II} ions using one of the two alkoxido arms; these ligands are thus $\eta^1:\eta^2:\mu$ (Scheme 2.1). The non-bridging O atoms of nd^{2-} are strongly hydrogen-bonded to the Et_3NH^+ countercations, thus enhancing the overall stability and crystallinity of **1**.

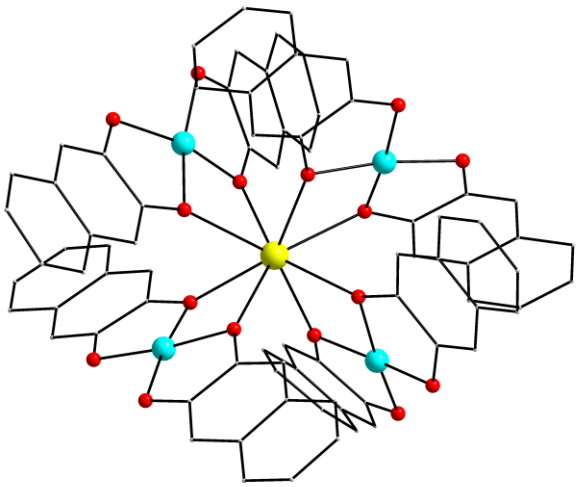

Figure 2.1. Molecular structure of the $[Cu_4Gd(nd)_8]^{5-}$ anion of complex **1**. H atoms have been omitted for clarity. Colour scheme: Gd^{III}, yellow; Cu^{II}, cyan; O, red; C, grey.

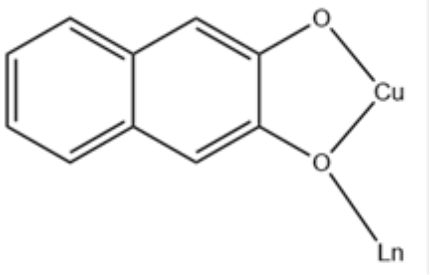

$\eta^1:\eta^2:\mu$

Scheme 2.1. Crystallographically established coordination mode of the ligand nd^{2-} present in complexes **1** and **2**.

Peripheral ligation about the $[Cu_4Gd(\mu\text{-}OR)_8]^{3+}$ core (Figure 2.2) is provided by the chelating part of the eight naphthalene-2,3-diol groups. The four Cu^{II} ions occupy the vertices of a distorted, non-planar Cu_4 rectangle (Figure 2.3) while the central Gd^{III} ion is displaced 0.14 Å away from the Cu_4 best-mean-plane. The Cu^{II} ions are not directly linked to each other but only through the Gd^{III} mediator; hence, there are no significant interactions between the 3*d*-metal ions.

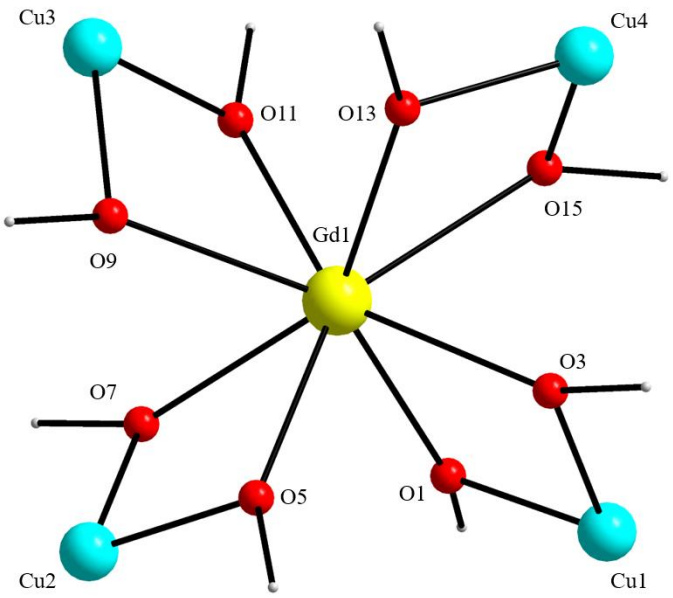

Figure 2.2. Complete and labeled $[Cu_4Gd(\mu\text{-}OR)_8]^{3+}$ core of **1**. Colour scheme: Gd^{III}, yellow; Cu^{II}, cyan; O, red; C, grey.

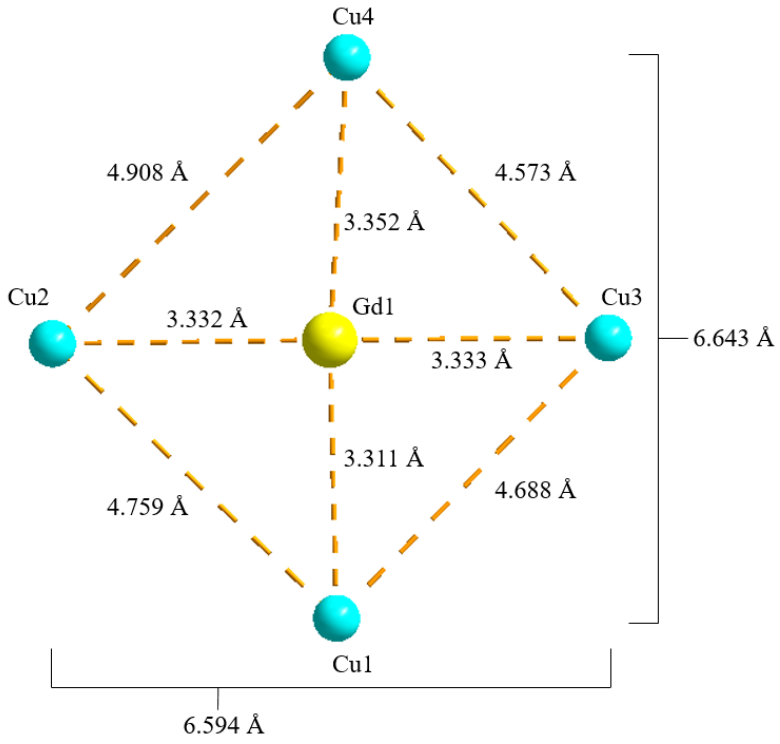

Figure 2.3. The {Cu_4Gd} metal topology and the corresponding metal···metal distances.

The Cu^{II}–O–Gd^{III} angles span the range 97.1(2)–102.7(2)°. All Cu^{II} ions are four-coordinate with distorted square planar geometries: the *cis*- and *trans*-angles lie in the 86.3–99.7° and 164.9–174.5° ranges, deviating only slightly from the 90° and 180°, respectively, of an ideal square plane. The tetrahedrality[97] calculated for Cu1, Cu2, Cu3, and Cu4 in **1** gives average dihedral angles of ~18, ~8, ~11, and ~10°, respectively, supporting the distorted square planar geometry for the basal Cu(1,2,3,4)O_4 planes. The central Gd^{III} ion is eight-coordinate with a triangular dodecahedral coordination geometry (CShM value = 0.76, program SHAPE;[98] see Figure 2.4 and Table 2.2). The Tb^{III} ion of complex **2** is also eight-coordinate with triangular dodecahedral coordination geometry (CShM value = 0.81, program SHAPE;[98] see Figure 2.4 and Table 2.2). Finally, the reported compounds join only a handful of previously reported {Cu_4Ln} clusters[99] albeit they are the first 'propeller'-like clusters exhibiting SMM behaviour and MCE properties (*vide infra*).

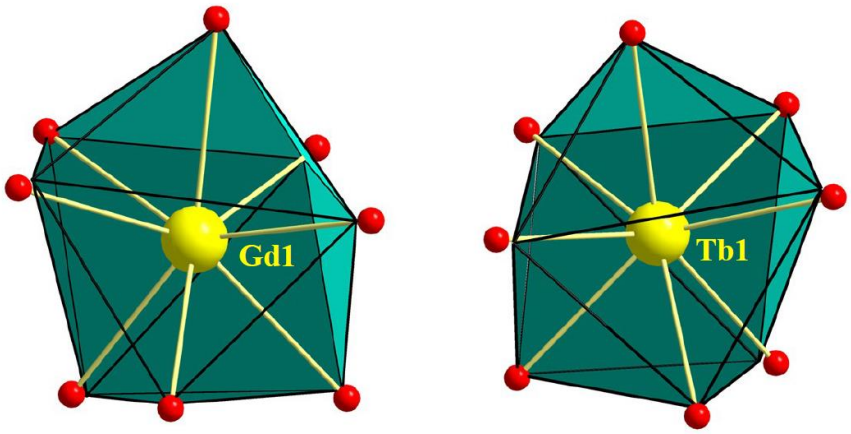

Figure 2.4. Triangular dodecahedron coordination geometries of Gd1 and Tb1 atoms in the structures of complexes **1** and **2**, respectively. Points connected by the black thin lines define the vertices of the ideal polyhedron. Values of CShM between 0.1 and 3 usually correspond to a not negligible but still small distortion from ideal geometry.

Table 2.2. SHAPE measures of the 8-coordinate Gd1 and Tb1 coordination polyhedra in complexes **1** and **2**, respectively.[a]

Polyhedron[b]	Gd1	Tb1
OP-8	25.17	25.06
HPY-8	24.55	24.67
HBPY-8	16.57	16.75
CU-8	9.11	9.25
SAPR-8	1.32	1.23
TDD-8	**0.76**	**0.81**
JGBF-8	15.16	14.97
JETBPY-8	28.04	27.96
JBTPR-8	2.50	2.48
BTPR-8	1.92	1.91
JSD-8	2.88	2.94
TT-8	9.87	10.02
ETBPY-8	23.40	23.15

[a] The values in boldface indicate the closest polyhedron according to the Continuous Shape Measures (CShM). [b] Abbreviations: OP-8, octagon; HPY-8, heptagonal pyramid; HBPY-8, hexagonal bipyramid; CU-8, cube; SAPR-8, square antiprism; **TDD-8, triangular dodecahedron**; JGBF-8, Johnson gyrobifastigium; JETBPY-8, Johnson elongated triangular bipyramid; JBTPR-8, Johnson biaugmented trigonal prism; BTPR-8, biaugmented trigonal prism; JSD-8, Johnson snub diphenoid; TT-8, triakis tetrahedron; ETBPY-8, elongated trigonal bipyramid.

2.2.3. Solid-state Magnetic Susceptibility Studies

Solid-state direct current (*dc*) magnetic susceptibility (χ_M) data on dried and analytically-pure samples of **1**–**3** were collected in the 2.0–300 K range in an applied field of 0.1 T, and are plotted as $\chi_M T$ versus T in Figure 2.5. The experimental $\chi_M T$ values at 300 K for all complexes are in excellent agreement with the theoretical ones expected for four Cu^{II} (S = 1/2, g = 2.2) and one Gd^{III} (9.69 cm^3 K mol^{-1}) or Tb^{III} (13.64 cm^3 K mol^{-1}) or Dy^{III} (15.99 cm^3 K mol^{-1}) non-interacting ions. The magnetic behaviour of **1**–**3** indicates ferromagnetic exchange interactions between the Cu^{II} and Ln^{III} ions, with the $\chi_M T$ products steadily increasing with decreasing temperature to reach the values of 17.91 (**1**), 18.72 (**2**), and 21.67 (**3**) cm^3 K mol^{-1} at T = 2, 3, and 2.5 K, respectively. The $\chi_M T$ value of **1** at 2 K is in excellent agreement with the value of 17.88 cm^3 K mol^{-1}, expected for an S = 11/2 system with g = 2. For the anisotropic analogues **2** and **3**, the $\chi_M T$ products slightly decrease below ~3 K, indicating the presence of magnetic anisotropy and/or depopulation of the excited m_J states.

For the isotropic analogue **1**, the PHI program[100] and the spin-Hamiltonian, $H = -J\,(\hat{S}_{Cu1}\cdot\hat{S}_{Gd1} + \hat{S}_{Cu2}\cdot\hat{S}_{Gd1} + \hat{S}_{Cu3}\cdot\hat{S}_{Gd1} + \hat{S}_{Cu4}\cdot\hat{S}_{Gd1})$, were used to fit the susceptibility and magnetization data. An excellent fit of the experimental data (solid blue line in Figure 2.5) gave as best-fit parameters: J = +1.31(4) cm^{-1} and g = 2.00(4), thus confirming the intramolecular ferromagnetic interactions between the metal ions and the stabilization of an S = 11/2 spin ground state for **1**. Note that the introduction of an additional J-coupling constant, to consider any possible Cu···Cu magnetic interactions, in the above spin-Hamiltonian did not improve the fit and gave almost identical $J_{Cu\cdots Gd}$ (+1.36 cm^{-1}) and $J_{Cu\cdots Cu} \sim 0$ cm^{-1} values. The obtained J value of **1** is of the same order of magnitude, although somewhat smaller than those observed in other {Cu_4Gd}

clusters in which the Cu^{II} ions are magnetically coupled to each other ($J_{Cu\cdots Cu} \neq 0$).[100] The weak ferromagnetic interactions in **1** are likely resulted from the orthogonality of the *d*- and *f*-metal orbitals.[36,85,100]

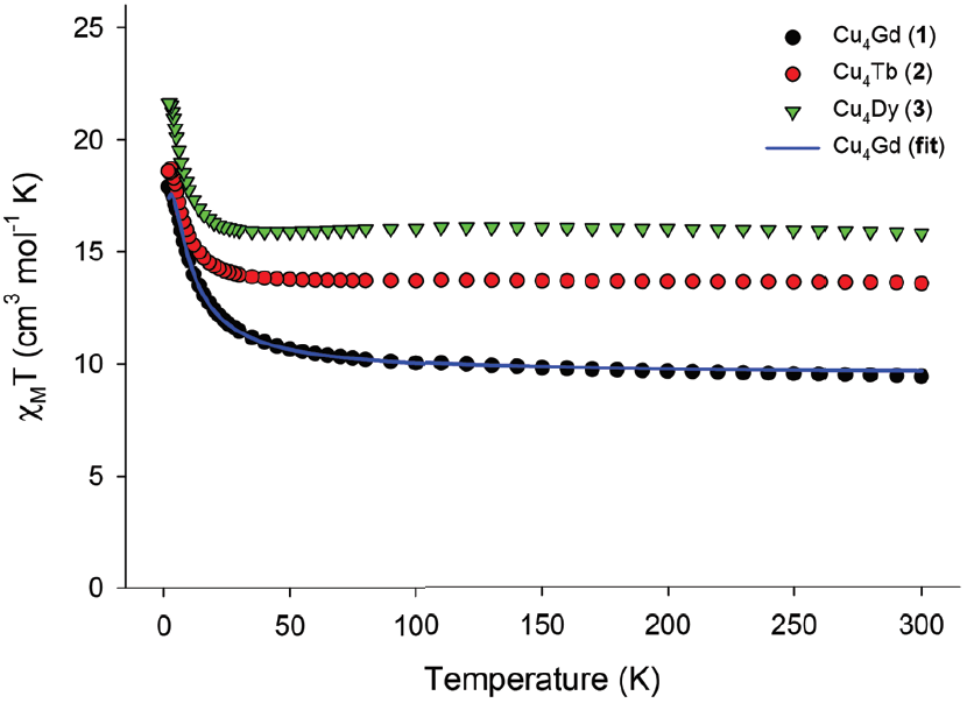

Figure 2.5. $\chi_M T$ versus T plots for **1**–**3** in an applied *dc* field of 0.1 T. Solid blue line is the result of the fit for the {Cu_4Gd} compound, as described in the text.

Magnetization (*M*) versus field (*H*) studies for **1**–**3** showed fast saturated variations (Figure 2.6), further confirming the presence of predominant ferromagnetic interactions in all compounds. The magnetization of **1** at 1.9 K saturates fast and in small fields to a value of ~11 $N\mu_\beta$ consistent with an S = 11/2 spin ground state. To evaluate the accuracy of the susceptibility data, the magnetization data of **1** were also fitted using the previously described spin-Hamiltonian. Best-fit parameters are: J = +1.34 cm^{-1} and g = 2.02. The *M* versus *H* plots for **2**

and **3** between 1.9 and 5 K justify the presence of magnetic anisotropy, since the data are not superimposed on a single master curve (Figure 2.7).

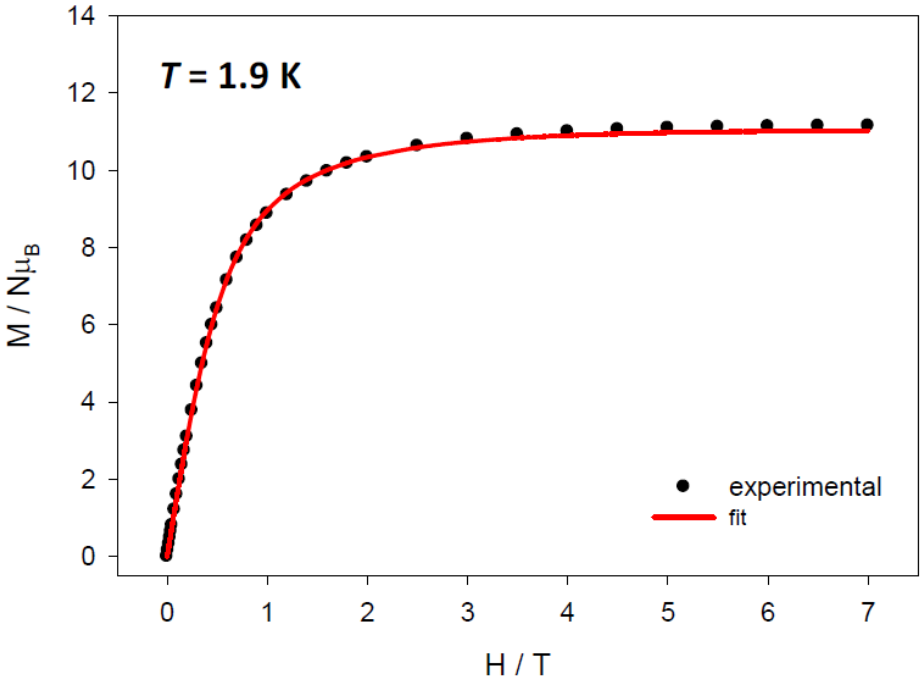

Figure 2.6. Magnetization (*M*) versus field (*H*) plot for the {Cu_4Gd} complex. The red line is the fit of the data; see the text for fit parameters.

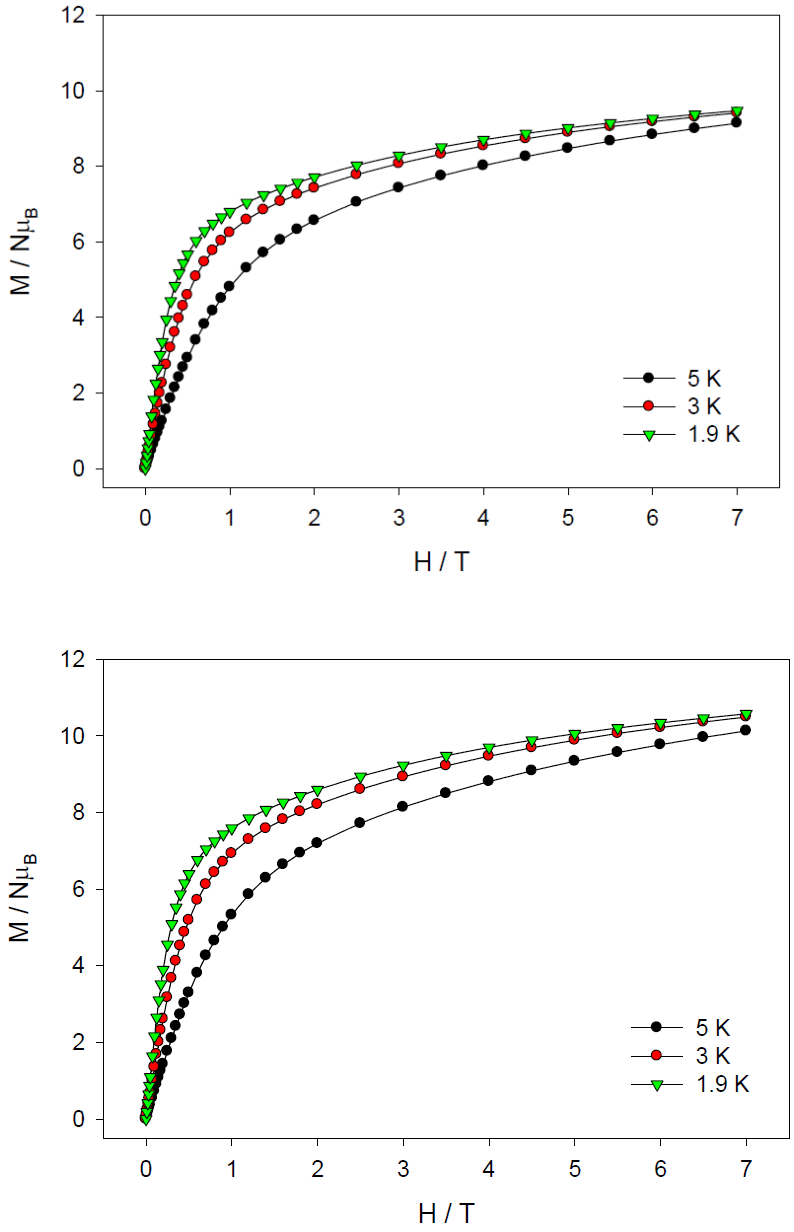

Figure 2.7. Magnetization (*M*) versus field (*H*) plots for the {Cu_4Tb} (top) and {Cu_4Dy} (bottom) complexes performed at a variety of temperatures. The solid lines are guides for the eye.

Alternating current (*ac*) magnetic susceptibility studies have been also carried out in order to investigate the magnetization dynamics of **2** (Figure 2.8) and **3** in the absence of an external *dc* magnetic field. Only the {Cu_4Dy} analogue showed frequency-dependent in-phase (χ'_M) and out-of-phase (χ''_M) tails of signals at temperatures below ~5 K (Figure 2.9), characteristic of the slow magnetization relaxation of a fast-relaxing SMM with a relatively small energy barrier for the magnetization reversal. Such behaviour most likely arises from predominant single-ion effects of the Dy^{III} ion within **3**; note that Dy^{III} is a Kramers ion, and irrespective of the ligand field it is expected to possess a bistable ground state.[101] On the other hand, Tb^{III} is a non-Kramers ion and so its complexes will have a bistable ground state only if it has an axially-symmetric ligand field.[101] Efforts to shift the χ''_M tails of signals of **3** to higher temperatures and surpass the fast tunneling of both **2** and **3** by applying an external *dc* field were all failed to improve the magnetization dynamics.

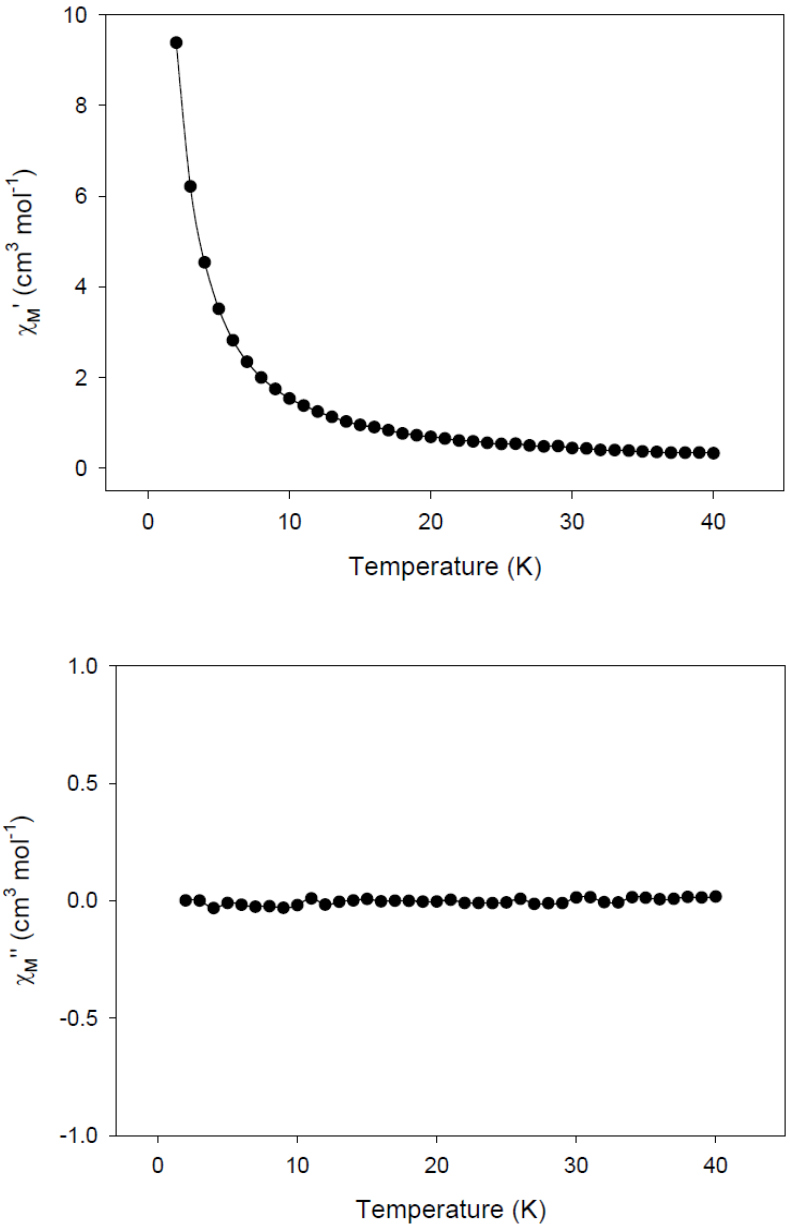

Figure 2.8. Temperature dependence of the in-phase χ'_M (top) and out-of-phase χ''_M (bottom) *ac* susceptibility signals of {Cu_4Tb} in a 3 G field oscillating at the frequency of 997 Hz.

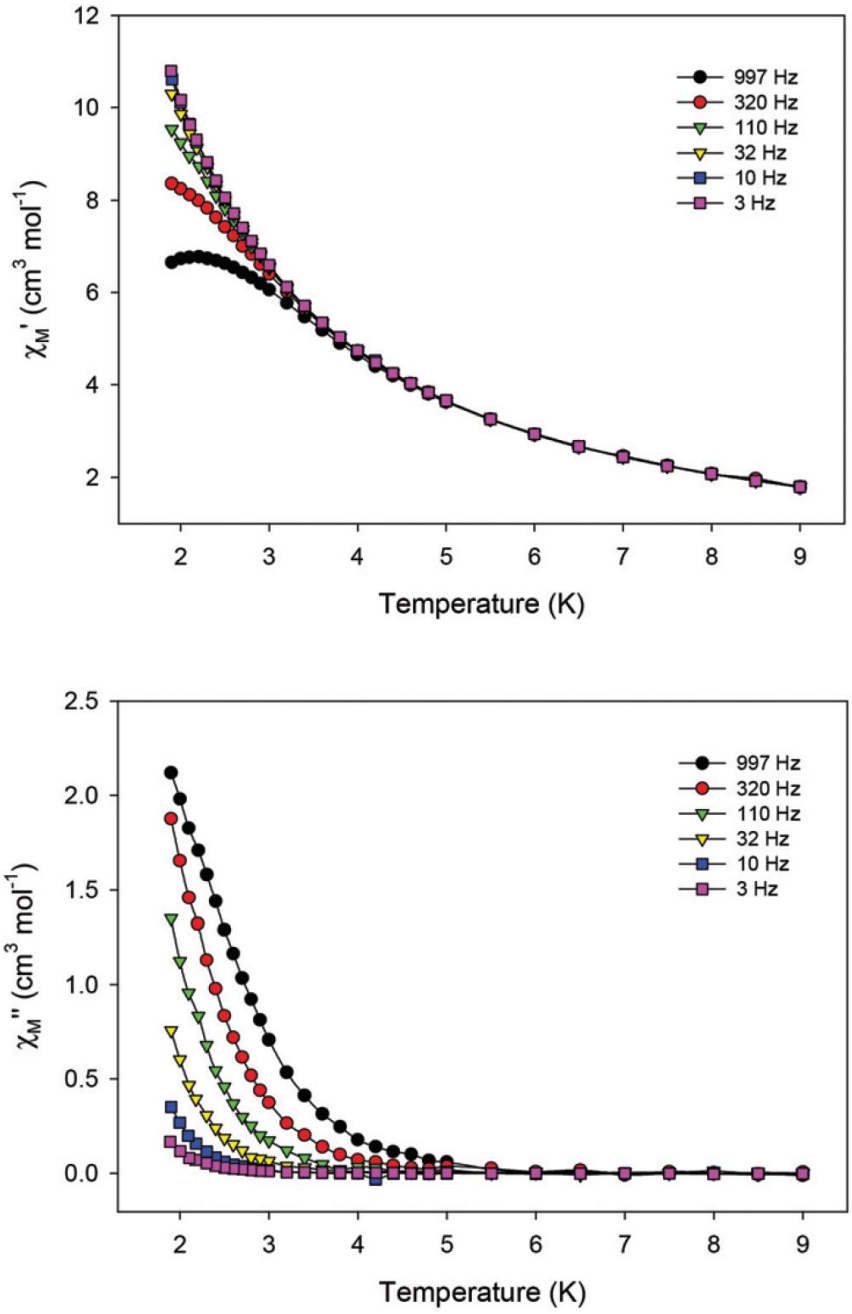

Figure 2.9. Temperature dependence of the in-phase χ'_M (top) and out-of-phase χ''_M (bottom) *ac* susceptibility studies of {Cu_4Dy} in a 3 G oscillating at the indicated frequencies.

2.2.4. Magnetocaloric Properties

Given the recent interest in Cu/Gd-clusters as low temperature magnetic coolers,[80,102] and the large magnetization value of **1** as a result of the ferromagnetic interactions between the metal ions, it was decided to pursue magnetocaloric studies. The magnetic entropy change, $-\Delta S_m$, as derived from heat capacity (Figure 2.10, top) and magnetization data is reported. Values of ΔS_m can be obtained from the *T* and field dependencies of the entropy (Figure 2.10, bottom).

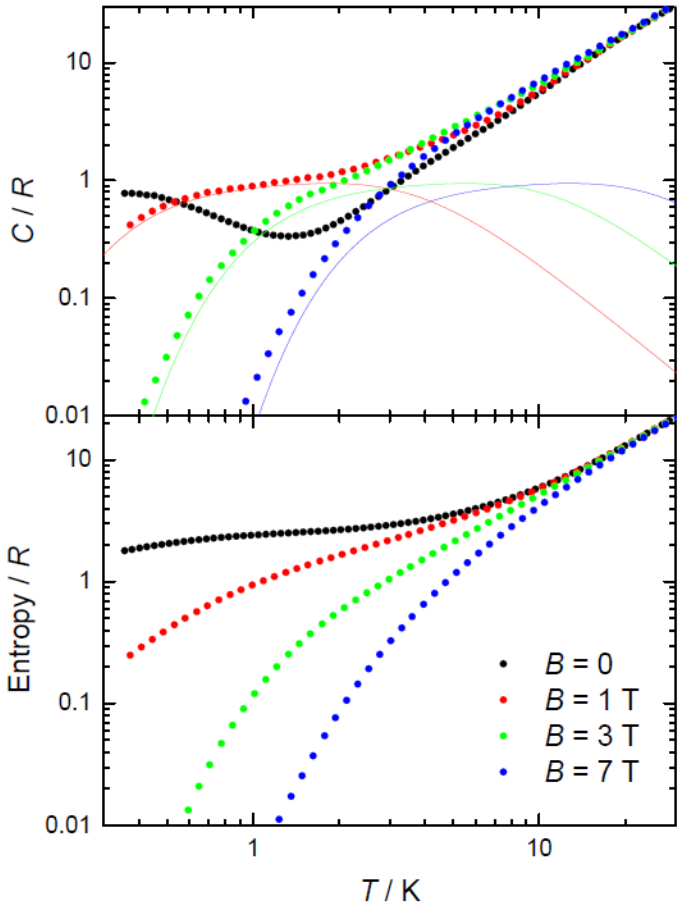

Figure 2.10. (top) *T*-dependence of the molar specific heat for {Cu_4Gd} at the indicated fields. The nonmagnetic lattice specific heat dominates at high temperatures, while the field-dependent contribution can be well described by the Schottky specific heat (solid lines) for non-interacting $S = 11/2$ spins, as proper for ferromagnetic {Cu_4Gd} clusters. (bottom) Magnetic entropy versus *T* as obtained from the specific heat data for {Cu_4Gd}.

The maximum $-\Delta S_m$ for **1** was achieved with ΔB = 7 T at T = 3 K; however, the obtained value of ~10 J kg^{-1} K^{-1} is much lower than the maximum entropy value per mole (4.85R ~ 18.43 J kg^{-1} K^{-1}) for 4 Cu^{II} and 1 Gd^{III} fully decoupled ions. This indicates that the magnetic coupling, J, between the five metal ions is accountable for the obtained $-\Delta S_m$ value. Indeed, for an S = 11/2 coupled spin system the maximum $-\Delta S_m$ expected is given by $R\ln(2S + 1) = R\ln 12 = 2.5R \sim 9.5$ J kg^{-1} K^{-1}; the latter value is in excellent agreement with the experimental $-\Delta S_m$ for **1**, highlighting the effect of the magnitude of J on the MCE (Figure 2.11).

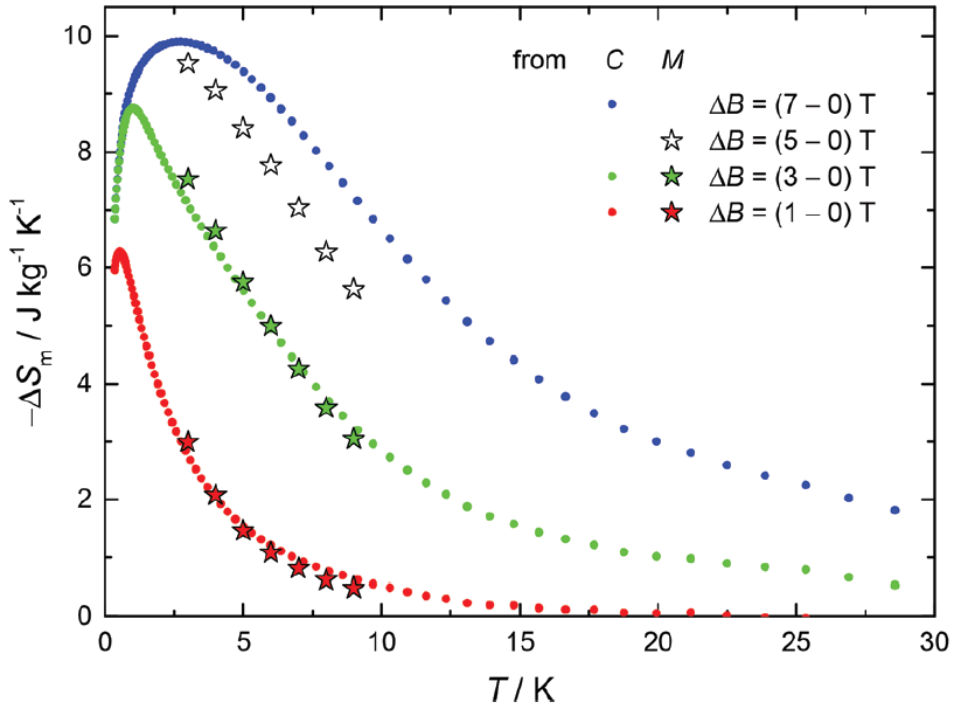

Figure 2.11. Magnetic entropy change for {Cu$_4$Gd} (**1**), as obtained from heat capacity (C) and magnetization (M) experiments for the indicated applied field changes.

2.3. Conclusions and Perspectives

In conclusion, it was shown that the choice of a capable organic chelating/bridging ligand in Cu/Ln chemistry can provide the means of obtaining new cluster compounds with interesting topologies and diverse magnetic properties. Complex **1** was found to act as a molecular magnetic refrigerant, complex **3** exhibited SMM behaviour, and all three complexes showed the presence of ferromagnetic exchange interactions between the $Cu^{II}\cdots Ln^{III}$ ions. The key feature of this work was to show that the ligand ndH_2, which has been previously employed in homometallic 4*f*-metal cluster chemistry,[26] could be successfully applied to heterometallic 3*d*/4*f*-metal cluster chemistry as well. Indeed, it was found that polynuclear metal complexes could be isolated from the use of this ligand. Work in progress includes the synthesis and complete characterization of the remaining members of this family of $\{Cu_4Ln\}$ clusters and the elucidation of their photophysical properties.

In keeping within the research interest of 3*d*/4*f*-metal cluster chemistry, a crossroads was reached in terms of the direction of the research. One option would be the continued employment of ndH_2 and exploring other 3*d*-metals than Cu^{II}, while the second option is continuing in Cu^{II}/Ln^{III} metal cluster chemistry with an entirely new ligand system. Towards that end, it was decided to move onto other type of ligand systems, specifically dioxime-type ligands. Dioximes have been shown to promote strong magnetic interactions between metal ions and have various bridging and chelating capabilities with both 3*d*- and 4*f*-metal ions. Consequently, a new dioxime-type ligand was explored in Cu^{II}/Ln^{III} cluster chemistry, and the results are presented in Chapter 3.

CHAPTER 3: New dioximes as bridging ligands in 3*d*/4*f*-metal cluster chemistry: 1-D chains of $\{Cu_6Ln_2\}$ clusters bearing acenaphthenequinone dioxime and exhibiting slow magnetization relaxation and magnetocaloric properties

3.1. Experimental Section

3.1.1. Physical Measurements

Elemental Analysis: Elemental analyses (C, H, N) were performed on a Perkin-Elmer 2400 Series II Analyzer.

FT-IR spectroscopy: Infrared (IR) spectra were recorded in the solid state using a Bruker FT-IR spectrometer (ALPHA Platinum ATR single reflection) in the 4000 – 400 cm^{-1} range. The notation for the IR bands is as follows: vs, very strong; s, strong; m, medium; w, weak; b, broad.

NMR spectroscopy: NMR spectra were recorded on a Bruker 300 MHz spectrometer at Brock University. All chemical shifts are referenced to tetramethylsilane [$Si(CH_3)_4$] or a residual

non-deuterated solvent. Data for proton spectra are reported as follows: chemical shift multiplicity [singlet (s) and doublet (d)].

Magnetic susceptibility studies: Variable-temperature direct and alternating current (*dc* and *ac*, respectively) magnetic susceptibility studies were performed at the State Key Laboratory of Rare Earth Resource Utilization, part of the Changchun Institute of Applied Chemistry in the Chinese Academy of Sciences. Data was collected using a Quantum Design SQUID magnetometer, equipped with a 7 T magnet and with an operating temperature range of 2 – 300 K. The *dc* magnetic susceptibility studies were carried out in an applied field of 0.1 T, while the *ac* studies utilized an oscillating field of 0.0003 T under a variety of different *ac* frequencies. Pascal's constants were used to estimate the diamagnetic corrections, which were subtracted from the experimental susceptibilities to give the molar paramagnetic susceptibilities (χ_M).[38]

Specific heat studies: Specific heat measurements were carried out at temperatures down to 0.3 K by using a Quantum Design PPMS magnetometer equipped with a ^{3}He cryostat. The experiments were performed on thin pressed pellets (approximately 1 mg) of a polycrystalline sample, thermalized by approximately 0.2 mg of Apiezon N grease, whose contribution was subtracted using a phenomenological expression.

3.1.2. Synthesis

General Considerations: All experiments were performed under aerobic conditions and at ambient temperature. The chemicals (excluding $Ln(acac)_3$ starting materials) needed for the synthesis of the reported compounds were acquired from Alfa Aesar and Sigma Aldrich (reagent

grade). These chemicals were all used as received. Solvents (reagent grade) were also used as received. The $Ln(acac)_3 \cdot H_2O$ (Ln = Gd, Tb, Dy) starting materials were synthesized through the 1:3 reaction between $LnCl_3 \cdot 6H_2O$ and $(NH_4)(acac)$ in H_2O. The $(NH_4)(acac)$ salt was prepared stoichiometrically from the 1:1 reaction between NH_4OH and acetylacetone (acacH) in Et_2O.

Acenaphthenequinone dioxime ($acndH_2$). The organic ligand $acndH_2$ was prepared and characterized according to a literature method described elsewhere.[103,104] A solution of $NH_2OH \cdot HCl$ (7.51 g, 108 mmol) and $NaHCO_3$ (9.07 g, 108 mmol) in the minimum required volume of distilled water (~15 mL) was added to a suspension of acenaphthenequinone (8.93 g, 49 mmol) in MeOH (75 mL). The resulting suspension was stirred under reflux for 1.5 h, during which time a colour change from yellow to tan was observed. The resulting tan suspension was filtered, isolating the tan solid which was washed with cold MeOH (2 x 3 mL) and dried under vacuum. Elemental analysis (%) calculated for $acndH_2$: C 67.92, H 3.80, N 13.20; found: C 67.96, H 3.92, N 13.18. Selected IR data (ATR): ν = 2836 (b), 1709 (m), 1620 (w), 1605 (w), 1421 (w), 1367 (m), 1348 (m), 1277 (m), 1215 (w), 1181 (w), 1150 (w), 1109 (m), 1015 (s), 985 (s), 937 (m), 855 (s), 824 (m), 793 (w), 771 (s), 610 (w), 583 (w), 522 (m), 499 (w), 464 (w), 440 (w), 411 (w). ^{1}H NMR (DMSO-d^6, ppm): 12.36 (singlet, -C=NOH), 8.35-7.70 (doublet and double-of-doublets, Ar-H). The NMR data are in excellent agreement with those reported previously.[103,104]

$[Cu_6Gd_2(acnd)_6(acndH)_6(MeOH)_6]_n$ (4). To a yellow-green solution of $CuCl_2 \cdot 2H_2O$ (0.02 g, 0.1 mmol) in DMF (15 mL) was added a tan solid of the ligand $acndH_2$ (0.04 g, 0.2 mmol). The resulting dark green solution was stirred for 5 min, during which time NEt_3 (14 μL, 0.1 mmol) was added, resulting in a colour change of the solution from dark green to brown. Addition of solid $Gd(acac)_3 \cdot H_2O$ (0.10 g, 0.2 mmol) and further stirring for 20 min led to a brown suspension

which was filtered to remove the insoluble precipitates. The resulting brown filtrate was mixed with MeOH (15 mL) and left undisturbed at ambient temperature to afford after ~14 days orange plate-like crystals of **4**·2MeOH. The crystals were collected by filtration, washed with cold MeOH (2 x 2 mL) and dried in air. The yield was 20 %. Elemental analysis (%) calculated for the lattice solvent-free **4**: C 52.74, H 3.01, N 9.84; found: C 52.59, H 2.95, N 9.92. Selected IR data (ATR): ν = 1653 (m), 1592 (m), 1527 (w), 1485 (m), 1378 (m), 1324 (m), 1276 (m), 1199 (m), 1134 (m), 1004 (vs), 972 (s), 894 (m), 821 (m), 768 (s), 734 (m), 685 (m), 664 (m), 541 (m), 506 (m), 474 (m), 438 (m).

$[Cu_6Tb_2(acnd)_6(acndH)_6(MeOH)_6]_n$ (**5**). This complex was prepared in the exact same manner as complex **4**, but using $Tb(acac)_3{\cdot}H_2O$ (0.09 g, 0.2 mmol) in place of $Gd(acac)_3{\cdot}H_2O$. After 12 days, small orange crystals of **5** were collected by filtration, washed with cold MeOH (2 x 2 mL) and dried in air. The crystals were not suitable for X-ray diffraction studies but the identity of the product was precisely determined through elemental analyses and IR spectroscopic comparison with authentic samples from complexes **4** and **6**. The yield was 25 %. Elemental analysis (%) calculated for **5**: C 52.68, H 3.01, N 9.83; found: C 52.84, H 3.31, N 9.66. Selected IR data (ATR): ν = 1652 (m), 1590 (m), 1529 (w), 1485 (m), 1379 (m), 1319 (m), 1272 (m), 1198 (m), 1133 (m), 1002 (vs), 969 (s), 893 (m), 820 (m), 767 (s), 734 (m), 685 (m), 662 (m), 541 (m), 505 (m), 471 (m), 435 (m).

$[Cu_6Dy_2(acnd)_6(acndH)_6(MeOH)_2]_n$ (**6**). This complex was prepared in the exact same manner as complex **4**, but using $Dy(acac)_3{\cdot}H_2O$ (0.10 g, 0.2 mmol) in place of $Gd(acac)_3{\cdot}H_2O$. After 14 days, X-ray quality orange crystals of **6**·2MeOH·2DMF were collected by filtration, washed with cold MeOH (2 x 2 mL) and dried in air. The yield was 35 %. Elemental analysis (%) calculated for **6**·2DMF: C 52.51, H 2.90, N 10.47; found: C 52.64, H 2.96, N 10.26. Selected

IR data (ATR): ν = 1700 (m), 1649 (m), 1591 (m), 1532 (w), 1486 (m), 1381 (m), 1320 (m), 1258 (m), 1196 (m), 1133 (m), 1024 (vs), 1001 (s), 967 (s), 894 (m), 821 (m), 769 (s), 661 (mb), 543 (m), 510 (m), 472 (m), 435 (m).

3.1.3. Single-crystal X-ray Crystallography

Diffraction data for complexes **4** and **6** were collected at the Advanced Light Source, Lawrence Berkeley National Lab on beamline 11.3.1, using synchrotron radiation monochromated (silicon(111) to a wavelength of 0.7749(1) Å). Samples were mounted on MiTeGen® kapton loops and placed in a 100(2) K nitrogen cold stream provided by an Oxford Cryostream 700 Plus low temperature apparatus on the goniometer head of a Bruker D8 diffractometer equipped with a PHOTON100 CMOS detector operating in shutterless mode. An approximate full-sphere of data was collected using a combination of phi and omega scans with scan speeds of 1 second per 4 degrees for the phi scans, and 5 seconds per degree for the omega scans at $2\theta = 0$ and -45°, respectively.

The images obtained during the data collection for complexes **4** and **6** were processed with the software SAINT+,[92] and the absorption effects were corrected by the multi-scan method implemented in SADABS.[93] The structures were solved using the algorithm implemented in SHELXT,[94,95] and refined by successive full-matrix least-squares cycles on F^2 using the latest SHELXL-v.2014.[94,96] All the non-hydrogen atoms were successfully refined using anisotropic displacement parameters. Hydrogen atoms on aliphatic and aromatic carbon atoms were geometrically located using appropriate *HFIX* instructions in SHELXL, and included in subsequent refinement cycles in riding-motion approximation with isotropic thermal

displacement parameters (U_{iso}) fixed at 1.2 or 1.5 × U_{eq} of the relative atom. Most of the hydrogen atoms on the bound MeOH and lattice DMF molecules were found in the Fourier difference maps, their distances were fixed and allowed to refine with a riding model. Unfortunately, it has been impossible to grow crystals of suitable size for the acquisition of a complete X-ray data set for complex **5**. Unit cell parameters, structure solution and refinement details for complexes **4** and **6** are summarized in Table 3.1.

Table 3.1. Crystallographic data for complexes **4** and **6**.

Parameter	**4**	**6**
Formula	$C_{75.25}H_{52}Cu_3GdN_{12}O_{15.25}$	$C_{80.29}H_{62.19}Cu_3DyN_{14}O_{16.30}$
Fw / g mol^{-1}	1716.16	1839.99
Crystal type	Orange plate	Orange block
Crystal size / mm^3	0.05 x 0.03 x 0.01	0.04 x 0.02 x 0.01
Crystal system	Triclinic	Triclinic
Space group	$P\bar{1}$	$P\bar{1}$
a / Å	14.2405(6)	14.2319(9)
b / Å	16.3599(7)	17.6762(11)
c / Å	17.0630(6)	17.9066(11)
α / º	111.529(2)	61.904(3)
β / º	105.305(2)	67.059(4)
γ / º	102.670(3)	70.679(4)
Volume / Å^3	3337.9(2)	3598.9(4)
Z	2	2

Temperature / K	100(2)	100(2)
D_c / g cm^{-3}	1.708	1.695
μ / mm^{-1}	2.520	2.491
θ range (°)	2.343 – 29.061	2.431 – 29.032
Index ranges	$-17 \le h \le 16$	$-17 \le h \le 17$
	$-20 \le k \le 19$	$-22 \le k \le 22$
	$0 \le l \le 21$	$-22 \le l \le 22$
Collected reflections	13788	49636
Independent reflections	10389 (R_{int} = 0.0570)	14744 (R_{int} = 0.0866)
Final $R^{a,b}$ indices [$I>2\sigma(I)$]	$R1$ = 0.0487	$R1$ = 0.0470
	$wR2$ = 0.1026	$wR2$ = 0.0913
Final R indices (all data)	$R1$ = 0.0851	$R1$ = 0.0851
	$wR2$ = 0.1234	$wR2$ = 0.1222
$(\Delta\rho)_{max,min}$ / e Å^{-3}	1.882 and -1.685	1.038 and -1.108

[a] $R1 = \Sigma(||F_o| - |F_c||)/\Sigma|F_o|$. [b] $wR2 = [\Sigma[w(F_o^2 - F_c^2)^2]/\Sigma[w(F_o^2)^2]]^{1/2}$, $w = 1/[\sigma^2(F_o^2) + (ap)^2 + bp]$, where $p = [\max(F_o^2, 0) + 2F_c^2]/3$.

3.2. Results and Discussion

3.2.1. Synthetic Comments

The organic ligand acndH$_2$ was prepared using previously reported procedures.[103,104] The synthesis of the ligand is presented in Scheme 3.1.

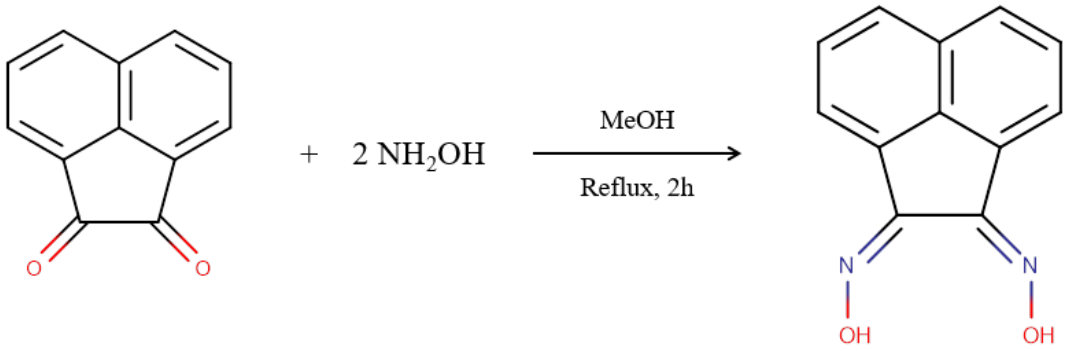

Scheme 3.1. Synthesis of acenaphthenequinone dioxime (acndH$_2$) from its precursor acenaphthenequinone. Synthesis as referenced from Ref. 103 and Ref. 104.

One of the key synthetic variables to the preparation of structurally novel and magnetically interesting Cu^{II}/Ln^{III} complexes is the choice of the organic chelating/bridging ligand. The latter should be able to satisfy the coordination needs of both metal ions by containing the preferable donor atoms and concurrently showing a bridging capacity which would allow for the aggregation of many metal ions into a polymetallic motif. To that end, it was decided to synthesize, characterize and use a new dioxime ligand in Cu^{II}/Ln^{III} (Ln = Gd, Dy, Tb) chemistry, as an extension of our previous interest in the use of pyridyl dioximes in 3*d*-, 4*f*- and 3*d*/4*f*-metal cluster chemistry.[105] The resulting molecule was acenaphthenequinone dioxime (acndH$_2$), which comprises four oximate-based donor atoms (2N + 2O atoms) and includes the bulky acenaphthene functionality, which could serve to enhance the solubility of coordination compounds in a variety of polar and nonpolar solvent media. The ligand acndH$_2$ has only been

used once in pure 3*d*-metal cluster chemistry for the synthesis of a family of $\{Zn_3\}$ linear clusters with luminescent properties.[103] The synthesis, structures and detailed magnetic studies on a new family of $\{Cu^{II}_6Ln^{III}_2\}$ clusters which extend their structures into covalently-linked 1-D chains are herein reported.

The general reaction between $CuCl_2{\cdot}2H_2O$, $Ln(acac)_3{\cdot}H_2O$, $acndH_2$ and NEt_3 in a 1:2:2:1 molar ratio, in a solvent mixture comprising DMF and MeOH, has afforded orange crystals of a new family of 1-D coordination polymers in yields of 20-35% depending on the employed 4*f*-metal ion. The $[Cu_6Ln_2(acnd)_6(acndH)_6(MeOH)_x]_n$ (Ln = Gd, **4**; Tb, **5**; Dy, **6**, and x = 6 or 2) polymeric compounds are built by repeating $\{Cu_6Ln_2\}$ cluster units, and their general formation is summarized in stoichiometric Equation 3.1.

$$6n\ Cu^{2+} + 2n\ Ln^{3+} + 12n\ acndH_2 + 18n\ NEt_3 + xn\ MeOH \xrightarrow{DMF/MeOH}$$

$$[Cu_6Ln_2(acnd)_6(acndH)_6(MeOH)_x]_n\ +\ 18n\ HNEt_3^+ \qquad \textbf{(Eqn 3.1)}$$

$$Ln = Gd\ (\mathbf{4});\ Tb\ (\mathbf{5});\ Dy\ (\mathbf{6})\ and\ x = 2\ or\ 6$$

Complexes **4**–**6** are stable under the prevailing basic conditions, and their identities are not dependent on either the nature of the base or the molar ratio of the reagents. However, their crystallinity and yields are heavily affected by the appropriate solvent mixture (DMF/MeOH) and the Cu^{II}:Ln^{III} molar ratio. In particular, the same reactions in only DMF or MeOH gave microcrystalline solids which were identified as $\{Cu_6Ln_2\}$ from IR spectroscopic studies and elemental analyses. Furthermore, similar reactions but in 1:1, 2:1, 3:1 and 1:3 Cu^{II}:Ln^{III} molar ratios gave crystals of **4**-**6** in 2-8 % yields. Although the Cl^- and $acac^-$ anions of the Cu^{II} and Ln^{III} starting materials, respectively, do not appear in the crystal structures of **4**-**6** (*vide infra*), the

analogous reactions with a variety of different metal precursors (i.e., $CuBr_2$, $Cu(NO_3)_2$, $Cu(ClO_4)_2$ and $LnCl_3$, $Ln(NO_3)_3$, $Ln(ClO_4)_3$, $Ln(O_2CMe)_3$) have afforded dark red insoluble precipitates which were impossible to crystallize and eventually determine their crystal structures.

3.2.2. Description of Structures

Complexes **4**-**6** are very similar to each other and differ only in the lanthanide ion present, the number of terminally bound MeOH groups, and the nature of the lattice solvate molecules. Complex **4** will be described in detail as a representative example but comparisons between the coordination numbers and geometries of the metal ions present in **4** and **6** will be carried out. The crystallographically established coordination modes of the $acnd^{2-}$ and $acndH^{-}$ ligands present in complexes **4** and **6** are shown in Scheme 3.2.

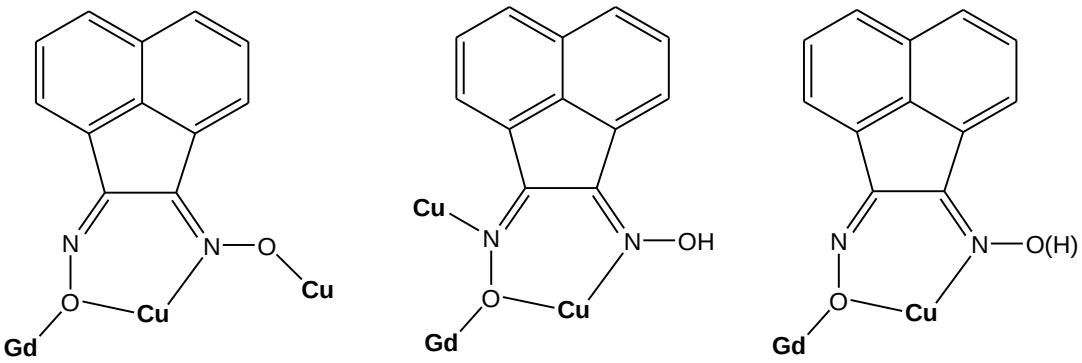

$\eta^2:\eta^1:\eta^1:\mu_3$ $\eta^2:\eta^1:\eta^1:\mu_3$ $\eta^2:\eta^1:\mu$

Scheme 3.2. Crystallographically established coordination modes of $acnd^{2-}$ and $acndH^{-}$ ligands present in complexes **4** and **6**.

The repeating unit of the 1-D polymeric complex **4** consists of $\{Cu_6Gd_2\}$ clusters that are intermolecularly linked to each other through the oximate groups of two $\eta^2:\eta^1:\eta^1:\mu_3$ acnd^{2-} ligands to give an overall *zigzag* chain along the *c* axis (Figure 3.1). The connection between adjacent $\{Cu_6Gd_2\}$ clusters within **4** is achieved through $\{Cu\text{-}(\mu\text{-}NO)_2\text{-}Cu\}$ units. The oximate bridges in the latter units are not planar, as previously seen in many dinuclear $\{Cu_2(\mu\text{-}NO)_2\}^{2+}$ complexes,[106] but instead 'twisted', with the Cu-N-O-Cu torsion angles being 83.3°.

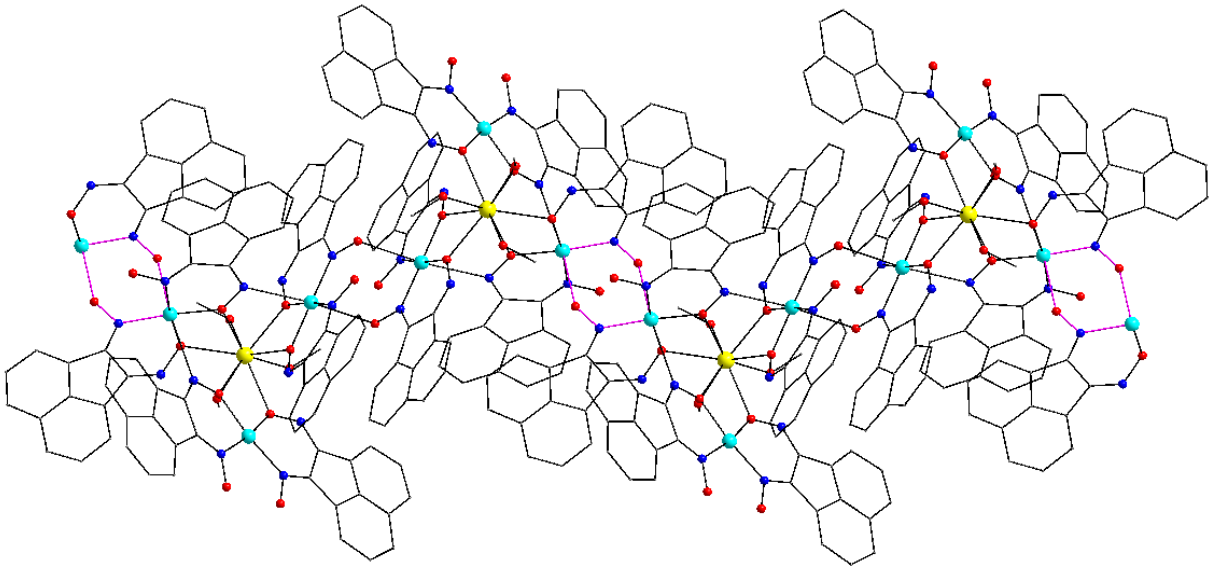

Figure 3.1. A small portion of the 1-D *zigzag* chain of **4** as extended along the *c* axis. H atoms are omitted for clarity. The purple bonds highlight the $\{Cu\text{-}(\mu\text{-}NO)_2\text{-}Cu\}$ units which serve to polymerize adjacent $\{Cu_6Gd_2\}$ clusters. Colour scheme: Gd^{III}, yellow; Cu^{II}, cyan; O, red; N, blue; C, grey.

The centrosymmetric $[Cu_6Gd_2(acnd)_6(acndH)_6(MeOH)_6]$ repeating unit of **4** comprises two symmetry-related $\{Cu_3Gd\}$ subunits, each with a distorted trigonal pyramidal topology (Figure 3.2, inset). The three Cu^{II} ions form the equatorial trigonal plane (Cu1···Cu2···Cu3 = 60.1°, Cu2···Cu3···Cu1 = 57.8° and Cu3···Cu1···Cu2 = 62.1°) while the apical position is occupied by the Gd^{III} ion which is displaced by 1.663 Å out of the Cu_3 best-mean-plane (Cu1···Gd1···Cu2 = 97.3°, Cu2···Gd1···Cu3 = 102.6° and Cu3···Gd1···Cu1 = 99.8°). Each Cu^{II} ion is linked to the Gd^{III} apex by two monoatomic $-NO^-$ oximate bridges (O1/O3, O5/O7 and O9/O11) of three $\eta^2:\eta^1:\eta^1:\mu_3$ $acnd^{2-}$ and three $\eta^2:\eta^1:\mu$ $acndH^-$ ligands (Scheme 3.2). The Cu^{II}-O-Gd^{III} angles span the range 107.4(2)-110.3(2)°. The three Cu^{II} ions within the triangular plane are bridged by a diatomic $-NO^-$ oximate group from three different $\eta^2:\eta^1:\eta^1:\mu_3$ $acnd^{2-}$ ligands. The Cu-N distances within the three Cu-N-O-Cu linkages are noticeably large (Cu1-N11 = 2.825(6) Å, Cu2-N3 = 2.682(5) Å and Cu3-N7 = 2.951(5) Å) and can be considered as very weakly bonding, whereas the respective Cu-N-O-Cu torsion angles span the range 173.5-178.0°. Therefore, the coordination geometry of all Cu^{II} ions is well described as Jahn-Teller distorted octahedral with four short bonds formed by two oximate N and two oximate O atoms, and a remaining axial coordination site occupied by an oximate O atom from a neighboring $\{Cu_6Gd_2\}_n$ chain. These Cu-O distances (Cu1-O2# = 2.610(5) Å, Cu2-O6# = 2.765(4) Å and Cu3-O12# = 2.855(5) Å, where "#" is the general symbol used for the atoms in adjacent chains) are significantly longer than the equatorial ones and they serve to connect adjacent chains into weakly coupled 2-D sheets (Figure 3.3).

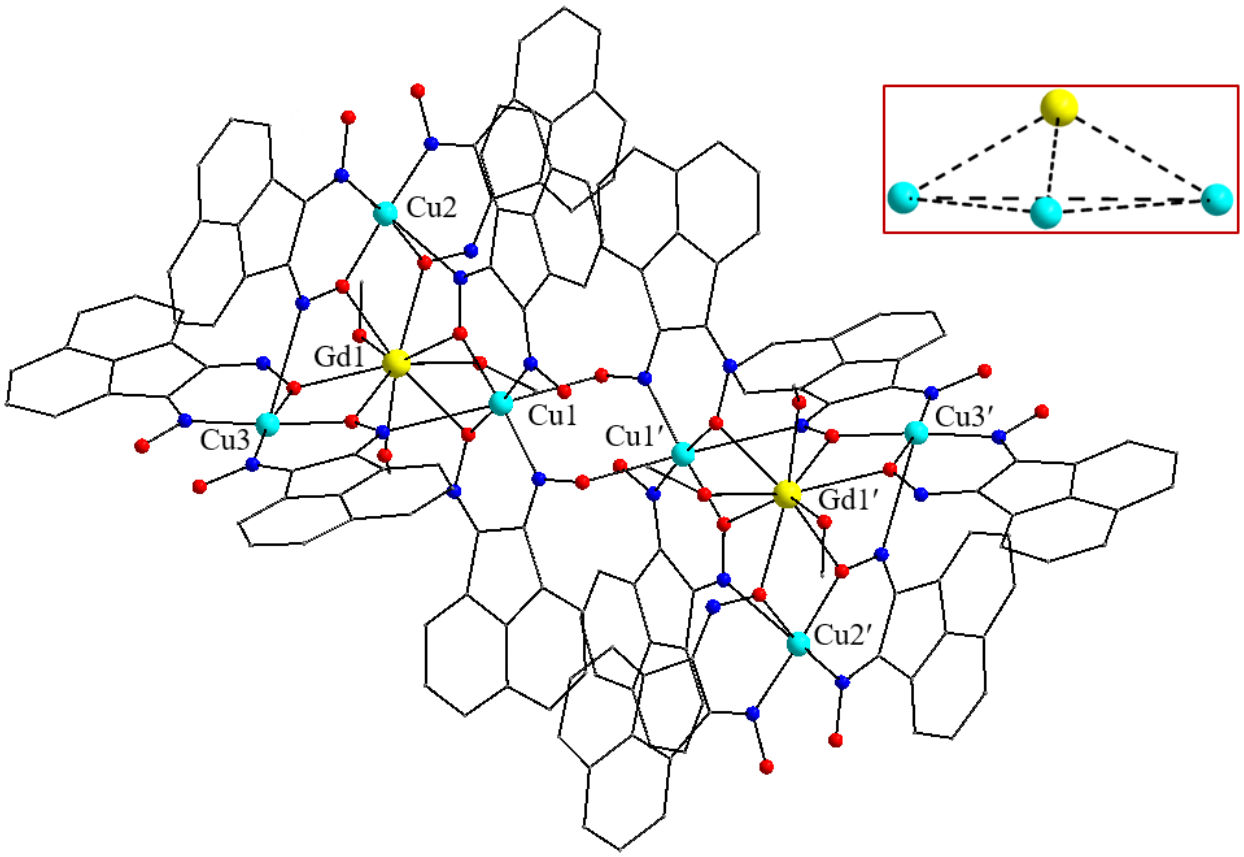

Figure 3.2. Partially labeled representation of the centrosymmetric $\{Cu_6Gd_2\}$ repeating unit of **4**. H atoms are omitted for clarity. Colour scheme: Gd^{III}, yellow; Cu^{II}, cyan; O, red; N, blue; C, grey. Inset: The trigonal pyramidal topology of the $\{Cu_3Gd\}$ asymmetric unit. Symmetry code: ′ = 1–x, 1–y, 2–z.

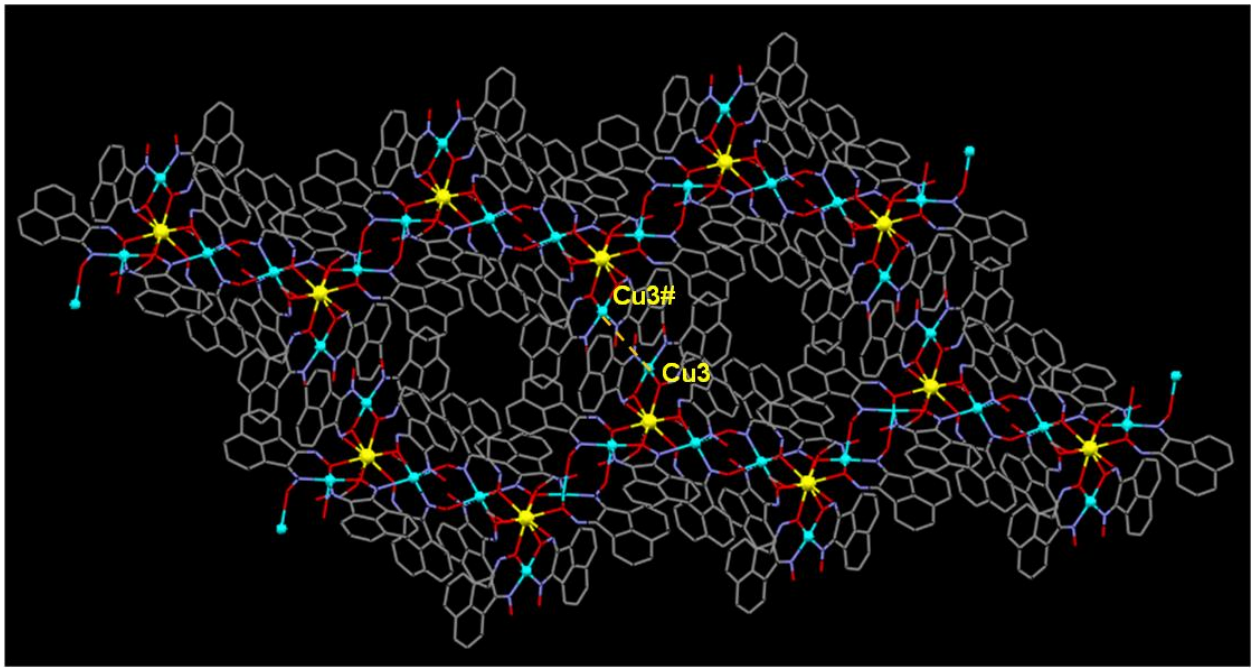

Figure 3.3. A small portion of the 2-D sheets formed by the weak interactions (dashed line) of Cu^{II} ions in **4** with oximate O atoms from adjacent chains.

The two {Cu_3Gd} subunits are intramolecularly connected through two μ-NO^- bridges from two different $\eta^2:\eta^1:\eta^1:\mu_3$ $acnd^{2-}$ ligands (Scheme 3.1); the two Cu1-N2-O2-Cu1′ torsion angles are 94.1°. Thus, the complete core of the repeating unit of **4** is $[Cu_6Gd_2(\mu_3\text{-}NO)_6(\mu\text{-}NO)_8]^{4+}$ (Figure 3.4). All dioximate ligands in complexes **4** and **6** act as bidentate chelates to a Cu^{II} ion, utilizing the O and N atoms from different oximate moieties to form stable six-member chelating rings, while the deprotonated O atoms act as linkers to additional Ln^{III} and Cu^{II} ions.

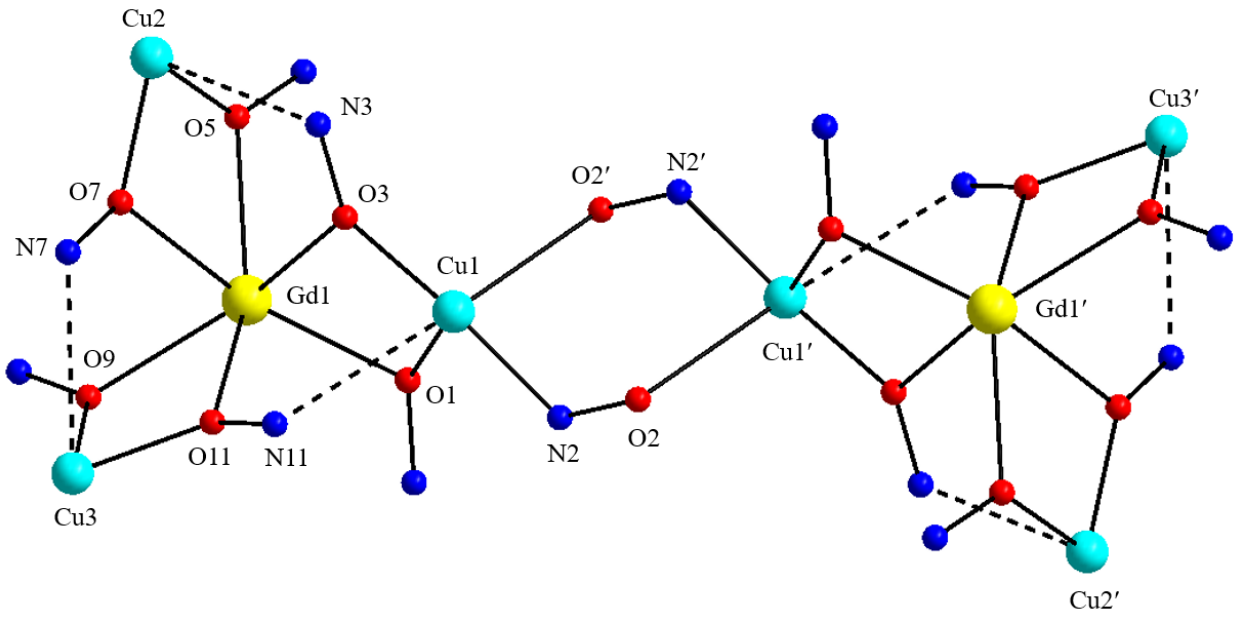

Figure 3.4. The complete $[Cu_6Gd_2(\mu_3\text{-}NO)_6(\mu\text{-}NO)_8]^{4+}$ core of **4**. The dashed lines indicate the weak Cu-N bonding distances. Colour scheme: Gd^{III}, yellow; Cu^{II}, cyan; O, red; N, blue.

The lanthanide ions in complexes **4** and **6** are nine- and seven-coordinate, respectively, with different number of terminal MeOH molecules completing the coordination spheres. To estimate the closer coordination polyhedra defined by the donor atoms around Gd1 and Dy1 in the asymmetric units of **4** and **6**, respectively, a comparison of the experimental structural data with the theoretical data for the most common polyhedral structures with different number of vertices was performed by means of the program SHAPE.[107] Following the proposal by Avnir and co-workers[108] to consider symmetry and polyhedral shape as continuous properties that can be quantified from structural data, Alvarez and co-workers have applied these concepts and the associated methodology to the stereochemical analysis of very large sets of molecular structures, including systems with 7-9 vertex polyhedra.[109] The so-called Continuous Shape Measures

(CShM) approach allows one to numerically evaluate by how much a particular structure deviates from an ideal shape.[110] The best fit was obtained for the spherical tricapped trigonal prism (Gd1; Figure 3.5, left) and capped octahedron (Dy1, Figure 3.5, right) with CShM values of 0.77 and 1.18, respectively (Tables 3.2 and 3.3). Values of CShM between 0.1 and 3 usually correspond to a not negligible, but still small, distortion from ideal geometry.[98] Finally, the Ln ions present in **4** and **6** are bound exclusively to O atoms from the dioximate and MeOH groups, further highlighting the oxophilicity of 4*f*-metal ions. The Ln-O bond distances in **4** and **6** fall into the expected range for similar compounds and take shorter values as moving from **4** to **6**, in agreement with the well-known lanthanide contraction effect.

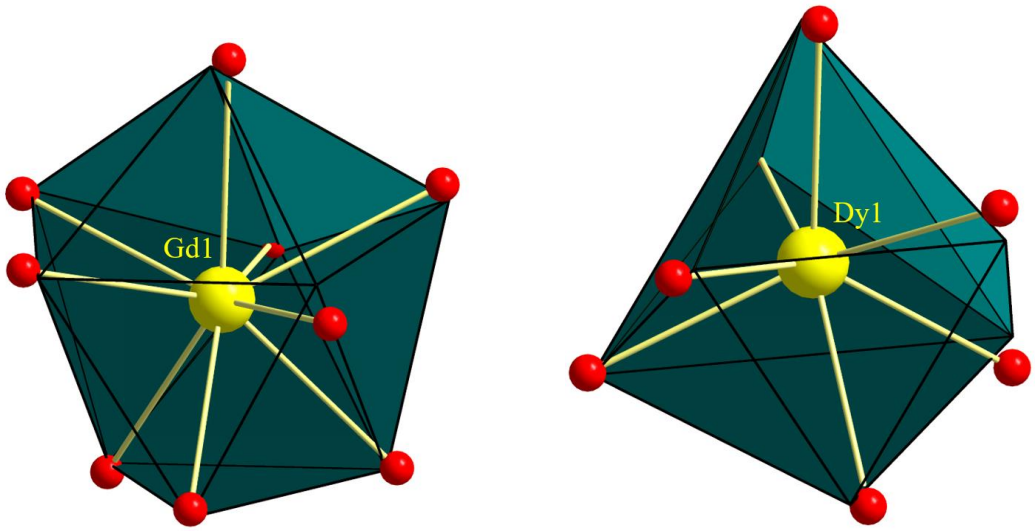

Figure 3.5. Spherical tricapped trigonal prismatic (left) and capped octahedral (right) coordination geometries of Gd1 and Dy1 atoms in the structures of **4** and **6**, respectively. Points connected by the black thin lines define the vertices of the ideal polyhedra.

Table 3.2. SHAPE measures of the 9-coordinate Gd1 coordination polyhedron in complex **4**.[a]

Polyhedron[b]	Gd1
EP-9	36.24
OPY-9	22.44
HBPY-9	19.47
JTC-9	14.31
JCCU-9	10.49
CCU-9	9.06
JCSAPR-9	2.18
CSAPR-9	1.00
JTCTPR-9	2.45
TCTPR-9	**0.77**
JTDIC-9	11.75
HH-9	12.36
MFF-9	1.51

[a] The values in boldface indicate the closest polyhedron according to the Continuous Shape Measures (CShM). [b] Abbreviations: EP-9, enneagon; OPY-9, octagonal pyramid; HBPY-9, heptagonal bipyramid; JTC-9, Johnson triangular cupola; JCCU-9, capped cube; CCU-9, spherical-relaxed capped cube; JCSAPR-9, capped square antiprism; CSAPR-9, spherical capped square antiprism; JTCTPY-9, tricapped trigonal prism; **TCTPR-9, spherical tricapped trigonal prism**; JTDIC-9, tridiminished icosahedron; HH-9, hula-hoop; MFF-9, muffin.

Table 3.3. SHAPE measures of the 7-coordinate Dy1 coordination polyhedron in complex **6**.[a]

Polyhedron[b]	Dy1
HP-7	38.53
HPY-7	16.17
PBPY-7	9.73
COC-7	**1.18**
CTPR-7	3.16
JPBPY-7	13.03
JETPY-7	18.96

[a] The values in boldface indicate the closest polyhedron according to the Continuous Shape Measures (CShM). [b] Abbreviations: HP-7, heptagon; HPY-7, hexagonal pyramid; PBPY-7, pentagonal bipyramid; **COC-7, capped octahedron**; CTPR-7, capped trigonal prism; JPBPY-7, Johnson pentagonal bipyramid; JETPY-7, Johnson elongated triangular pyramid.

Complexes **4-6** join a handful of previously reported $\{Cu_6Ln_2\}$ clusters,[111] and they are the first structurally characterized $\{Cu_6Ln_2\}$ compounds with a 1-D polymeric topology. In addition, the $[Cu_6Ln_2(\mu_3\text{-}NO)_6(\mu\text{-}NO)_8]^{4+}$ core is reported for a first time in heterometallic cluster chemistry and this urged us to investigate in detail the magnetic and magnetocaloric properties of **4**-**6**.

3.2.3. Solid-State Magnetic Susceptibility Studies

The covalently linked {Cu_3Ln} units of complexes **4**–**6** are extended into {Cu_6Ln_2} clusters and subsequently to 1-D polymeric chains. As a result, the interpretation of their magnetic properties in terms of fitting the magnetic susceptibility data and rationalizing the ground state spin values using a simple 'spin-up'/'spin-down' vector scheme was not straightforward and when attempted (in the case of isotropic complex **4**) it led to unreasonable results. Unfortunately, it was not possible to isolate crystals of the diamagnetic Y- or La-analogues of **4**–**6**, and therefore the nature and magnitude of the magnetic exchange interactions between the Cu^{II} ions remain unclear. However, it is well known that the $Cu^{II}\cdots Cu^{II}$ magnetic exchange interactions, promoted exclusively by diatomic NO oximate bridges, are antiferromagnetic in nature and the strength of the interactions depends on the Cu-N-O-Cu torsion angles.[106]

Solid-state direct current (*dc*) magnetic susceptibility (χ_M) data on dried and analytically pure and crystalline samples of **4**, **5** and **6**·2DMF were collected in the temperature range 2.0-300 K in an applied field of 0.1 T, and are plotted as $\chi_M T$ versus T plots in Figure 3.6. The experimental $\chi_M T$ values at 300 K for all complexes are in excellent agreement with the theoretical ones (18.00 cm^3 K mol^{-1} for **4**; 25.89 cm^3 K mol^{-1} for **5**; 30.59 cm^3 K mol^{-1} for **6**) for 6 Cu^{II} and 2 Ln^{III} non-interacting ions. For complexes **4** and **5**, the $\chi_M T$ product steadily increases with decreasing temperature to reach the values of 29.90 and 36.27 cm^3 K mol^{-1}, respectively, at 7 K. The magnetic behaviour of **4** and **5** is consistent with the presence of predominant ferromagnetic exchange interactions between the metal ions and a relatively strong coupling between them, as indicated by the sharp increase of the $\chi_M T$ product in the 300-5 K region. For complex **6**, the magnetic response is slightly different than that of **4** and **5**; the $\chi_M T$ product remains almost

constant at a value of ~35.2 cm^3 K mol^{-1} from 300 K to ~35 K, and then steadily decreases to a value of 32.72 cm^3 K mol^{-1} at 20 K. This behaviour indicates either the presence of predominant antiferromagnetic exchange interactions between the metal centers or depopulation of the excited m_J states of the Dy^{III} atoms,[66,72,112] or both. Below 20 K though, the $\chi_M T$ product of **6** starts increasing with decreasing temperature to reach a maximum value of 33.55 cm^3 K mol^{-1} at 6 K. This increase may be attributed to some weak ferromagnetic exchange interactions between the Cu^{II} and Dy^{III} ions in **6**. The low temperature (T < 6-7 K) decrease of the $\chi_M T$ products of **4**–**6** is likely due to the presence of weak antiferromagnetic exchange interactions and magnetic anisotropy. Thus, the magnetic susceptibility data of complexes **4**–**6** are suggestive of ferromagnetically-coupled systems albeit the presence of some antiferromagnetic contribution from the Cu-N-O-Cu pathways should not be ruled out. Anticipating the analysis of the heat capacity data for complex **4**, its magnetic properties were interpreted as the result of the ferromagnetic coupling between each Gd^{III} (S_{Gd} = 7/2) ion with the peripheral Cu^{II} (S_{Cu} = 1/2) ions, thus leading to two S = 5 units per $\{Cu_6Gd_2\}$ molecule, which are weakly and antiferromagnetically intercoupled. Assuming g = 2.0, the susceptibility of two S = 5 units with negligible interaction between them should be equal to 30 cm^3 K mol^{-1}, which nicely agrees with the low-temperature value reached by the experimental $\chi_M T$ product.

The magnetic coupling between Cu^{II} and Gd^{III} ions is frequently found to be ferromagnetic for a wide range of Cu^{II}-O-Gd^{III} angles.[36,84,113] In addition, the sign and magnitude of the J_{ij} coupling constant depends on various structural and physical parameters, such as the degree of planarity of the bridging core,[114] the hinge angle,[115] the orthogonality of the *d*- and *f*-orbitals,[36] and the efficient electron transfer from the singly occupied 3*d* copper(II) orbital to an empty 5*d* gadolinium(III) orbital.[36,114] Ferromagnetic coupling between Cu^{II} and either Tb^{III} or Dy^{III} ions is

also of precedence in 3*d*/4*f*-metal cluster chemistry but this is more rarely observed due to the concurrent presence of first-order angular momentum.[116]

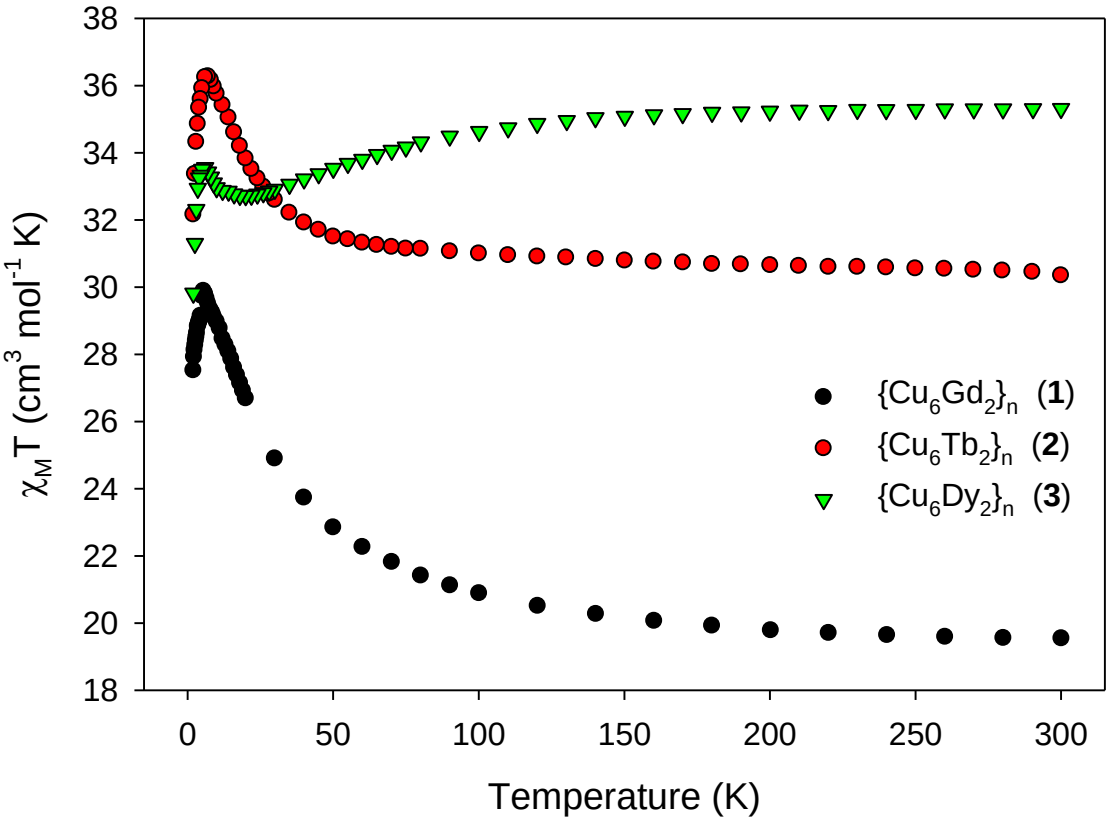

Figure 3.6. $\chi_M T$ versus T plots for complexes **4**–**6** in an applied *dc* field of 0.1 T.

Magnetization (*M*) versus field (*H*) studies were also performed for complexes **4**–**6** (Figure 3.7) at different low temperatures and magnetic fields. The data for the $\{Cu_6Gd_2\}$ compound shows a very fast increase of magnetization with increasing field, resulting in a fast saturation of *M* at a value of ~20 $N\mu_B$, which is indicative of the presence of dominant ferromagnetic exchange interactions between the metal ions.[36,84,113] The magnetization at saturation agrees nicely with two weakly coupled $\{Cu_3Gd\}$ units, each possessing an $S = 5$ spin state, as anticipated from the

$\chi_M T$ data. The *M* versus *H* plots for **5** and **6** between 1.9 and 5 K are not superimposed on a single master curve, thus indicating the presence of magnetic anisotropy and/or the population of low-lying excited states and the effect from some weak antiferromagnetic components between the metal ions.[36,66,72,112,113,115]

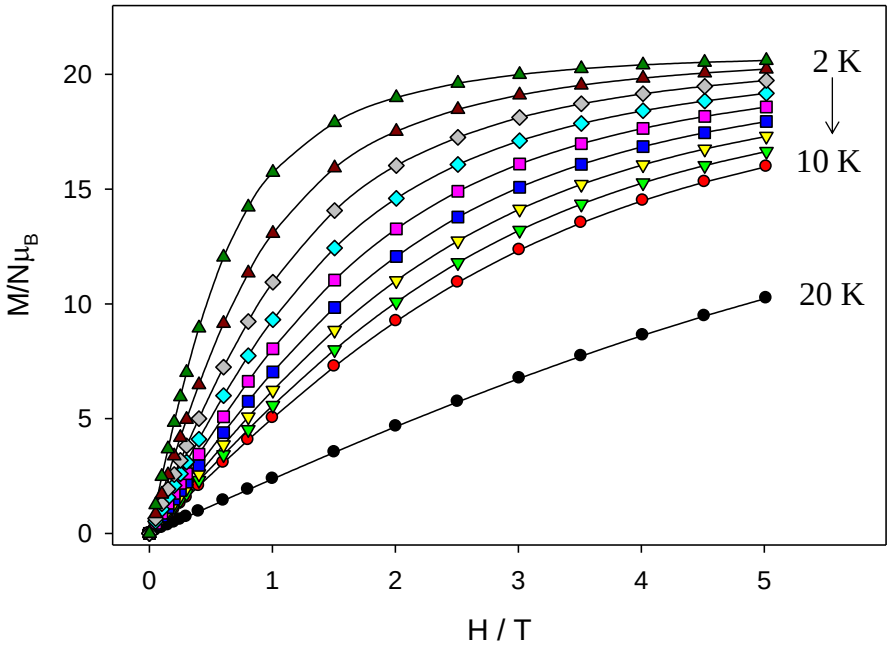

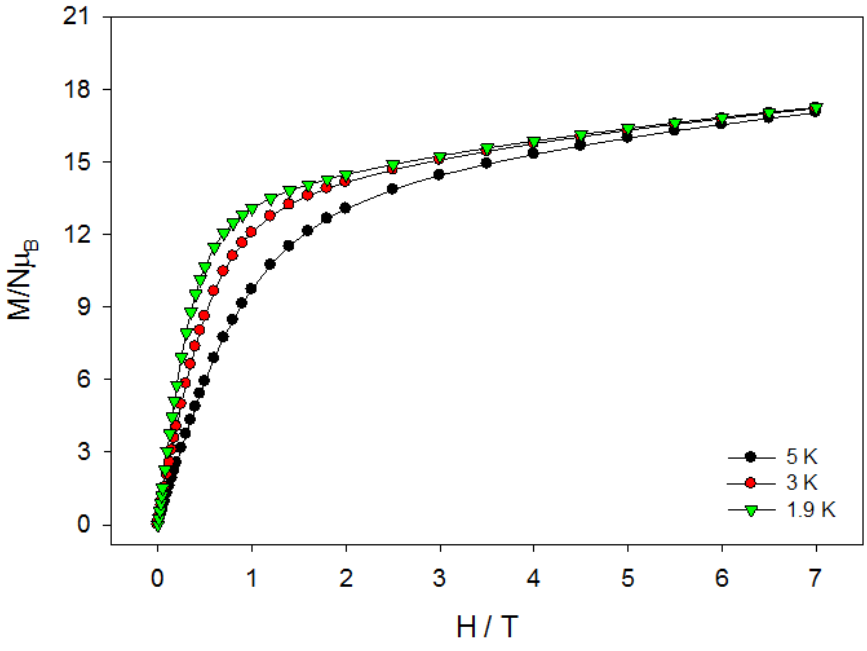

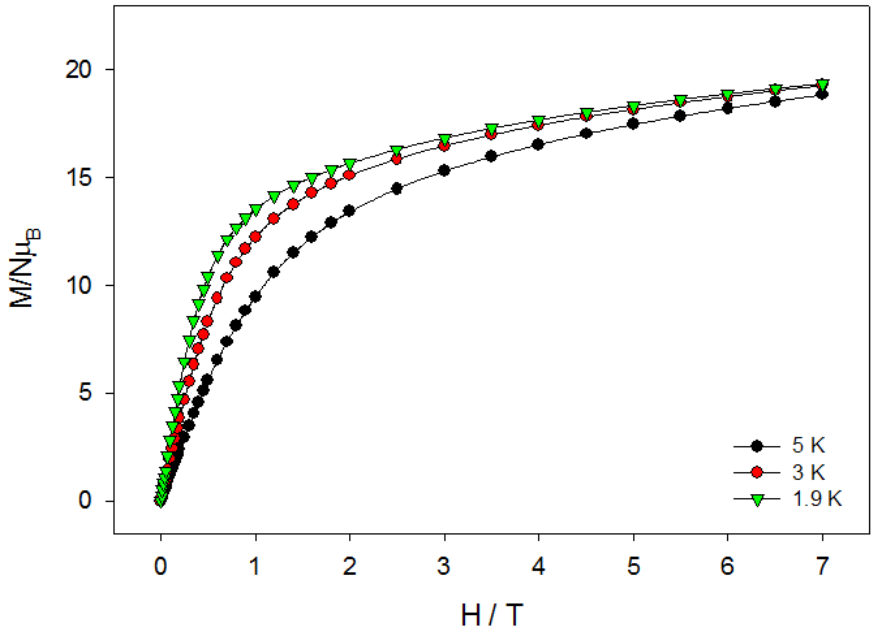

Figure 3.7. *M* versus *H* plots for complexes **4** (top), **5** (middle), and **6** (bottom) carried out at different temperatures, as labeled. The solid lines are guides for the eye.

Alternating current (*ac*) magnetic susceptibility studies have also been carried out in order to investigate the magnetization dynamics of the anisotropic complexes **5** and **6** in the absence of an external *dc* magnetic field. Complex **6** did not show any χ_M'' signals either in the absence or the presence of external *dc* field. This indicates the presence of a very fast relaxation of magnetization, presumably derived from the non-ideal coordination environment (ligand field) around the Dy^{III} atoms. This could be the key reason for the small axiality of $\{Cu_6Dy_2\}$, which is, in turn, reflected in a large tunneling gap of the ground Ising doublet.[66,72] In contrast to complex **6**, the study of the magnetic dynamics of **5** revealed the presence of frequency-dependent in-phase, χ_M', and out-of-phase, χ_M'', signals at temperatures below ~6 K (Figure 3.8); this behavior is indicative of the slow magnetization relaxation of an SMM with a small energy

barrier for the magnetization reversal. The χ_M'' signal reaches the value of 2.7 cm^3 mol^{-1} at 320 Hz and 1.9 K but is still increasing at this point and so the peak maximum is not visible within the temperature limit of our SQUID magnetometer.

The *ac* susceptibility of **5** as a function of the frequency at different temperatures has also been explored in order to follow, if possible, the relaxation process. Unfortunately, no difference was observed in the location of the out-of-phase peak maxima, and therefore it was decided to conduct *ac* studies in the presence of external *dc* fields of different strengths at 1.9 K. These measurements help to suppress a possible fast ground state quantum tunneling of the magnetization and consequently shift the χ_M'' tails of signals to higher temperatures where the peak maxima could be observed and used for the determination of the relaxation time (τ) and the effective energy barrier (U_{eff}) for the magnetization reversal. To our disappointment, it was not feasible to observe any χ_M'' maxima at 1.9 K and 1000 Hz within the *dc* field range of 0.01-1.0 T (Figure 3.9). This suggests that the quantum tunneling of magnetization in complex $\{Cu_6Tb_2\}_n$ is not an efficient relaxation pathway above 1.9 K.[116]

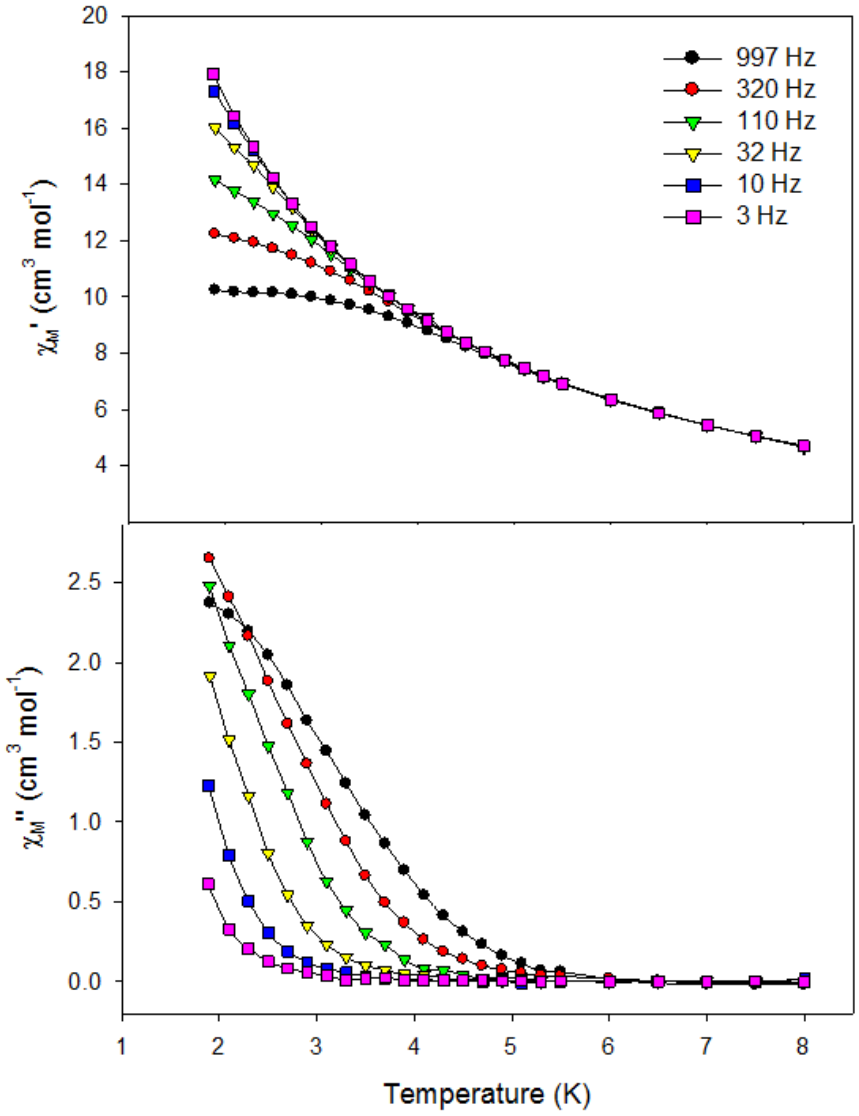

Figure 3.8. Temperature dependence of the in-phase (top) and out-of-phase (bottom) *ac* susceptibility signals of **5** in a 3 G field oscillating at the indicated frequencies.

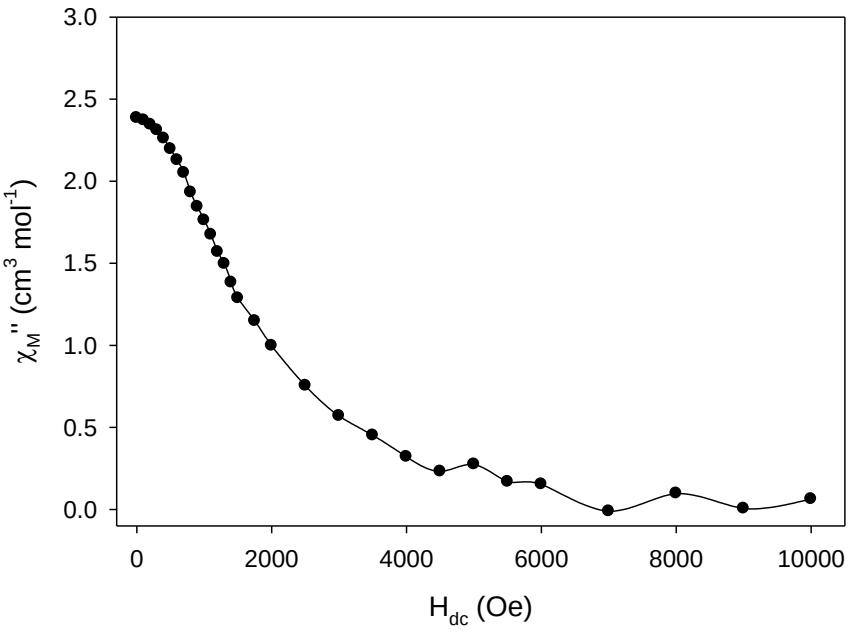

Figure 3.9. *dc*-field dependence of the out-of-phase *ac* susceptibility signals of **5** at 1.9 K and a frequency of 1000 Hz.

An alternative way to estimate the energy barrier and relaxation time when the peak maxima cannot be determined is through the employment of the below Equation 3.2 developed by Bartolomé and coworkers.[117]

$$\ln(\chi''/\chi') = \ln(\omega\tau_o) + E_a/k_\beta T \qquad \textbf{(Eqn. 3.2)}$$

Considering a single relaxation process, the least-squares fits of the experimental data (Figure 3.10) gave an energy barrier of ~11 K and a relaxation time of 10^{-8} s, which is consistent with the expected τ_0 values for a fast relaxing molecular nanomagnet.

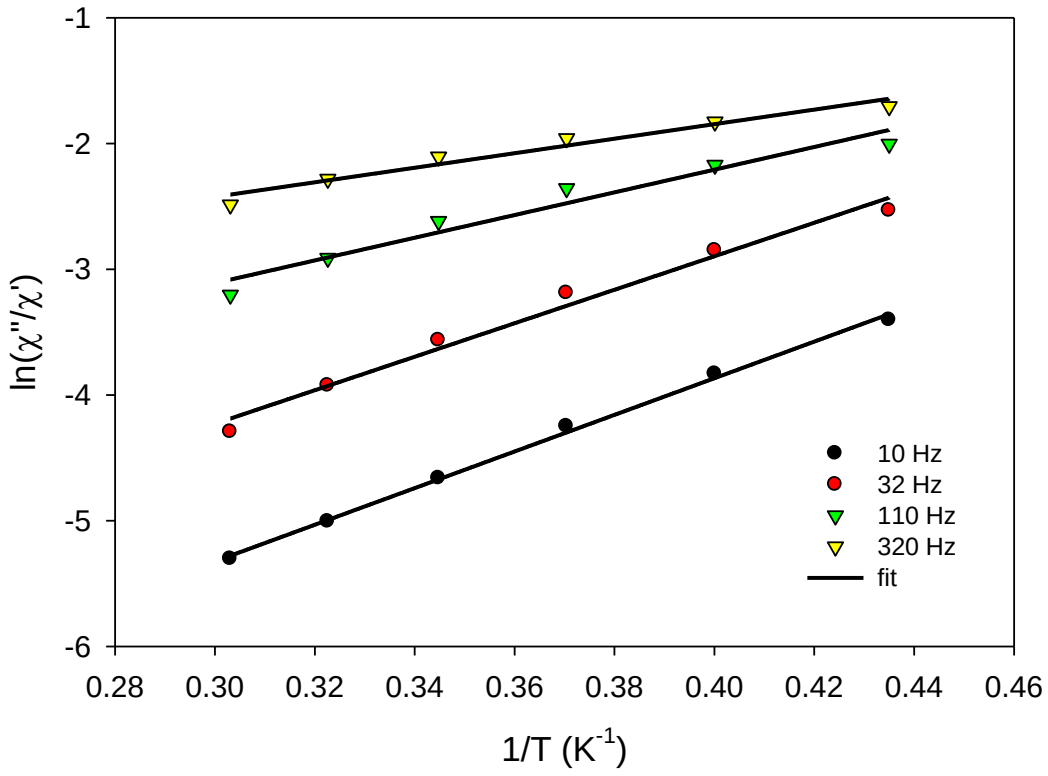

Figure 3.10. Plots of ln(χ''/χ') versus 1/T for **5** at different *ac* frequencies; the solid lines are the best-fit curves.

3.2.4. Magnetocaloric Properties

Figure 3.11 shows the experimental heat capacity, collected from 30 K down to 0.3 K for several applied fields. A non-magnetic contribution is seen to dominate the heat capacity above 5 K. This contribution was attributed to the lattice heat capacity, C_{latt}, and it was modeled with the Debye function for characteristic temperature, Θ_D = 21.2 K (dotted line). At low temperatures, the heat capacity strongly depends on the applied fields. The magnetic contribution to the heat capacity, C_m, consists of a Schottky-like anomaly that shifts to higher temperatures on increasing the applied field. The Schottky-like anomaly was associated to the splitting of two S = 5 net spin-

multiplets per molecule, which results from the ferromagnetic coupling between each Gd^{III} ion with the three peripheral Cu^{II} ions. Note that the height, C_{max}, of the Schottky anomaly is sensitive to the value of the spins involved. For instance, a fully ferromagnetic net spin of $S = 10$ per molecule should give $C_{max}/R = 1.0$, whereas the sum of six non-interacting Cu^{II} spins and two non-interacting Gd^{III} spins per molecule should provide $C_{max}/R = 4.0$, both in clear disagreement with the experimental data. In the case of two non-interacting $S = 5$ spin-multiplets, $C_{max}/R = 1.9$ and the calculated Schottky anomalies (solid lines) nicely describe the magnetic contribution to the experimental heat capacity for $\mu_0 H \geq 1$ T. The fact that a field of 1 T is already sufficient for fully decoupling the $S = 5$ spin-multiplets implies a weak coupling between these units, which is likely antiferromagnetic, in agreement with the susceptibility data. Furthermore, from the heat capacity data, the entropy: $S(T,H) = \int_0^T \frac{C(T,H)}{T} dT$ which is shown in Figure 3.11, together with the lattice entropy, calculated from C_{latt}, were calculated As expected, the magnetic contribution of the zero-field entropy tends to the value corresponding to two uncorrelated $S = 5$ spin units per mole, i.e., $2R\ln(2S+1) = 2R\ln(2 \times 5 + 1) = 4.8R$.

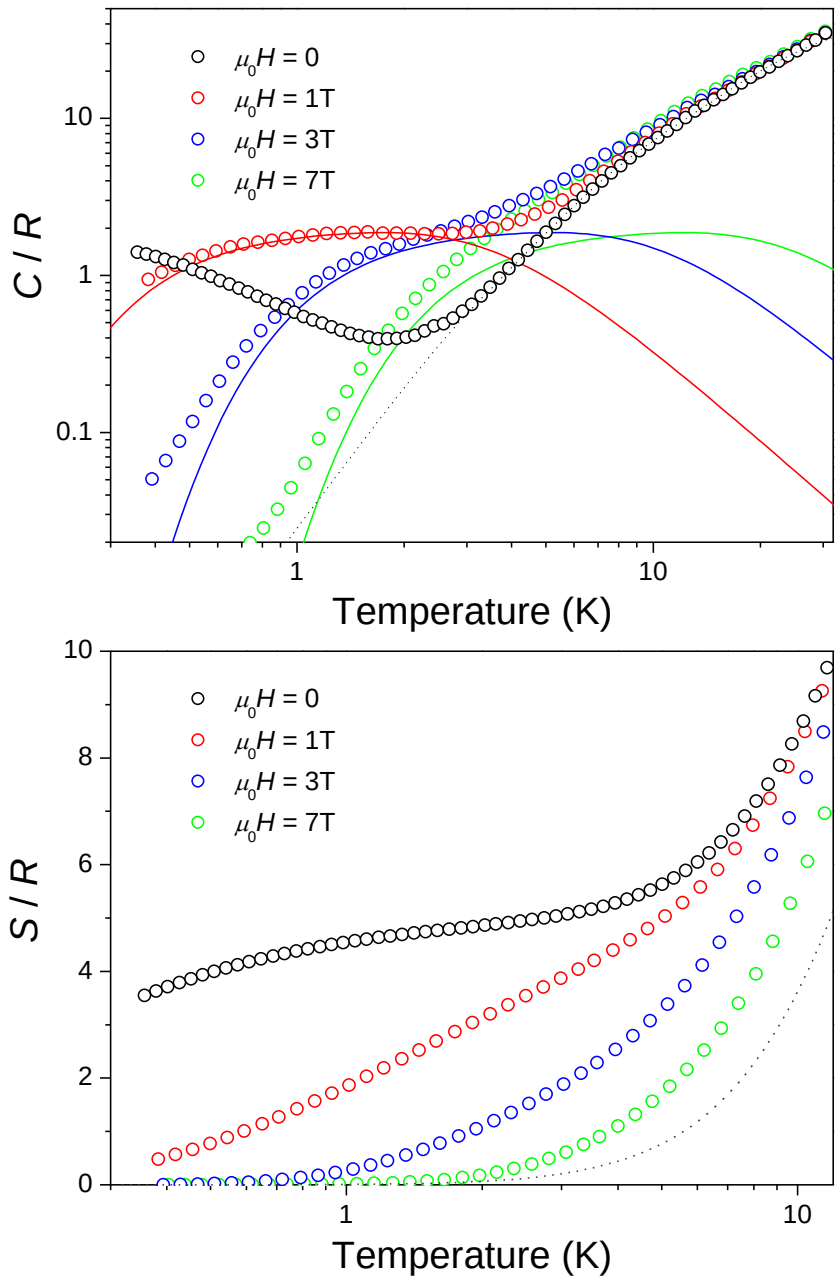

Figure 3.11. (top) Molar heat capacity for **4** as a function of temperature for the indicated applied fields. The solid lines correspond to the Schottky anomalies calculated for two non-interacting $S = 5$ systems. The dashed line is the lattice contribution, C_{latt}. (bottom) Temperature dependence of the total entropy of **4** for several applied fields, as obtained from the integration of the heat capacity data. The dashed line is the lattice contribution, C_{latt}.

Finally, the magnetocaloric effect for complex **4** was evaluated. From the entropy curves, the magnetic entropy change, $\Delta S_m(T,\Delta H)$, and adiabatic temperature change, $\Delta T_{ad}(T,\Delta H)$, were obtained, which resulted from the magnetic field change, $\Delta H = H_f - H_i$ (Figure 3.12). Likewise, the magnetic entropy change was also obtained from the magnetization data (Figure 3.7, top), by using the Maxwell-type Equation 3.3.

$$\Delta S_m(T,\Delta H) = \int_{H_i}^{H_f} \left[\frac{\partial M(T,H)}{\partial T}\right]_H dH \qquad \textbf{(Eqn. 3.3)}$$

The two sets of data for the magnetic entropy change, independently derived either from heat capacity or magnetization, respectively, were in good agreement to each other. Note that the estimation of the non-magnetic lattice contribution to the heat capacity is irrelevant since it cancels out when dealing with differences in total entropies. For $\mu_0\Delta H$ = 1 T, $-\Delta S_m(T,1\text{T})$ reaches 7.9 J kg^{-1} K^{-1} at T = 0.5 K, whereas $\Delta T_{ad}(T,1\text{T})$ reaches 3.2 K at T = 1.0 K. The field dependence of the MCE is not linear on increasing ΔH. As can be seen in Figure 3.12, for the maximum applied field change, i.e., $\mu_0\Delta H$ = 7 T, $-\Delta S_m(T,7\text{T})$ reaches 11.8 J kg^{-1} K^{-1} at T = 1.6 K, whereas $\Delta T_{ad}(T,7\text{T})$ reaches 7.9 K at T = 0.8 K. These values turned out to be not excitingly large when compared with those obtained from other coordination compounds based on Cu^{II} and Gd^{III} ions.[85,87,118] One of the reasons is that complex **4** has a relatively large molecular mass (or a small metal/ligand mass ratio), hence not favouring a large MCE since the nonmagnetic ligands contribute passively.[119] An additional reason is that, as already noted, magnetic fields as large as 7 T are not sufficient for decoupling the Cu^{II} and Gd^{III} spins, and thus they stabilize into two net S = 5 spins per $\{Cu_6Gd_2\}$ molecule at low temperatures. Therefore, $-\Delta S_m$ has to be limited by the available entropy, which reduces to $2\times R\ln(2\times5 + 1) = 4.8R$ = 11.8 J kg^{-1} K^{-1}. This value is

reached experimentally for $\mu_0\Delta H$ = 7 T, thus corroborating that the antiferromagnetic coupling between the S = 5 spins has to be very weak, and so is their magnetic anisotropy.

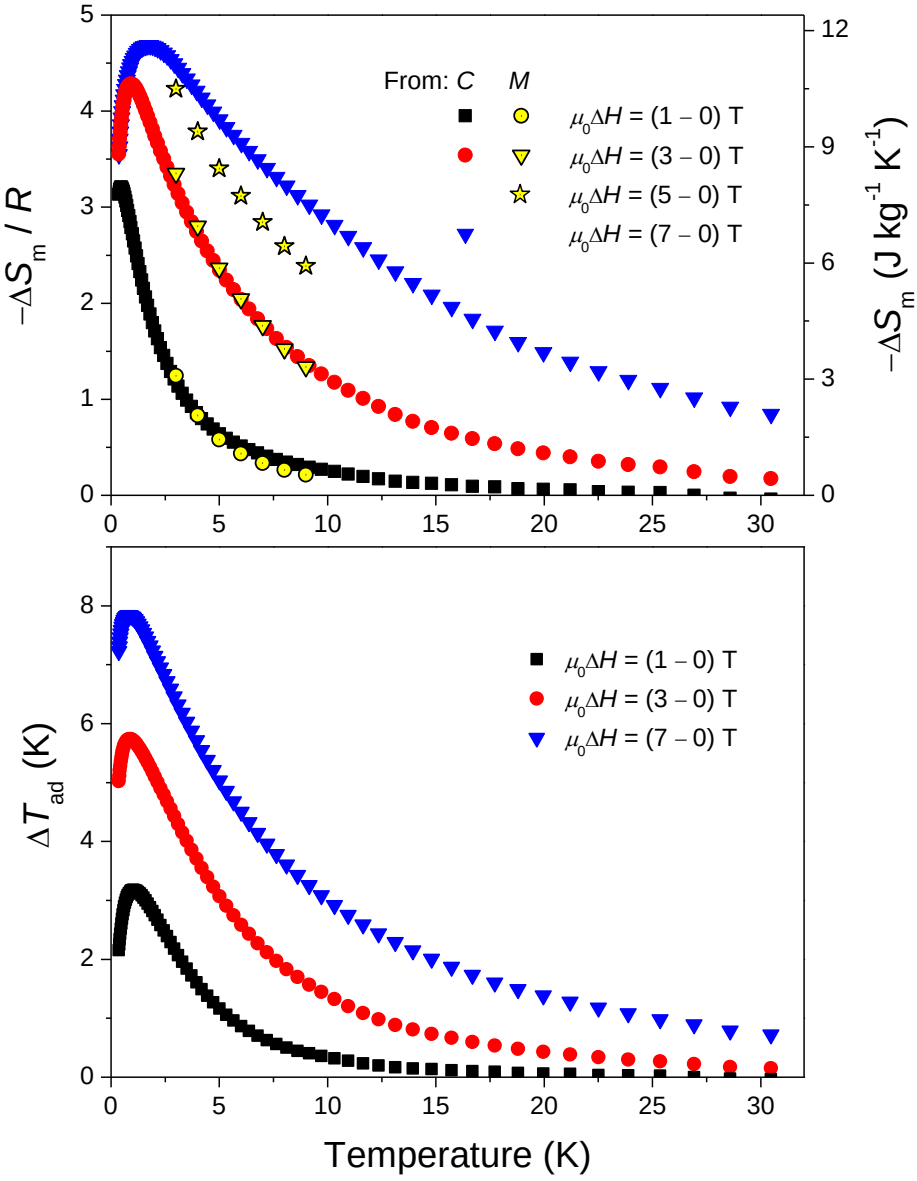

Figure 3.12. (top) Magnetic entropy change, as obtained from heat capacity and magnetization data, and (bottom) adiabatic temperature change for complex **4**, as obtained from heat capacity data, for the indicated applied field changes.

3.3. Conclusions and Perspectives

In conclusion, it was shown that the ligand acndH_2 can be successfully employed in heterometallic 3*d*/4*f*-metal cluster chemistry, yielding new cluster compounds that possess interesting structural motifs and magnetic properties. Complexes **4** and **5** were clearly shown to possess ferromagnetic exchange interactions between the paramagnetic metal ions. Furthermore, complex **4** was shown to act as a molecular magnetic refrigerant, while complex **5** exhibited SMM behaviour. The ligand acndH_2 showed numerous different bridging and chelating capabilities, yielding a new family of 1-D coordination polymers based on {Cu_6Ln_2} repeating units, which have not been previously reported in the literature. Future work includes the synthesis and complete characterization of the remaining members of this {Cu_6Ln_2} family, as well as the employment of other polyaromatic dioximes in 3*d*/4*f*-metal cluster chemistry.

3.4. Final Conclusions

The primary goal of this thesis was the synthesis and characterization of novel polynuclear 3*d*/4*f* heterometallic clusters which would employ Cu^{II} and Ln^{III} metal ions. Indeed, towards that end, the goal has been successfully accomplished. Both families of compounds presented in this thesis ({Cu_4Ln} and {Cu_6Ln_2}$_n$) possess some novelty. In the family of {Cu_4Ln} compounds, while the "propeller"-like topology has been previously reported, these compounds were the first to exhibit interesting magnetic properties, such as SMM behaviour in the Dy^{III} analogue, and the magnetocaloric effect in the Gd^{III} analogue. Furthermore, the project proved the feasibility of using the ligand ndH_2 in 3*d*/4*f* heterometallic cluster chemistry, specifically using Cu^{II} as the 3*d*-metal ion. In the family of {Cu_6Ln_2}$_n$, the synthesized compounds possess a unique 1-D

structure, unique compared to the handful of previously reported 0-D $\{Cu_6Ln_2\}$ clusters in the literature. The members of this family also exhibited interesting magnetic properties. Specifically, the Gd^{III} analogue was found to act as a molecular magnetic refrigerant, while the Tb^{III} analogue exhibited SMM behaviour.

There are some distinct perspectives for future work. None of the compounds presented in this thesis broke any records in the fields of SMMs or molecular magnetic refrigeration. The SMM properties of the $\{Cu_4Dy\}$ and $\{Cu_6Tb_2\}_n$ compounds arise only at very low temperatures. Furthermore, the $-\Delta S_m$ values of the $\{Cu_4Gd\}$ and $\{Cu_6Gd_2\}_n$ complexes did not approach any record values, and were also found to be smaller than their theoretical maximum values (4.8*R* and 8.3*R*, respectively). However, this does not diminish the feasibility of the project. 3*d*/4*f* heterometallic cluster chemistry employing the combination of Cu^{II}/Ln^{III}, in conjunction with the appropriate bridging and chelating ligands, can produce compounds with interesting motifs and magnetic properties such as single-molecule magnetism and molecular magnetic refrigeration. The ligands employed in this thesis (ndH_2 and $acndH_2$) were found to successfully chelate and bridge both 3*d* transition metal ions and 4*f* lanthanide ions, yielding interesting topologies and aesthetically pleasing structures. While the ndH_2 ligand has been explored in homometallic 4*f* cluster chemistry, there is a lack of polynuclear metal complexes in homometallic 3*d* cluster chemistry. This leads to a potential avenue to isolate new compounds that could exhibit interesting physical properties. As well, the only homometallic 3*d* transition metal clusters isolated with the $acndH_2$ ligand were a series of $\{Zn_3\}$ compounds. Consequently, there is great deal of ground that could be covered employing the $acndH_2$ ligand, whether it would be within homometallic 3*d* cluster chemistry using paramagnetic metal ions, or homometallic 4*f* cluster chemistry, as well as new combinations of metals in heterometallic 3*d*/4*f* cluster chemistry.

Ultimately, while the compounds presented in this thesis did not show any approach towards the record holding single-molecule magnets or molecular magnetic refrigerants, the combined use of Cu^{II} and Ln^{III} metal ions is still a viable option for the isolation of these types of compounds. Furthermore, the rich coordination chemistry demonstrated by the ligands employed in this thesis is of great interest for further investigation.

References

[1] Feynman, R. P. *Eng. Sci.* **1960**, *23*, 22.

[2] (*a*) Alexandropoulos, D. I., *PhD Thesis: Single-Molecule Magnets and Multifunctional Molecular Magnetic Materials Based on Polynuclear Metal Complexes*, Brock University: **2015**. (*b*) Athanasopoulou, A. A., *MSc Thesis: Polynuclear Ni(II) Complexes with Schiff Bases as Bridging Ligands: A Molecular Approach to Nanoscience*, Brock University: **2015**.

[3] Christou, G. *Polyhedron* **2005**, *24*, 2065.

[4] Balzani, V.; Credi, A.; Raymo, F. M.; Stoddart, J. F. *Angew Chem. Int. Ed.* **2000**, *39*, 3348.

[5] Papaefstathiou, G. S.; Perlepes, S. P. *Comments on Inorganic Chemistry.* **2002**, *23*, 249.

[6] Papatriantafyllopoulou, C.; Moushi, E. E.; Christou, G.; Tasiopoulos, A. J. *Chem. Soc. Rev.* **2016**, *45*, 1597.

[7] Ishikawa, N.; Sugita, M.; Ishikawa, T.; Koshihara, S.; Kaizu, Y. *J. Am. Chem. Soc.* **2003**, *125*, 8694.

[8] Murugesu, M.; Clérac, R.; Anson, C. E.; Powell, A. K. *Inorg. Chem.* **2004**, *43*, 7269.

[9] Peng, J.-B.; Kong, X.-J.; Zhang, Q.-C.; Orendáč, M.; Prokleška, J.; Ren, Y.-P.; Long, L.-S.; Zheng, Z.; Zheng, L.-S. *J. Am. Chem. Soc.* **2014**, *136*, 17938.

[10] Gu, X.; Xue, D.; *Inorg. Chem.* **2007**, *46*, 3212.

[11] Leng, J.-D.; Liu, J.-L.; Tong, M.-L. *Chem. Commun.* **2012**, *48*, 5286.

[12] Fielden, J.; Cronin, L. *"Coordination Clusters"*, *Encyclopedia of Supramolecular Chemistry*. **2005**, 1.

[13] Olenyuk, B.; Levin, M. D.; Whiteford, J. A.; Shield, J. E.; Stang, P. J. *J. Am. Chem. Soc.* **1999**, *121*, 10434.

[14] Seidel, S. R.; Stang, P. J. *Acc. Chem. Res.* **2002**, *35*, 972.

[15] Fujita, M.; Umemoto, K.; Yoshizawa, M.; Fujita, N.; Kusukawa, T.; Biradha, K. *Chem. Commun.* **2001**, 509.

[16] (*a*) Leininger, S.; Fan, J.; Schmitz, M.; Stang, P. J. *Proc. Natl. Acad. Sci.* **2000**, *97*, 1380. (*b*) Radhakrishnan, U.; Schweiger, M.; Stang, P. J. *Org. Lett*. **2001**, *3*, 3141.

[17] Winpenny, R. E. P. *J. Chem. Soc. Dalton Trans.* **2002**, 1.

[18] Stamatatos, T. C.; Christou, G. *Inorg. Chem.* **2009**, *48*, 3308.

[19] Tasiopoulos, A. J.; Vinslava, A.; Wernsdorfer, W.; Abboud, K. A.; Christou, G. *Angew. Chem. Int. Ed.* **2004**, *116*, 2169.

[20] Baskar, V.; Gopal, K.; Helliwell, M.; Tuna, F.; Wernsdorfer, W.; Winpenny, R. E. P. *Dalton Trans.* **2010**, *39*, 4747.

[21] Aromí, G.; Bell, A. R.; Helliwell, M.; Raftery, J.; Teat, S. J.; Timco, G. A.; Roubeau, O.; Winpenny, R. E. P. *Chem. Eur. J.* **2003**, *9*, 3024.

[22] Liu, K.; Shi, W.; Cheng, P. *Coord. Chem. Rev.* **2015**, *289-290*, 74.

[23] (*a*) Athanasopoulou, A. A.; Pilkington, M.; Raptopoulou, C. P.; Escuer, A.; Stamatatos, T. C. *Chem. Commun.* **2014**, *50*, 14942. (*b*) Kühne, I. A.; Kostakis, G. E.; Anson, C. E.; Powell, A. K. *Chem. Commun.* **2015**, *51*, 2702.

[24] Perlepe, P. S. *MSc Thesis: High-Spin and Emissive Molecular Materials: Synthesis and Characterization of New Polynuclear NiII Complexes from the Use of Aromatic Schiff Bases as Bridging Ligands*, Brock University: **2016**.

[25] Sharples, J. W.; Collison, D. *Coord. Chem. Rev.* **2014**, *260*, 1.

[26] Alexandropoulos, D. I.; Fournet, A.; Cunha-Silva, L.; Mowson, A. M.; Bekiari, V.; Christou, G.; Stamatatos, T. C. *Inorg. Chem.* **2014**, *53*, 5420.

[27] Alexandropoulos, D. I.; Cunha-Silva, L.; Lorusso, G.; Evangelisti, M.; Tang, J.; Stamatatos, T. C. *Chem. Commun.* **2016**, *52*, 1693.

[28] March, J. *Advanced Organic Chemistry*, 4th Ed. Wiley, New York, **1992**. pp. 109, 110, 127, 128, 592, 593, 818, 906, 907, 934, 935, 1198, 1223.

[29] Escuer, A.; Esteban, J.; Roubeau, O. *Inorg. Chem.* **2011**, *50*, 8893.

[30] Stamatatos, T. C.; Escuer, A.; Abboud, K. A.; Raptopoulou, C. P.; Perlepes, S. P.; Christou, G. *Inorg. Chem.* **2008**, *47*, 11825.

[31] Milios, C. J.; Stamatatos, T. C.; Perlepes, S. P. *Polyhedron*, **2006**, *25*, 134.

[32] Papatriantafyllopoulou, C.; Stamatatos, T. C.; Efthymiou, C. G.; Cunha-Silva, L.; Almeida Paz, F. A.; Perlepes, S. P.; Christou, G. *Inorg. Chem.* **2010**, *49*, 9743.

[33] Lampropoulos, C.; Stamatatos, T. C.; Abboud, K. A.; Christou, G. *Inorg. Chem.* **2009**, *48*, 429.

[34] Okazawa, A.; Nogami, T.; Nojiri, H.; Ishida, T. *Chem. Mater.* **2008**, *20*, 3110.

[35] Frost, J. M.; Harriman, K. L. M.; Murugesu, M. *Chem. Sci.* **2016**, *7*, 2470.

[36] Kahn, O. *Molecular Magnetism*, VCH Publishers, New York, **1993**.

[37] Carlin, R. L. *Magnetochemistry*, Springer-Verlag, Berlin, **1986**.

[38] Bain, G. A.; Berry, J. F. *J. Chem. Ed.* **2008**, *85*, 532.

[39] Orchard, A. F. *Magnetochemistry*, Oxford University Press, Oxford, **2003**.

[40] (*a*) Stares, E. *PhD Thesis: Novel Magnetic Materials Based on Macrocyclic Ligands: Towards High Relaxivity Contrast Agents and Mononuclear Single-Molecule Magnets*, Brock University: **2015**. (*b*) Maurer, J. A. *PhD Thesis: I. Structure-Function Analysis of the Mechanosensitive Channel of Large Conductance. II. Design of Novel Magnetic Materials using Crystal Engineering.* California Institute of Technology: **2003**.

[41] (*a*) Getzlaff, M. *Fundamentals of Magnetism*, Springer, Berlin, **2007**. (*b*) Yamauchi, J. *Nitroxides: Applications in Chemistry, Biomedicine, and Materials Science, Chapter 1: Fundamentals of Magnetism*, Wiley-VCH, **2008**.

[42] DeVorkin, D. H. *Henry Norris Russell: Dean of American Astronomers*, Princeton University Press, **2000**.

[43] Reddy, S. L.; Endo, T.; Reddy, G. S. *Electronic (Absorption) Spectra of 3d Transition Metal Complexes*, Intech, **2012**.

[44] https://upload.wikimedia.org/wikipedia/commons/3/30/LS_coupling.svg, Creative Commons License

[45] Liu, J.-L.; Chen, Y.-C.; Guo, F.-S.; Tong, M.-L. *Coord. Chem. Rev.* **2014**, *281*, 26.

[46] Maurice, R.; Verma, P.; Zadrozny, J. M.; Luo, S.; Borycz, J.; Long, J. R.; Truhlar, D. G.; Gagliardi, L. *Inorg. Chem.* **2013**, *52*, 9379.

[47] Drago, R. S. *Physical Methods in Inorganic Chemistry,* Reinhold Publishing Corporation, **1965**.

[48] Goodenough, J. B. *Phys. Rev.* **1968**, *171*, 466.

[49] de Groot, F. *Coord. Chem. Rev.* **2005**, *249*, 31.

[50] Dunn, T. M. *Trans. Faraday Soc.* **1961**, *57*, 1441.

[51] Cole, G. M.; Garrett, B. B. *Inorg. Chem.* **1970**, *9*, 1898.

[52] Stöhr, J.; König, H. *Phys. Rev. Lett.* **1995**, *75*, 3748.

[53] http://www.epr.ethz.ch/education/basic-concepts-of-epr/one-elect--in-the-magn--field/cf-split--so-coupl-.html, ETH Zürich, **2005**.

[54] Zadrozny, J. M.; Liu, J.; Piro, N. A.; Chang, C. J.; Hill, S.; Long, J. R.; *Chem. Commun.* **2012**, *48*, 8317.

[55] Popescu, C. V.; Mock, M. T.; Stoian, S. A.; Dougherty, W. G.; Yap, G. P. A.; Riordan, C. G. *Inorg. Chem.* **2009**, *48*, 8317.

[56] Karunadasa, H. I.; Arquero, K. D.; Berben, L. A.; Long, J. R. *Inorg. Chem.* **2010**, *49*, 4738.

[57] Skomski, R. *Simple models of magnetism.* Oxford University Press, New York, **2008**.

[58] Tang, J.; Zhang, P. *Lanthanide Single Molecule Magnets*, Springer, **2015**.

[59] Jiang, S.-D.; Wang, B.-W.; Gao, S. *Molecular Nanomagnets and Related Phenomena, Chapter 2: Advances in Lanthanide Single-Ion Magnets*, Oxford University Press, **2006**.

[60] Feltham, H. L. C.; Brooker, S. *Coord. Chem. Rev.* **2014**, *276*, 1.

[61] Gatteschi, D.; Sessoli, R.; Villain, J. *Molecular Nanomagnets*, Oxford University Press, **2006**.

[62] Wernsdorfer, W.; Chakov, N. E.; Christou, G. *Phys. Rev. B.* **2004**, *70*, 132413.

[63] Milios, C. J.; Winpenny, R. E. P. *Molecular Nanomagnets and Related Phenomena, Chapter 1: Cluster-Based Single-Molecule Magnets*, *Struct. Bond*, Springer, **2015**.

[64] Bagai, R.; Christou, G. *Chem. Soc. Rev.* **2009**, *38*, 1011.

[65] Morrish, A. H. *The Physical Properties of Magnetism*, Wiley, **1966**.

[66] Woodruff, D. N.; Winpenny, R. E. P.; Layfield, R. A. *Chem. Rev.* **2013**, *113*, 5110.

[67] Moragues-Cánovas, M.; Helliwell, M.; Ricard, L.; Rivière, É.; Wernsdorfer, W.; Brechin, E.; Mallah, T. *Eur. J. Chem. Soc.* **2004**, *11*, 2219.

[68] (*a*) Wernsdorfer, W.; Aliaga-Alcalde, N.; Hendrickson, D. N.; Christou, G. *Nature*, **2002**, *416*, 406. (*b*) Mishra, A.; Wernsdorfer, W.; Abboud, K. A.; Christou, G. *J. Am. Chem. Soc.* **2004**, *126*, 15648. (*c*) del Barco, E.; Kent, A. D.; Hill, S.; North, J. M.; Dalal, N. S.; Rumberger, E. M.; Hendrickson, D. N.; Chakov, N.; Christou, G. *J. Low Temp. Phys.* **2005**, *140*, 119.

[69] (*a*) Xue, S.; Zhao, L.; Guo, Y.-N.; Deng, R.; Guo, Y.; Tang, J. *Dalton Trans.* **2011**, *40*, 8347. (*b)* Palacios, M. A.; Titos-Padilla, S.; Ruiz, J.; Herrera, J. M.; Pope, S. J. A.; Brechin, E. K.; Colacio, E. *Inorg. Chem.* **2014**, *53*, 1465.

[70] (*a*) Sessoli, R.; Gatteschi, D.; Caneschi, A.; Novak, M. A. *Nature*, **1993**, *365*, 141. (*b*) Sessoli, R.; Tsai, H. L.; Schake, A. R.; Wang, S. Y.; Vincent, J. B.; Folting, K.; Gatteschi, D.; Christou, G.; Hendrickson, D. N. *J. Am. Chem. Soc.*, **1993**, *115*, 1804.

[71] Ako, A. M.; Hewitt, I. J.; Mereacre, V.; Clérac, R.; Wernsdorfer, W.; Anson, C. E.; Powell, A. K. *Angew. Chem. Int. Ed.* **2006**, *118*, 5048.

[72] Rinehart, J. D.; Long, J. R. *Chem. Sci.* **2011**, *2*, 2078.

[73] Cotton, S. *Lanthanide and Actinide Chemistry*, Wiley, Hoboken, **2006**.

[74] Habib, F.; Murugesu, M. *Chem. Soc. Rev.* **2013**, *42*, 3278.

[75] Ishida, T.; Watanabe, R.; Fujiwara, K.; Okazawa, A.; Kojima, N.; Tanaka, G.; Yoshii, S.; Nojiri, H. *Dalton Trans.* **2012**, *41*, 13609.

[76] (*a*) Pecharsky, V. K.; Gschneider, Jr., K. A. *J. Magn. Magn. Mater.* **1999**, *200*, 44. (*b*) Gschneider, Jr., K. A.; Pecharsky, V. K. *J. Appl. Phys.* **1999**, *85*, 5365.

[77] (*a*) Kinney, W. I.; Wolf, W. P. *J. Appl. Phys*. **1979**, *50*, 2115. (*b*) McMichael, R. D.; Ritter, J. J.; Shull, R. D. *J. Appl. Phys.* **1993**, *73*, 6946.

[78] Luis, F.; Evangelisti, M. *Molecular Nanomagnets and Related Phenomena, Chapter 9: Magnetic Refrigeration and Spin-Lattice Relaxation in Gadolinium-Based Molecular Nanomagnets*, *Struct. Bond*, Springer, **2015**.

[79] Liu, J.-L.; Chen, Y.-C.; Guo, F.-S.; Tong, M.-L. *Coord. Chem. Rev.* **2014**, *281*, 26.

[80] Garlatti, E.; Carretta, S.; Schnack, J.; Amoretti, G.; Santini, P. *Appl. Phys. Lett.* **2013**, *103*, 202410.

[81] (*a*) Evangelisti, M.; Brechin, E. K. *Dalton Trans.* **2010**, *39*, 4672. (*b*) Zheng, Y.-Z.; Zhou, G.-J.; Zheng, Z.; Winpenny, R. E. P. *Chem. Soc. Rev.* **2014**, *43*, 1462.

[82] (*a*) Liddle, S. T.; von Slageren, J. *Chem. Soc. Rev.* **2015**, *44*, 6655. (*b*) Piquer, L. R.; Sañudo, E. C. *Dalton Trans.* **2015**, *44*, 8771.

[83] Housecroft, C. E.; Sharpe, A. G. *Inorganic Chemistry, Fourth Edition*, Pearson, **2012**.

[84] (*a*) Andruh, M.; Ramade, I.; Codjovi, E.; Guillou, O.; Kahn, O.; Trombe, J.-C. *J. Am. Chem. Soc.* **1993**, *115*, 1822. (*b*) Paulovič, J.; Cimpoesu, F.; Ferbinteanu, M.; Hirao, K. *J. Am. Chem. Soc.* **2004**, *126*, 3321. (*c*) Shimada, T.; Okazawa, A.; Kojima, N.; Yoshii, S.; Nojiri, H.; Ishida, T. *Inorg. Chem.* **2011**, *50*, 10555.

[85] Rajeshkumar, T.; Annadata, H. V.; Evangelisti, M.; Langley, S. K.; Chilton, N. F.; Murray, K. S.; Rajaraman, G. *Inorg. Chem.* **2015**, *54*, 1661.

[86] Chen, Y.-C.; Guo, F.-S.; Liu, J.-L.; Leng, J.-D.; Vrábel, P.; Orendáč, M.; Prokleška, J.; Sechovský, V.; Tong, M.-L. *Chem. Eur. J.* **2014**, *20*, 3029.

[87] Langley, S. K.; Chilton, N. F.; Moubaraki, B.; Hooper, T.; Brechin, E. K.; Evangelisti, M.; Murray, K. S. *Chem. Sci.* **2011**, *2*, 1166.

[88] Liu, J.-L.; Lin, W.-Q.; Chen, Y.-C.; Gómez-Coca, S.; Aravena, D.; Ruiz, E.; Leng, J.-D.; Tong, M.-L. *Chem. Eur. J.* **2013**, *19*, 17567.

[89] Kottke, T.; Stalke, D. *J. App. Cryst.* **1993**, *26*, 615.

[90] APEX2, *Data Collection Software Version 2012.4*, Bruker AXS, Delft, The Netherlands, **2012**.

[91] Cryopad, *Remote monitoring and control, Version 1.451*, Oxford Cryosystems, Oxford, United Kingdom, **2006**.

[92] SAINT+, *Data Integration Engine v. 8.27b*©, **1997 – 2012**, Bruker AXS, Madison, Wisconsin, USA.

[93] Sheldrick, G. M. *SADABS 2012/1, Bruker AXS Area Detector Scaling and Absorption Correction Program*, **2012**, Bruker AXS, Madison, Wisconsin, USA.

[94] Sheldrick, G. M. *Acta. Cryst. A*, **2008**, *64*, 112.

[95] Sheldrick, G. M. *SHELXT v. 2014/3, Program for Crystal Structure Solution*, University of Göttingen, **2014**.

[96] Sheldrick, G. M. *SHELXL v. 2014, Program for Crystal Structure Refinement*, University of Göttingen, **2014**.

[97] Koumousi, E. S.; Zampakou, M.; Raptopoulou, C. P.; Psycharis, V. P.; Beavers, C. M.; Teat, S. J.; Psomas, G.; Stamatatos, T. C. *Inorg. Chem.* **2012**, *51*, 7699.

[98] (*a*) Alvarez, S.; Alemany, P.; Casanova, D.; Cirera, J.; Llunell, M.; Avnir, D. *Coord. Chem. Rev.* **2005**, *249*, 1693.

[99] (*a*) Sun, Y.-Q.; Liang, M.; Dong, W.; Yang, G.-M.; Liao, D.-Z.; Jiang, Z.-H.; Yan, S.-P.; Cheng, P. *Eur. J. Inorg. Chem.* **2004**, 1514. (*b*) Zhang, L.; Wang, S.-B.; Yang, G.-M.; Tang, J.; Liao, D.-Z.; Jiang, Z.-H.; Yan, S.-P.; Cheng, P. *Inorg. Chem.* **2003**, *42*, 1462. (*c*) Sanz, J. L.; Ruiz, R.; Gleizes, A.; Lloret, F.; Faus, J.; Julve, M.; Borras-Almenar, J. J.; Journaux, Y. *Inorg. Chem.* **1996**, *35*, 7384. (*d*) Zhu, Q.; Xiang, S.; Sheng, T.; Yuan, D.; Shen, C.; Tan, C.; Hu, S.; Wu, X. *Chem. Commun.* **2012**, *48*, 10736.

[100] Chilton, N. F.; Anderson, R. P.; Turner, L. D.; Soncini, A.; Murray, K. S. *J. Comput. Chem.* **2013**, *34*, 1164.

[101] Blagg, R. J.; Ungur, L.; Tuna, F.; Speak, J.; Comar, P.; Collison, D. N.; Wernsdorfer, W.; McInnes, E. J. L.; Chibotaru, L.; Winpenny, R. E. P. *Nat. Chem.* **2013**, *5*, 673.

[102] Hooper, T. N.; Schnack, J.; Piligkos, S.; Evangelisti, M.; Brechin, E. K. *Angew. Chem. Int. Ed.* **2012**, *51*, 4633.

[103] (*a*) Wu, S.; Cheng, H.; Chen, Z.; Zhang, Z.; Liang, F. Z. *Z. Anorg. Allg. Chem.* **2014**, *640*, 1000. (*b*) Williams, O. M.; Cowley, A. H.; Rose, M. J. *Dalton Trans.* **2015**, *44*, 13017.

[104] Rai, H. C.; Rai, B. K. *Asian J. Chem.* **2001**, *13*, 264.

[105] (*a*) Alexandropoulos, D. I.; Papatriantafyllopoulou, C.; Li, C.; Cunha-Silva, L.; Manos, M. J.; Tasiopoulos, A. J.; Wernsdorfer, W.; Christou, G.; Stamatatos, T. C. *Eur. J. Inorg. Chem.* **2013**, 2286. (*b*) Stamatatos, T. C.; Luisi, B. S.; Moulton, B.; Christou, G. *Inorg. Chem.* **2008**, *47*, 1134.

[106] (*a*) Koumousi, E. S.; Raptopoulou, C. P.; Perlepes, S. P.; Escuer, A.; Stamatatos, T. C. *Polyhedron* **2010**, *29*, 204. (*b*) Okawa, H.; Koikawa, M.; Kida, S.; Luneau, D.; Oshio, H. *J. Chem. Soc., Dalton Trans.* **1990**, 469. (*c*) Luneau, D.; Oshio, H.; Okawa, H.; Kida, S. *J. Chem.*

Soc., Dalton Trans. **1990**, 2283. (*d*) Chaudhuri, P.; Winter, M.; Della Vedova, B. P. C.; Bill, E.; Trautwein, A.; Gehring, S.; Fleischauer, P.; Nuber, B.; Weiss, J. *Inorg. Chem.* **1991**, *30*, 2148. (*e*) Ruiz, R.; Sanz, J.; Cervera, B.; Lloret, F.; Julve, M.; Bois, C.; Faus, J.; Muñoz, M. C. *J. Chem. Soc., Dalton Trans.* **1993**, 1623. (*f*) Ruiz, R.; Sanz, J.; Lloret, F.; Julve, M.; Faus, J.; Bois, C.; Muñoz, M. C. *J. Chem. Soc., Dalton Trans.* **1993**, 3035. (*g*) Ruiz, R.; Lloret, F.; Julve, M.; Muñoz, M. C.; Bois, C. *Inorg. Chim. Acta* **1994**, 179. (*h*) Colacio, E.; Dominguez-Vera, J. M.; Escuer, A.; Klinga, M.; Kivekäs, R.; Romerosa, A. *J. Chem. Soc., Dalton Trans.* **1995**, 343. (*i*) Dominguez-Vera, J. M.; Colacio, E.; Escuer, A.; Klinga, M.; Kivekäs, R.; Romerosa, A. *Polyhedron* **1997**, *16*, 281. (*j*) Chaudhuri, P.; Winter, M.; Flörke, U.; Haupt, H.-J. *Inorg. Chim. Acta* **1995**, *232*, 125.

[107] Llunell, M.; Casanova, D.; Girera, J.; Alemany, P.; Alvarez, S. *SHAPE Version 2.0*, Barcelona, Spain, **2010**.

[108] Zabrodsky, H.; Peleg, S.; Avnir, D. *J. Am. Chem. Soc.* **1992**, *114*, 7843.

[109] Ruiz-Martinez, A.; Casanova, D.; Alvarez, S. *Chem. Eur. J.* **2008**, *14*, 1291.

[110] Zabrodsky, H.; Peleg, S.; Avnir, D. *J. Am. Chem. Soc.* **1993**, *115*, 8278.

[111] (*a*) Xue, S.; Guo, Y.-N.; Zhao, L.; Zhang, H.; Tang, J. *Inorg. Chem.* **2014**, *53*, 8165. (*b*) Sheng, E.; Yu, W.; Li, X. *Inorg. Chem. Commun.* **2008**, *11*, 418.

[112] (*a*) Zhang, P.; Zhang, L.; Tang, J. *Dalton Trans*. **2015**, *44*, 3923. (*b*) Zhang, P.; Zhang, L.; Wang, C.; Xue, S.; Lin, S.- Y.; Tang, J. *J. Am. Chem. Soc*. **2014**, *136*, 4484. (*c*) Ungur, L.; Lin, S.- Y.; Tang, J.; Chibotaru, L. F. *Chem. Soc. Rev*. **2014**, *43*, 6894. (*d*) Aronica, C.; Pilet, G.; Chastanet, G.; Wernsdorfer, W.; Jacquot, J.- F.; Luneau, D. *Angew. Chem. Int. Ed*. **2006**, *45*, 4659. (*e*) Langley, S. K.; Ungur, L.; Chilton, N. F.; Moubaraki, B.; Chibotaru, L. F.; Murray, K. S. *Chem. Eur. J*. **2011**, *17*, 9209.

[113] (*a*) Aronica, C.; Chastanet, G.; Pilet, G.; Le Guennic, B.; Robert, V.; Wernsdorfer, W.; Luneau, D. *Inorg. Chem.* **2007**, *46*, 6108. (*b*) Iasco, O.; Novitchi, G.; Jeanneau, E.; Luneau, D. *Inorg. Chem.* **2013**, *52*, 8723. (*c*) Akine, S.; Matsumoto, T.; Taniguchi, T.; Nabeshima, T. *Inorg. Chem.* **2005**, *44*, 3270. (*d*) Dinca, A. S.; Ghirri, A.; Madalan, A. M.; Affronte, M.; Andruh, M. *Inorg. Chem.* **2012**, *51*, 3935. (*e*) Pavlishchuk, A. V.; Kolotilov, S. V.; Zeller, M.; Thompson, L. K.; Addison, A. W. *Inorg. Chem.* **2014**, *53*, 1320.

[114] (*a*) Ramade, I.; Kahn, O.; Jeannin, Y.; Robert, F. *Inorg. Chem.* **1997**, *36*, 930. (*b*) Koner, R.; Lin, H.-H.; Wei, H.-H.; Mohanta, S. *Inorg. Chem.* **2005**, *44*, 3524.

[115] (*a*) Costes, J.-P.; Duhayon, C.; Mallet-Ladeira, S.; Vendier, L.; Garcia-Tojal, J.; Lopez Banet, L. *Dalton Trans.* **2014**, *43*, 11388. (*b*) Costes, J.-P.; Dahan, F.; Dupuis, A. *Inorg. Chem.* **2000**, *39*, 165. (*c*) Colacio, E.; Ruiz, J.; Mota, A. J.; Palacios, M. A.; Cremades, E.; Ruiz, E.; White, F. J.; Brechin, E. K. *Inorg. Chem.* **2012**, *51*, 5857. (*d*) Cremades, E.; Gómez-Coca, S.; Aravena, D.; Alvarez, S.; Ruiz, E. *J. Am. Chem. Soc.* **2012**, *134*, 10532.

[116] (*a*) Feltham, H. L. C.; Clérac, R.; Ungur, L.; Vieru, V.; Chibotaru, L. F.; Powell, A. K.; Brooker, S. *Inorg. Chem.* **2012**, *51*, 10603. (*b*) Feltham, H. L. C.; Clérac, R.; Ungur, L.; Chibotaru, L. F.; Powell, A. K.; Brooker, S. *Inorg. Chem.* **2013**, *52*, 3236. (*c*) Feltham, H. L. C.; Clérac, R.; Powell, A. K.; Brooker, S. *Inorg. Chem.* **2011**, *50*, 4232. (*d*) Hamamatsu, T.; Matsumoto, N.; Re, N.; Mrozinski, J. *Chem. Lett.* **2009**, *38*, 762. (*e*) Ida, Y.; Ghosh, S.; Ghosh, A.; Nojiri, H.; Ishida, T. *Inorg. Chem.* **2015**, *54*, 9543. (*f*) Winpenny, R. E. P. *Molecular Cluster Magnets*; World Scientific Publishing Co., **2012**. (*g*) Layfield, R. A.; Murugesu, M. *Lanthanides and Actinides in Molecular Magnetism*; Wiley-VCH, **2015**.

[117] Bartolomé, J.; Filoti, G.; Kuncser, V.; Schinteie, G.; Mereacre, V.; Anson, C. E.; Powell, A. K.; Prodius, D.; Turta, C. *Phys. Rev. B.* **2009**, *80*, 14430.

[118] (*a*) Dermitzaki, D.; Lorusso, G.; Raptopoulou, C. P.; Psycharis, V.; Escuer, A.; Evangelisti, M.; Perlepes, S. P.; Stamatatos, Th. C. *Inorg. Chem.* **2013**, *52*, 10235. (*b*) Hooper, T. N.; Inglis, R.; Palacios, M. A.; Nichol, G. S.; Pitak, M. B.; Coles S. J.; Lorusso, G.; Evangelisti, M.; Brechin, E. K., *Chem. Commun*., **2014**, 50, 3498.

[119] Evangelisti, M.; Roubeau, O.; Palacios, E.; Camón, A.; Hooper, T. N.; Brechin, E. K.; Alonso, J. J. *Angew. Chem. Int. Ed*. **2011**, *50*, 6606.

4. Appendix

4.1. IR Spectra of All Synthesized Metal Clusters and Ligands

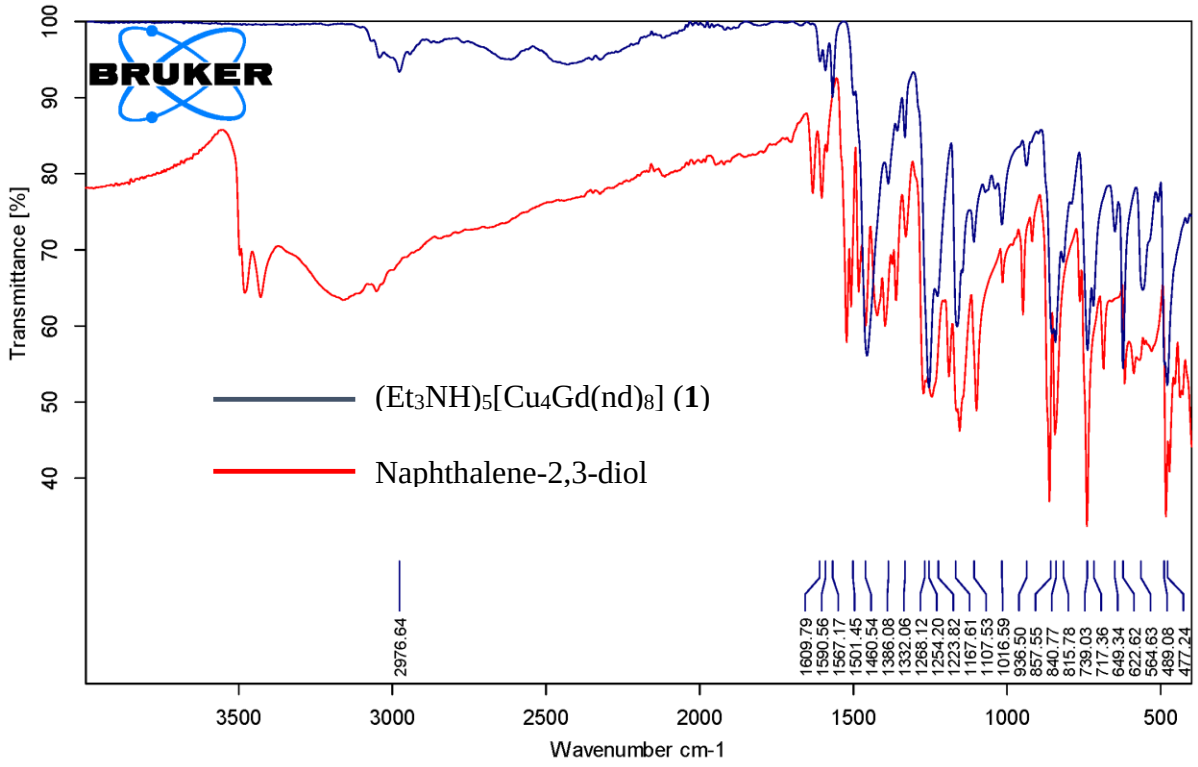

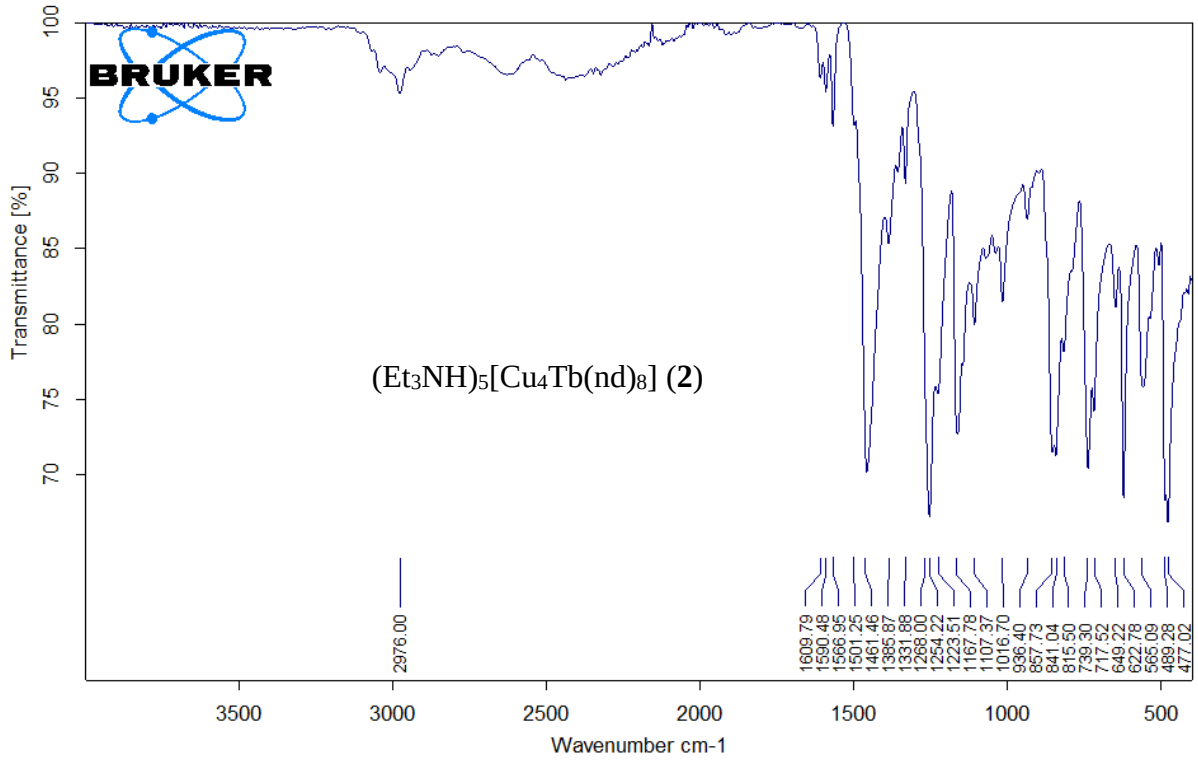
BRUKER
Transmittance [%]
100
95
90
85
80
75
70
(Et3NH)5[Cu4Tb(nd)8] (2)
2976.00
1609.79
1590.48
1566.95
1501.25
1461.46
1385.87
1331.88
1268.00
1254.22
1223.51
1167.78
1107.37
1016.70
936.40
857.73
841.04
815.50
739.30
717.52
649.22
622.78
565.09
489.28
477.02
3500
3000
2500
2000
1500
1000
500
Wavenumber cm-1

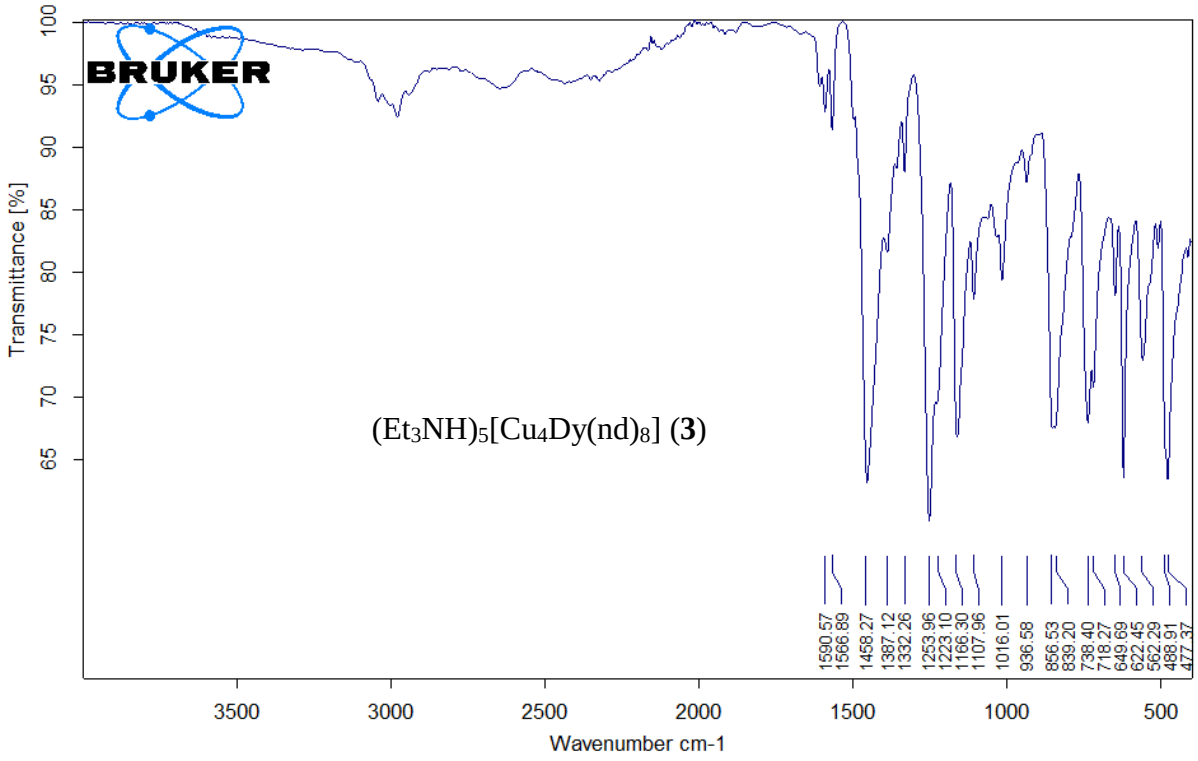
BRUKER
Transmittance [%]
100
95
90
85
80
75
70
65
(Et3NH)5[Cu4Dy(nd)8] (3)
1590.57
1566.89
1458.27
1387.12
1332.26
1253.96
1223.10
1166.30
1107.96
1016.01
936.58
856.53
839.20
738.40
718.27
649.69
622.45
562.29
488.91
477.37
3500
3000
2500
2000
1500
1000
500
Wavenumber cm-1

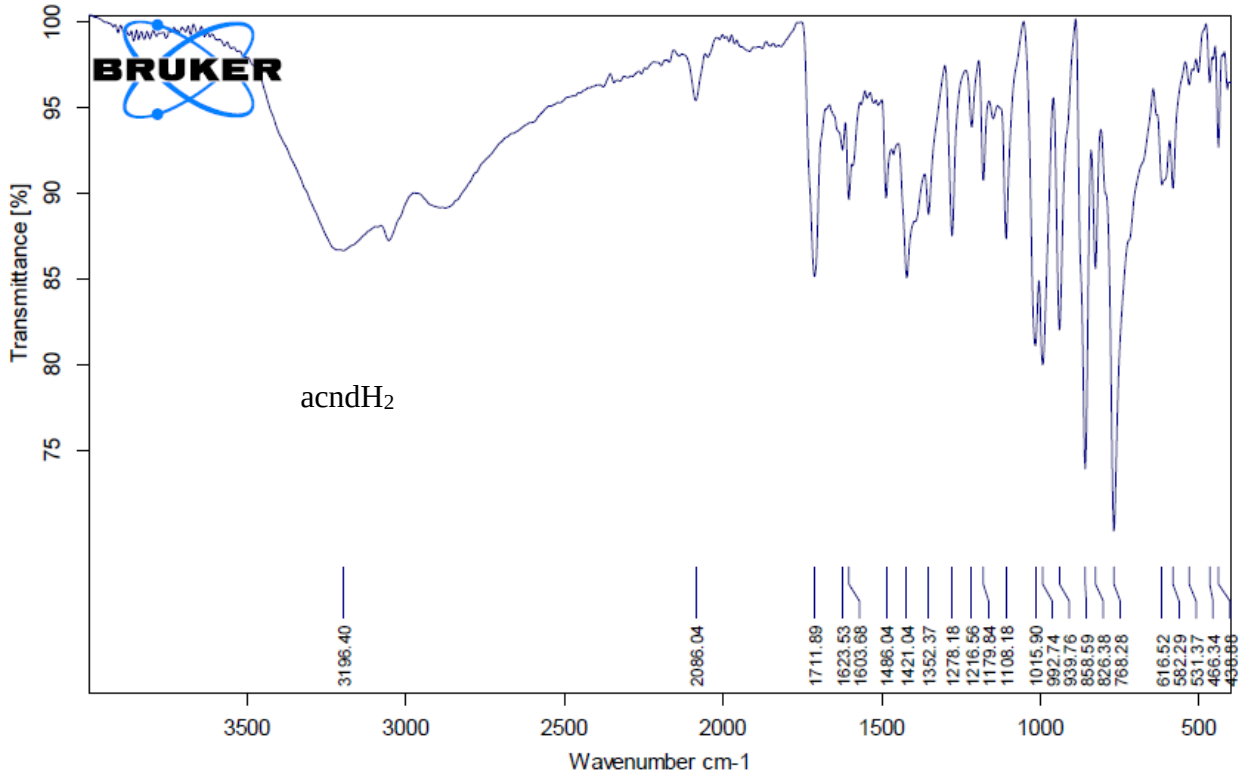
BRUKER
Transmittance [%]
100
95
90
85
80
75
acndH2
3196.40
2086.04
1711.89
1623.53
1603.68
1486.04
1421.04
1352.37
1278.18
1216.56
1179.84
1108.18
1015.90
992.74
939.76
858.59
826.38
768.28
616.52
582.29
531.37
466.34
438.88
3500
3000
2500
2000
1500
1000
500
Wavenumber cm-1

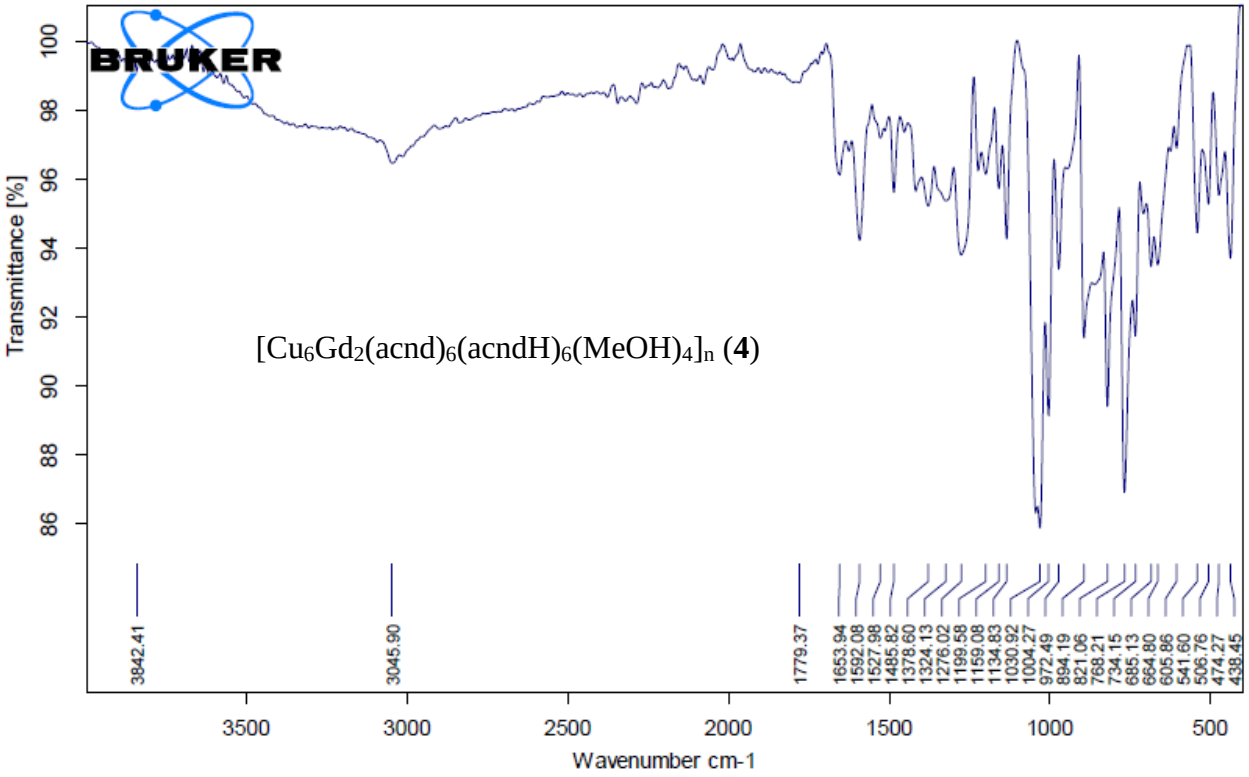
BRUKER
Transmittance [%]
100
98
96
94
92
90
88
86
[Cu6Gd2(acnd)6(acndH)6(MeOH)4]n (4)
3842.41
3045.90
1779.37
1653.94
1592.08
1527.98
1485.82
1378.60
1324.13
1276.02
1199.58
1159.08
1134.83
1030.92
1004.27
972.49
894.19
821.06
768.21
734.15
685.13
664.80
605.86
541.60
506.76
474.27
438.45
3500
3000
2500
2000
1500
1000
500
Wavenumber cm-1

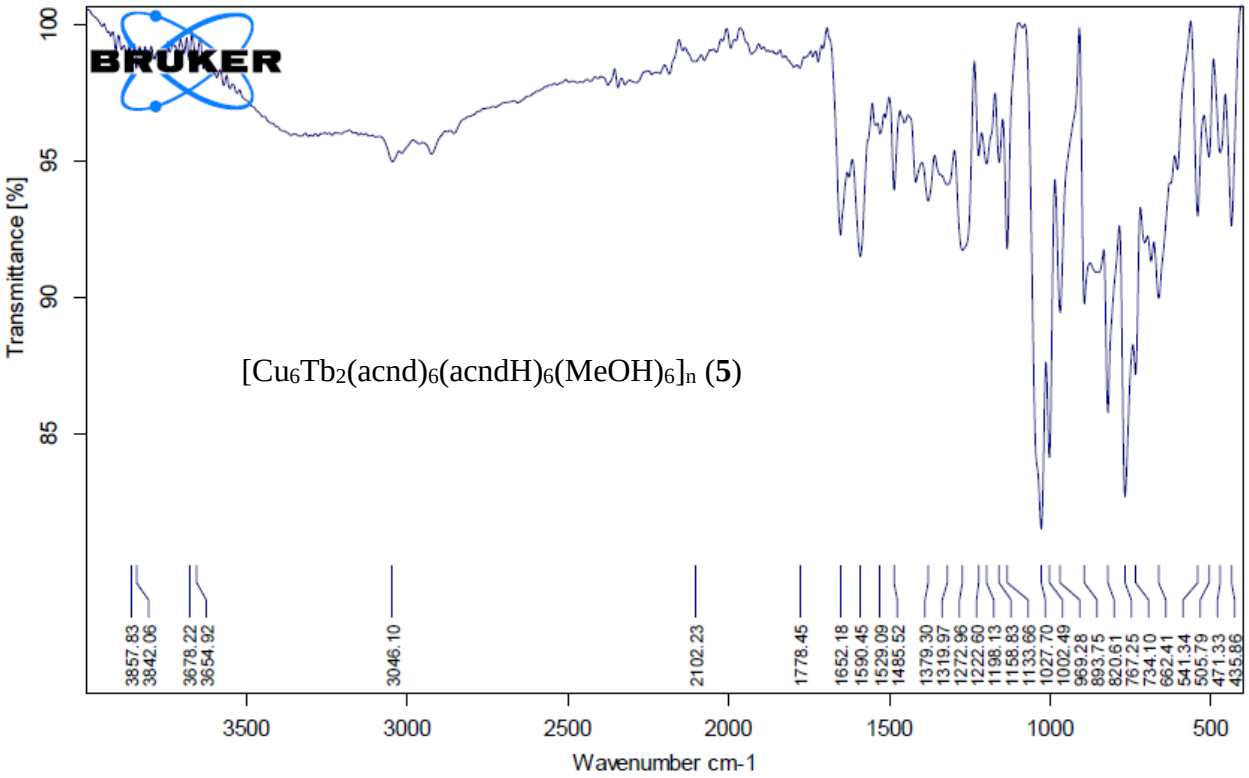
BRUKER
Transmittance [%]
100
95
90
85
[Cu6Tb2(acnd)6(acndH)6(MeOH)6]n (5)
3857.83
3842.06
3678.22
3654.92
3046.10
2102.23
1778.45
1652.18
1590.45
1529.09
1485.52
1379.30
1319.97
1272.96
1222.60
1198.13
1158.83
1133.66
1027.70
1002.49
969.28
893.75
820.61
767.25
734.10
662.41
541.34
505.79
471.33
435.86
3500
3000
2500
2000
1500
1000
500
Wavenumber cm-1

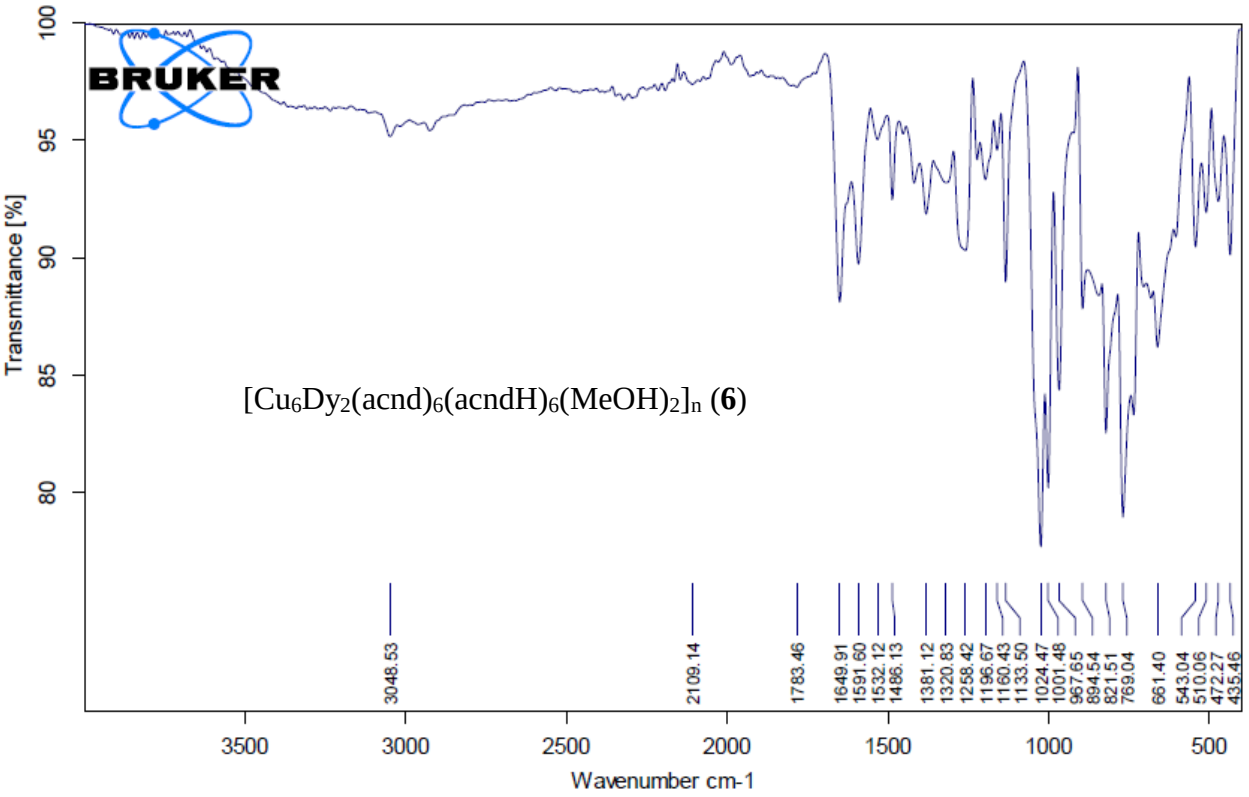
BRUKER
Transmittance [%]
100
95
90
85
80
[Cu6Dy2(acnd)6(acndH)6(MeOH)2]n (6)
3048.53
2109.14
1783.46
1649.91
1591.60
1532.12
1486.13
1381.12
1320.83
1258.42
1196.67
1160.43
1133.50
1024.47
1001.48
967.65
894.54
821.51
769.04
661.40
543.04
510.06
472.27
435.46
3500
3000
2500
2000
1500
1000
500
Wavenumber cm-1

4.2. Tables of Bond Distances and Bond Angles

Table 4.1. Selected interatomic distances (Å), bond angles (°), and torsion angles (°) for complex **1**.

Intermetallic Distances (Å)			
Gd1···Cu1	3.311	Cu1···Cu2	4.759
Gd1···Cu2	3.332	Cu2···Cu4	4.908
Gd1···Cu3	3.333	Cu4···Cu3	4.573
Gd1···Cu4	3.352	Cu3···Cu1	4.688
Bond Distances (Å)			
Gd1—O3	2.359 (5)	Cu4—O12	1.886 (7)
Gd1—O9	2.368 (5)	Cu4—O9	1.910 (6)
Gd1—O15	2.397 (6)	Cu4—O10	1.923 (6)
Gd1—O7	2.395 (5)	Cu4—O11	1.932 (5)
Gd1—O11	2.407 (5)	Cu3—O16	1.888 (7)
Gd1—O5	2.441 (5)	Cu3—O14	1.916 (6)
Gd1—O1	2.466 (5)	Cu3—O13	1.929 (5)
Gd1—O13	2.492 (5)	Cu3—O15	1.945 (5)
Cu2—O6	1.874 (5)	Cu1—O2	1.927 (6)
Cu2—O8	1.919 (5)	Cu1—O1	1.921 (5)
Cu2—O7	1.930 (5)	Cu1—O3	1.926 (6)
Cu2—O5	1.925 (5)	Cu1—O4	1.948 (6)
Bond Angles (°)			
Cu1—O1—Gd1	97.2 (2)	Cu3—O13—Gd1	97.1 (2)

Cu1—O3—Gd1	100.7 (2)	Cu3—O15—Gd1	99.8 (2)
Cu2—O7—Gd1	100.2 (2)	Cu4—O9—Gd1	102.7 (2)
Cu2—O5—Gd1	98.8 (2)	Cu4—O11—Gd1	100.6 (2)

Torsion Angles (º)			
Cu1—O1—Gd1—O3	13.34	Cu2—O5—Gd1—O7	7.90
Cu3—O13—Gd1—O15	11.08	Cu4—O9—Gd1—O11	2.10

Table 4.2. Selected interatomic distances (Å) and bond angles (º) for complex **2**.

Intermetallic Distances (Å)			
Tb1···Cu1	3.321	Cu1···Cu3	4.816
Tb1···Cu2	3.321	Cu3···Cu2	4.583
Tb1···Cu3	3.335	Cu2···Cu4	4.690
Tb1···Cu4	3.300	Cu4···Cu1	4.757

Bond Distances (Å)			
Tb1—O13	2.346 (7)	Cu2—O8	1.878 (9)
Tb1—O9	2.364 (7)	Cu2—O7	1.899 (9)
Tb1—O5	2.369 (8)	Cu2—O6	1.906 (8)
Tb1—O1	2.387 (8)	Cu2—O5	1.940 (8)
Tb1—O10	2.402 (7)	Cu3—O11	1.882 (9)
Tb1—O2	2.425 (8)	Cu3—O9	1.906 (8)
Tb1—O14	2.444 (7)	Cu3—O10	1.931 (8)
Tb1—O6	2.461 (8)	Cu3—O12	1.932 (9)

Cu1—O3	1.874 (8)	Cu4—O15	1.922 (9)
Cu1—O4	1.907 (8)	Cu4—O14	1.924 (8)
Cu1—O1	1.924 (8)	Cu4—O16	1.925 (9)
Cu1—O2	1.925 (8)	Cu4—O13	1.936 (9)
Bond Angles (º)			
Cu1—O1—Tb1	100.2 (3)	Cu3—O9—Tb1	102.2 (3)
Cu1—O2—Tb1	98.9 (3)	Cu3—O10—Tb1	100.1 (3)
Cu2—O5—Tb1	100.4 (3)	Cu4—O13—Tb1	100.4 (3)
Cu2—O6—Tb1	98.2 (3)	Cu4—O14—Tb1	97.4 (3)

Table 4.3. Selected interatomic distances (Å), bond angles (º), and torsion angles (º) for complex **4**.

Intermetallic Distances (Å)			
Gd1···Cu1	3.545	Cu1···Cu2	5.317
Gd1···Cu2	3.539	Cu2···Cu3	5.556
Gd1···Cu3	3.582	Cu3···Cu1	5.452
Bond Distances (Å)			
Gd1—O1	2.446 (4)	Cu1—N2	1.982 (5)
Gd1—O3	2.432 (4)	Cu1—N4	1.950 (5)
Gd1—O5	2.427 (4)	Cu2—O5	1.942 (4)
Gd1—O7	2.415 (4)	Cu2—O7	1.944 (4)
Gd1—O9	2.426 (4)	Cu2—N6	1.979 (5)
Gd1—O11	2.438 (4)	Cu2—N8	1.961 (5)

Gd1—O13	2.480 (4)	Cu3—O9	1.925 (4)
Gd1—O14	2.513 (4)	Cu3—O11	1.954 (4)
Gd1—O15	2.466 (4)	Cu3—N10	1.977 (6)
Cu1—O1	1.932 (4)	Cu3—N12	1.954 (5)
Cu1—O3	1.953 (4)		
Bond Angles (º)			
Cu1—O1—Gd1	107.55 (16)	Cu2—O7—Gd1	108.06 (17)
Cu1—O3—Gd1	107.38 (16)	Cu3—O9—Gd1	110.27 (17)
Cu2—O5—Gd1	107.69 (17)	Cu3—O11—Gd1	108.80 (16)
Torsion Angles (º)			
Gd1—O3—N3—Cu2	1.87	Cu2—O6—N6—Cu2′	94.13
Cu1—O2—N2—Cu1′	83.33		

Table 4.4. Selected interatomic distances (Å), bond angles (º), and torsion angles (º) for complex **6**.

Intermetallic Distances (Å)			
Dy1···Cu1	3.391	Cu1···Cu2	5.251
Dy1···Cu2	3.405	Cu2···Cu3	5.348
Dy1···Cu3	3.407	Cu3···Cu1	5.294
Bond Distances (Å)			
Dy1—O1	2.283 (3)	Cu1—N2	1.956 (4)
Dy1—O3	2.354 (3)	Cu2—O5	1.929 (3)
Dy1—O5	2.296 (3)	Cu2—N8	1.940 (4)

Dy1—O7	2.342 (3)	Cu2—O7	1.951 (3)
Dy1—O9	2.296 (3)	Cu2—N6	1.964 (4)
Dy1—O11	2.343 (3)	N12—Cu3	1.946 (4)
Dy1—O13	2.308 (4)	O11—Cu3	1.944 (3)
Cu1—O1	1.942 (3)	Cu3—O9	1.931 (3)
Cu1—O3	1.943 (3)	Cu3—N10	1.960 (4)
Cu1—N4	1.943 (4)		

Bond Angles (º)

Cu1—O1—Dy1	106.46 (15)	Cu2—O7—Dy1	104.59 (14)
Cu1—O3—Dy1	103.80 (13)	Cu3—O9—Dy1	107.10 (14)
Cu2—O5—Dy1	107.04 (15)	Cu3—O11—Dy1	104.90 (14)

Torsion Angles (º)

Dy1—O3—N3—Cu2	4.89	Cu3—O10—N10—Cu3′	84.78
Cu1—O2—N2—Cu1′	80.51		